Dipl.-Ing. Gernot J. Kraberger, BSc

Development of a full matrix ab-initio scheme for materials with strong spin-orbit coupling and Coulomb interactions

Application to selected iridates and osmates

DOCTORAL THESIS

For obtaining the academic degree of
Doktor der technischen Wissenschaften

Doctoral Program in Engineering Sciences
Doctoral School Physics

Graz University of Technology

Supervisor:
Ass. Prof. Dipl.-Ing. Dr. Markus Aichhorn

Institute of Theoretical and Computational Physics

Graz, February 2018

AFFIDAVIT

I declare that I have authored this thesis independently, that I have not used other than the declared sources/resources, and that I have explicitly indicated all material which has been quoted either literally or by content from the sources used. The text document uploaded to TUGRAZonline is identical to the present doctoral thesis.

Date

Signature

Abstract

The recent research interest in systems containing heavy atoms with open d-shells calls for a set of tools that can accurately calculate their electronic structure in the presence of both strong correlations and spin-orbit coupling (SOC). As the physical properties of these materials are determined by the interplay of these ingredients, both have to be included simultaneously in the theoretical description. For treating the electron-electron interaction based on first principles, the density functional theory plus dynamical mean-field theory (DFT+DMFT) is a well-established, highly successful method. In this thesis, the non-trivial inclusion of SOC into that framework is tackled and a strategy to circumvent the obstacles one faces is developed.

The SOC gives rise to a significant complex-valued orbital hybridization, which in turn leads to complex matrix-valued local Green's functions that have to be handled in the DMFT. As a consequence, the Quantum Monte Carlo (QMC) impurity solver needs to be adapted. But even then, usually a pronounced fermionic sign problem is present in these calculations. We investigate how this problem can be avoided, or at least minimized. In order to tame the noise that is inevitably present in any QMC run, a fit of the self-energy at high Matsubara frequencies has to be performed. The required adaptations to the fit procedure for the treatment of the complex-valued case are explained.

After a successful DMFT calculation using state-of-the-art QMC solvers, the real-frequency behavior of the system can be determined from the imaginary-time results in order to allow a better physical interpretation. This analytic continuation of the data can be carried out by different methods, most of which cannot handle the matrix-valued case correctly. We present a variant of the popular Maximum Entropy method for analytic continuation, which extracts matrix-valued spectral functions while preserving the physical properties of positive definiteness and Hermiticity.

Our scheme for DFT+DMFT calculations is then applied to a heterostructure of $SrTiO_3$ and $SrIrO_3$, for which we also show a newly developed approach for reducing the number of orbital degrees of freedom. We calculate the correlated properties of the compound and compare with experiment. Finally, the double perovskite Sr_2MgOsO_6 is studied, where we can confirm the Mott insulating state found in experiment and previous studies. For that material, we also benchmark the influence of different possible approximations to the full theory.

Kurzfassung

Das gegenwärtig rege Forschungsinteresse an Systemen, die schwere Atome mit offenen d-Schalen enthalten, erfordert Methoden, die es erlauben, deren elektronische Struktur in Gegenwart sowohl starker Korrelationen als auch der Spin-Bahn-Kopplung akkurat zu berechnen. Da die physikalischen Eigenschaften dieser Materialien durch das Zusammenspiel dieser beiden Zutaten bestimmt werden, müssen beide gleichzeitig in die theoretische Beschreibung einbezogen werden. Ein etabliertes, sehr erfolgreiches Verfahren zur *ab initio* Behandlung der Elektron-Elektron-Wechselwirkung ist die Kombination der Dichtefunktionaltheorie mit der dynamischen Molekularfeldtheorie (DFT+DMFT). Die vorliegende Arbeit beschäftigt sich damit, die Spin-Bahn-Kopplung in dieses Schema zu integrieren, sowie die auftretenden Schwierigkeiten zu lösen.

Die Spin-Bahn-Kopplung führt zu einer beträchtlichen komplexwertigen Orbitalhybridisierung, die wiederum zu komplexen matrixwertigen lokalen Green'schen Funktionen führt, welche in der DMFT zu behandeln sind. Daher sind Adaptierungen am Quanten-Monte-Carlo (QMC) Störstellenlöser nötig, aber selbst dann kommt es bei diesen Berechnungen meist zu einem ausgeprägten fermionischen Vorzeichenproblem. Wir untersuchen, wie dieses vermieden oder zumindest minimiert werden kann. Um dem Rauschen, das in jedem QMC-Lauf unvermeidlich ist, entgegen zu wirken, muss ein Fit der Selbstenergie bei hohen Matsubara-Frequenzen durchgeführt werden. Die nötigen Anpassungen dieser Fitprozedur für den komplexwertigen Fall werden erläutert.

Um das Ergebnis einer erfolgreichen DMFT-Rechnung mit aktuellen QMC-Algorithmen besser physikalisch interpretieren zu können, kann man die Eigenschaften des Systems als Funktion reeller Frequenzen aus der Lösung in imaginärer Zeit ermitteln. Diese analytische Fortsetzung der Daten kann mittels verschiedener Methoden durchgeführt werden, von denen die meisten den matrixwertigen Fall nicht korrekt behandeln. Wir präsentieren eine Variante der oft verwendeten Maximum-Entropie-Methode zur analytischen Fortsetzung, die matrixwertige Spektralfunktionen liefert und dabei die physikalischen Eigenschaften der Positiv-Definitheit und Hermitizität bewahrt.

Unsere Technik für DFT+DMFT-Rechnungen wird dann auf eine Heterostruktur von $SrTiO_3$ und $SrIrO_3$ angewandt, für die wir auch einen neuentwickelten Ansatz zur Reduktion der Anzahl der Orbitalfreiheitsgrade vorstellen. Wir berechnen die korrelierten Eigenschaften der Heterostruktur und vergleichen sie mit Experimenten. Schlussendlich wird der Doppelperowskit Sr_2MgOsO_6 untersucht, dessen Mott-isolierende Phase, welche in Experimenten und vorangegangenen Studien gefunden wurde, bestätigt werden kann. Für dieses Material vergleichen wir auch den Einfluss verschiedener möglicher Näherungen der vollen Theorie.

Contents

Acknowledgments

Thank you, *Markus Aichhorn*, for giving me the possibility to do my PhD thesis in your group, and for all your support and advice throughout the last few years. You have always been there for my questions, giving suggestions and new ideas. I appreciate the friendly atmosphere in your group, which is definitely owed to your management style, and all the interesting discussions we had (not just about physics). Finally, I want to thank you for the chance to participate in all the schools, conferences, and collaborations abroad.

Thank you, *Enrico Arrigoni*, for supervising my thesis before Markus's habilitation and for the uncomplicated handling of all the responsibilities that come with that.

Thank you, *Antoine Georges* and *Olivier Parcollet*, for hosting me in Paris, and for the long-lasting collaboration without which this thesis would not be what it is now. Thank you, *Michel Ferrero* and *Priyanka Seth*, for adding to the Paris experience. Thank you, *Oleg Peil*, for the good collaboration in the VASP project. Thank you, all members of the *TRIQS community*, for doing and sharing your work so that others (like me) can profit from it.

Thank you, *Manuel Zingl*, for your friendship, for the good discussions about life, many-body physics and everything and especially for your motivation and ideas whenever I ran out of them, and for the excellent job as chairman of the journal club. Thank you, *Robert Triebl*, for life support when the mathematical aspects of theoretical physics overwhelmed me. Thank you, *Jakob Neumayer*, although you never installed a ventilation in our office. Thank you, *Michael Rumetshofer*, for providing the point of view of a many-body and Bayes expert from outside our group, but especially for spreading your contagious good mood.

Thank you, all the members of the *Institute of Theoretical and Computational Physics*, I always enjoyed the friendly working environment you helped create. Thank you, *Elias Assmann*, for answering my questions about Wien2k, FORTRAN, and physics in general, *Gernot Kapper*, for sharing your expertise in MPI, *Ewald Schachinger* for all the discussions about MaxEnt, and *Daniel Bauernfeind*, for giving me a different perspective on life and physics. Thank you, *Andreas Hirczy*, for taking excellent care of the computer infrastructure and always being motivated to enlighten me about Linux and computers in general. Thank you, *Brigitte Schwarz*, for protecting us from administrative chaos.

Thank you, *Thomas Taucher*, for all the coffee and lunch breaks that significantly improved my morale, and for your friendship in general. Thank you, fellow *Zapo* lovers, for interesting

conversations during lunch time and for hosting me at your *Nudeltag*. Thank you, all my friends and former colleagues, for always lending me an ear and sharing the occasional beer.

Thank you, my dear parents, *Ingrid* and *Gerald Kraberger*, for your unconditional support and for always making me look forward to coming back home to you. Thank you, *Bernhard*, for being a brother that I can always count on.

Thanks to the *Austrian Science Fund* FWF for funding the project Y 746 that I worked for while doing my PhD, the *Collège de France* and *CEA* for financially enabling the stays in Paris, and the *ZID* of TU Graz and the *Vienna Scientific Cluster* for providing the computational resources for this work.

List of symbols and abbreviations

In this list, the meaning of most of the mathematical symbols and abbreviations is given together with a reference to the page where they first appear.

$\mathcal{A}$	integral of the angular part of the Coulomb interaction → p. 37
A_0	non-interacting spectral function → p. 107
$A(\underline{k},\omega)$	spectral function → p. 28
α	hyperparameter → p. 79
$\hat{\alpha}_i$	prefactor in the Dirac equation → p. 49
α_F	fine structure constant → p. 49
b_x	annihilation operator of the bath, destroys an electron with quantum number(s) x in the bath → p. 29
$b_x^\dagger$	creation operator of the bath, creates an electron with quantum number(s) x in the bath → p. 29
β	inverse temperature → p. 29
$\hat{\beta}$	prefactor in the Dirac equation → p. 49
$\mathcal{C}$	crystal-field splitting → p. 55
C	cost function → p. 111
c	speed of light → p. 49
c_x	annihilation operator, destroys an electron with quantum number(s) x → p. 28
$c_x^\dagger$	creation operator, creates an electron with quantum number(s) x → p. 28
χ	small component of the Dirac wave function → p. 51
$\lvert\chi\rangle$	trial orbitals for PWF → p. 31
χ^2	misfit → p. 71
cLDA	constrained local density approximation → p. 36

cRPA	constrained random-phase approximation → p. 36
CTHYB	continuous time Quantum Monte Carlo in hybridization expansion → p. 61
CTINT	continuous time Quantum Monte Carlo in interaction expansion → p. 61
CTQMC	continuous time Quantum Monte Carlo → p. 61
D	default model → p. 79
d_{z^2}, $d_{x^2-y^2}$, d_{xy}, d_{xz}, d_{yz}	cubic harmonics → p. 55
DC	double-counting correction → p. 34
Δ	hybridization function → p. 29
DFT	density functional theory → p. 25
DMFT	dynamical mean-field theory → p. 25
DOS	density of states → p. 27
E	energy → p. 49
E_{corr}	correlation energy from DMFT → p. 42
E_{dc}	double-counting energy → p. 42
$E[\varrho]$	energy functional of the electron density → p. 26
ED	exact diagonalization → p. 124
E_i	many-body eigenenergies → p. 40
ϵ_{bath}	non-interacting Hamiltonian of the bath → p. 29
$\epsilon_{\underline{k}}^{mm'}$	Fourier-transformed hopping Hamiltonian → p. 28
ϵ_{loc}	local non-interacting Hamiltonian → p. 29
$\varepsilon_{\underline{k},\nu}$	band structure (possibly Kohn-Sham) energies → p. 26
η	PAW channel → p. 44
$\mathcal{F}$	tail fit window → p. 70
F	free energy → p. 63
f	free energy density → p. 64
F^k	Slater integral → p. 37
f_ν	filling of the Bloch band ν → p. 32

$F[\varrho]$	universal functional → p. 26
fcsc	fully charge self-consistent → p. 41
FLL	fully-localized limit → p. 35
$\mathcal{G}_0$	non-interacting impurity Green's function, effective Weiss field → p. 29
G_{imp}	interacting impurity Green's function → p. 29
G_{latt}	lattice Green's function → p. 29
G_{loc}	local Green's function → p. 29
GGA	generalized gradient approximation → p. 26
H	Hamiltonian → p. 28
$h_{\underline{k}}$	Kohn-Sham effective one-particle Hamiltonian → p. 27
H_0	non-interacting Hamiltonian → p. 28
H_{int}	interaction Hamiltonian → p. 28
H_{hyb}	hybridization term in the Anderson impurity model → p. 62
H_{lb}	the local and bath Hamiltonian in the Anderson impurity model → p. 62
I^x_m	spectral function of orbital m integrated in window $\mathcal{W}_x$ → p. 111
$\underline{J}$, J_x, J_y, J_z	total angular momentum operator → p. 53
J	Hund's coupling → p. 35
j	total angular momentum quantum number → p. 52
J_K	Hund's coupling in Kanamori parametrization → p. 38
$\underline{k}$	point in reciprocal space, typically in the first Brillouin zone → p. 26
K	kernel of the analytic continuation → p. 79
κ	dielectric function → p. 36
KS	Kohn-Sham → p. 26
ℓ	orbital angular momentum quantum number → p. 52
$\underline{L}$, L_x, L_y, L_z	orbital angular momentum operator → p. 53
λ	prefactor of the SOC term → p. 51
LAPW+LO	linear augmented plane wave plus local orbitals → p. 26
LDA	local density approximation → p. 26

$\mathcal{M}$	matrix mixing the bands for MLWF → p. 31
M	number of correlated orbitals → p. 36
m	mass → p. 49
m_j	total magnetic quantum number → p. 52
m_ℓ	orbital magnetic quantum number → p. 52
m_s	spin magnetic quantum number → p. 52
MLWF	maximally localized Wannier function → p. 31
μ	chemical potential → p. 29
N	number of electrons in the system → p. 26
n	principal quantum number → p. 51
N_{imp}	total occupancy of the impurity → p. 35
n_x	density operator for quantum number(s) x → p. 28
NCA	non-crossing approximation → p. 62
ν	Bloch band index → p. 26
O	overlap matrix of the projected orbitals → p. 32
ω	excitation energy → p. 28
ω_n	(fermionic) Matsubara frequency → p. 29
$\mathcal{P}$	matrix elements of the projection operator for PWF, before orthonormalization → p. 31
P	matrix elements of the projection operator for PWF, after orthonormalization → p. 32
p	momentum → p. 49
PAW	projector-augmented wave → p. 44
PBE	Perdew, Burke, and Ernzerhof → p. 26
$\|\phi_i\rangle$	PAW all-electron partial wave → p. 44
ϕ	large component of the Dirac wave function → p. 51
$\|\tilde{\phi}_i\rangle$	PAW pseudo partial wave → p. 44
Π	polarization function → p. 36
$\psi_{\underline{k},\nu}$	Block wave function → p. 26

$\lvert\tilde{\psi}_{\underline{k},\nu}\rangle$	PAW pseudo wave function → p. 44
$\tilde{p}_i$	PAW projector → p. 44
PWF	projective Wannier function → p. 31
$Q^{\ell m_\ell}$	PAW all-electron partial wave overlap matrix → p. 44
Q_α	cost function in the MaxEnt method → p. 79
$\mathcal{R}$	radial part of the (hydrogen-like) wave function → p. 37
$\underline{R}$	lattice vector → p. 31
$\underline{r}$	spatial position vector, coordinate → p. 26
$\hat{\varrho}$	density matrix → p. 32
$\varrho(\underline{r})$	electron density → p. 25
RPA	random phase approximation → p. 36
$\underline{S}$, S_x, S_y, S_z	spin angular momentum operator → p. 53
S	entropy → p. 79
s	spin quantum number → p. 52
$\hat{\Sigma}$	upfolded self-energy → p. 34
Σ	self-energy → p. 29
σ_x, σ_y, σ_z	Pauli matrices → p. 49
SOC	spin-orbit coupling → p. 49
T	transformation matrix → p. 39
$t_{ij}^{mm'}$	hopping from orbital m on site i to orbital m' on site j → p. 28
τ	imaginary time → p. 62
TF	tail fit → p. 68
TRIQS	Toolbox for Research on Interacting Quantum Systems → p. 30
T_τ	imaginary time-ordering operator → p. 62
$\underline{u}$	parameter vector in singular space → p. 84
U	Coulomb interaction strength → p. 28
U'_K	different-orbital Coulomb interaction strength in Kanamori parametrization → p. 38

U_K	same-orbital Coulomb interaction strength in Kanamori parametrization → p. 38
$u_{\underline{k},\nu}(\underline{r})$	lattice-periodic part of the Bloch wave function → p. 26
U, Ξ, V	SVD of the kernel K → p. 83
V	bare Coulomb operator → p. 36
$v(\underline{r})$	external potential, ionic potential → p. 26
VASP	Vienna Ab-Initio Simulation Package → p. 26
$v_H(\underline{r})$	Hartree potential → p. 27
$v_{KS}(\underline{r})$	Kohn-Sham effective one-body potential → p. 27
$v_{xc}(\underline{r})$	exchange-correlation potential → p. 27
$\mathcal{W}$	subset of the bands in PWF, e.g., an energy window → p. 32
W	screened Coulomb interaction operator → p. 36
w	Wannier function → p. 31
$Y_\ell^{m_\ell}$	spherical harmonics → p. 37
$\mathcal{Z}$	partition function → p. 62
z	frequency in the complex plane → p. 29
ζ	hybridization between impurity and bath → p. 29
Z_N	atomic number → p. 50

1 Introduction

In our technology-driven time, a lot of innovation comes from the development of new materials with properties that often were previously unheard of. For instance, the semiconductor revolution [1], which started as an achievement in materials design and control, has already permeated society, and (unconventional) superconductivity [2] is used in many special technical applications. Quite recently, the advent of topological insulators [3] has sparked a huge interest, but still more work has to be done to mature that field. In all these areas, fundamental research is performed in order to ensure further advancement. What is truly amazing is that all these technologies and the underlying phenomena are based on the same basic principles of physics, i.e., quantum theory (including corrections to account for the results of the special theory of relativity), which was formulated about one hundred years ago. The plethora of different behaviors of matter that we are either familiar with or that fascinate us, emerge just from different ways of arranging atoms. The task of a materials scientist is, thus, to find an efficient and practicable way of doing so in order to create the desired effect.

Industrially and experimentally, this is no easy feat. There are many different knobs to turn; some of the routes that are often explored [4] are heterostructuring or layering of materials (which, in addition to the interplay between two different materials can also produce interesting effects due to the dimensional reduction and due to strain exerted on one constituent by the other), coating of surfaces, doping, changing the levels of disorder either chemically or physically (e.g., annealing), chemical functionalization, and going to lower (or higher) temperatures. Theoretical efforts to explain these processes are usually ambitious, but normally a satisfying theoretical model providing a deeper understanding can be found. Astonishingly, even simple models can give rise to extraordinarily rich phase diagrams [5].

The task of theoretical and computational materials science should, however, not be reduced to the interpretation of experimental findings. Rather, the highly challenging mission is to find, by means of computer simulation, ever new ways to combine and put to use the basic pieces. The holy grail of this field is predictive power, which is a necessary precondition for discovering useful compounds. Then, given a sufficiently computationally lightweight implementation, a screening of many different promising candidate materials can be performed much more efficiently than in the laboratory [6]. On that road, a continuous improvement of the methods is key.

Of all the possible basic physical concepts that can be realized in a crystal, one of the most exciting ones are strongly-correlated electrons. The seemingly trivial Coulomb interaction between the electrons is the root cause for such different, intriguing phenomena as Mott physics, charge-density

waves, spin-density waves, magnetic order, unconventional superconductivity, and the Kondo effect [7]. These are, thus, archetypes of emerging phenomena. From the point of view of a computational physicist, finding and exploiting ways to trick the exponential wall one inexorably faces when dealing with interacting many-electron systems is a highly stimulating motivation.

The advent of the dynamical mean-field theory (DMFT) in the early 1990s [8–10] allowed the treatment of strongly-correlated systems, i.e., systems where the Coulomb interaction cannot be included in an (effective) one-particle picture, without a bias towards the itinerant or localized picture. This Green's function-based theory has soon been used on top of ab-initio calculations, typically employing density functional theory (DFT), in order to describe real correlated materials [11]. Since then, the boundary of what is feasible has been pushed time and again.

Sometimes the limiting factor for DFT+DMFT calculations is the size of the system, which already makes DFT slow. There exists a very efficient DFT package that is often used to treat crystals with large unit cells, the Vienna Ab-Initio Simulation Package (VASP). Oleg Peil [12] has developed, together with the VASP group, an interface between VASP and TRIQS, the Toolbox for Research on Interacting Quantum Systems, which enables users of that DFT code to profit from the tools developed for DMFT calculations. The author of this thesis has, in close collaboration with Oleg Peil, tested and improved that framework; this is presented in section 2.4.

In recent years, especially driven by the advances in the field of topological insulators [3], there has been an increased interest in the interplay between strongly-correlated electrons and the spin-orbit coupling (SOC). The latter is a feature of electrons in atoms with heavy nuclei that arises because of the combination of quantum mechanics with Einstein's special theory of relativity. Strong electron-electron interactions together with a large SOC can be found whenever atoms with open $4d$, $5d$ (e.g., in the iridates and osmates that were investigated in this thesis) or f-shells are present.

In the literature, several DFT+DMFT studies of systems with non-negligible SOC can be found. Usually, however, the matrix structure of the involved Green's functions (i.e., the non-zero off-diagonal elements) and/or the interaction beyond the density-density terms was ignored [13–16] (studies treating the full problem are Refs. [17, 18]). The goal and main theme of this thesis is to allow full calculations using matrix-valued quantities. This necessitates several adaptions of the well-established methods and their implementation (for which we use TRIQS), all of which are discussed in detail in this work.

The contents of this thesis are the following. First, an introduction to the framework of DFT+DMFT calculations (chapter 2) and the basics of the SOC (chapter 3) is given. Then, the changes that have to be made to the central tool used in our calculations, the so-called impurity solver (its role is discussed already in chapter 2), are discussed in chapter 4. Furthermore, two related topics, namely avoiding the sign problem (section 4.4) and performing the high-frequency or "tail fit" (section 4.5), are considered there. Once the DFT+DMFT calculation was successful, often an analytic continuation has to be executed to be able to better interpret the results. Applying this theory to matrix-valued Green's functions turns out to be non-trivial; the full

account of the problem and its solution is given in chapter 5.

Finally, this scheme is applied to two systems of recent interest. On the one hand, a heterostructure of $SrTiO_3$ and $SrIrO_3$ is considered (chapter 6), where also an approach for performing a reduction of the number of orbitals that have to be included in the calculation is introduced. In this structure, the correction provided by the DMFT on top of the DFT calculation is not very large. This is in stark contrast to the second compound we focus on, Sr_2MgOsO_6 (chapter 7). There, DFT predicts a metal but experiments clearly show an insulating behavior. Only the inclusion of strong electronic correlations and the SOC allows to correctly describe this in the paramagnetic phase. On top of presenting these results, different potentially applicable approximations are benchmarked.

2 Ab-initio calculations of correlated materials

In this chapter, the density functional theory plus dynamical mean-field theory (DFT+DMFT) framework, enabling the calculation of the electronic properties of strongly-correlated materials from first principles, is introduced. For the purpose of this chapter, everything is treated non-relativistically; the incorporation of relativistic effects into this theory is handled in chapter 3. At first, the two building blocks of that formalism are introduced, namely DFT in section 2.1 and DMFT in section 2.2. Afterwards, the combination of these two theories in the DFT+DMFT approach is explained in section 2.3. Finally, the TRIQS interface to VASP is discussed in section 2.4.1. While the majority of this chapter consists of a literature review, section 2.4.2 is original work performed by the author of this thesis in order to benchmark the implementation of the TRIQS-VASP interface. The author helped to improve the interface, also by suggesting changes to the source code.

2.1 Density functional theory (DFT)

This overview of density functional theory is based on Walter Kohn's Nobel lecture [19] and the excellent book by Richard M. Martin [20].

Describing crystals from first principles means that the only ingredients entering the calculation are the geometry information, i.e., the unit cell dimensions and the position and atomic number of the ions, the number of electrons, and the fundamental forces acting between the constituents (ions and electrons) of the material. A quantum-mechanical description is typically achieved by writing down the Hamiltonian of that system and solving the according time-independent Schrödinger equation. However, even after performing the so-called Born-Oppenheimer approximation, which fixates the positions of the ions because their dynamics happen on a much slower time scale than the electron dynamics, solving that equation is prohibitively expensive for any realistically large system. The main problem is the exponential growth of the Hilbert space with the number of electrons as soon as there is an interaction between the individual electrons.

In 1964, Hohenberg and Kohn [21] published their theorem stating that all the ground-state properties of the interacting electron gas are uniquely determined by the ground-state electron density $\varrho(\underline{r})$ alone; there is no need to know the wave function of the system. In contrast to the

latter, which depends on the 3^N coordinates of the N electrons, the electron density is a function of just the three spatial dimensions $\underline{r}$. The theorem expresses that, in particular, the total energy is a functional $E[\varrho]$ of the electron density. The functional can be split into two contributions,

$$E[\varrho] = F[\varrho] + \int d^3r\, v(\underline{r})\, \varrho(\underline{r}), \tag{2.1}$$

where $F[\varrho]$ is a *universal* functional of the electron density and $v(\underline{r})$ is the "external" potential (typically generated by the ions in the crystal). There exists a variational principle, which means that the minimal value (with respect to different electron densities) of the functional $E[\varrho]$ is achieved for the ground-state density.

While the theoretical concepts of the Hohenberg-Kohn theorem lie at the foundation of density-functional theory, it does not by itself allow to solve for the ground-state density and energy of a given system. This is made possible by a framework developed by Kohn and Sham in 1965 [22]. There, the interacting electron gas is mapped onto a non-interacting electron gas; that means that the resulting effective Hamiltonian is separable in the individual electrons, which allows a solution of the corresponding Schrödinger equation, which is called Kohn-Sham (KS) equation in this context. The universal functional $F[\varrho]$ from Hohenberg-Kohn theory enters as part of the effective one-body potential. The ground-state density and energy is determined self-consistently by repeatedly solving the KS equation and then updating the effective KS potential according to the electron density. As there is no known expression for the functional, in practice approximate expressions have to be used. Some popular choices for the functional include the local density approximation (LDA) and different flavors of the generalized gradient approximation (GGA), one of which is the often-used functional by Perdew, Burke, and Ernzerhof (PBE) [23].

KS DFT is implemented in many commercially or freely available packages, among them Wien2k [24] and the Vienna Ab-Initio Simulation Package (VASP) [25–29], which were used in this thesis. In the following, we will present the individual steps of a KS DFT calculation in more detail.

We will only consider periodic crystals, which are defined by a unit cell consisting of three lattice vectors and the ion positions within the cell. In the effective one-electron picture, the wave functions follow Bloch's theorem,

$$\psi_{\underline{k},\nu}(\underline{r}) = e^{i\underline{k}\,\underline{r}} u_{\underline{k},\nu}(\underline{r}), \tag{2.2}$$

where the wave function $\psi_{\underline{k},\nu}(\underline{r})$ at a point $\underline{k}$ in reciprocal space (typically in the first Brillouin zone) with the band index ν is obtained from the lattice-periodic part of the wave function $u_{\underline{k},\nu}(\underline{r})$. Within DFT we want to calculate the KS orbitals $|u_{\underline{k},\nu}\rangle$, expressed in a convenient basis, e.g., the linear augmented plane wave plus local orbitals (LAPW+LO) basis in Wien2k or a plane-wave basis in VASP. The corresponding "energy" eigenvalues $\varepsilon_{\underline{k},\nu}$ of the KS orbitals in the KS equation,

$$h_{\underline{k}}\, |u_{\underline{k},\nu}\rangle = \varepsilon_{\underline{k},\nu}\, |u_{\underline{k},\nu}\rangle\,, \tag{2.3}$$

with an effective one-body Hamiltonian $h_{\underline{k}}$, form the KS band structure.

In a DFT calculation, after an appropriate initialization of all quantities, first the KS Hamiltonian $h_{\underline{k}}$ is constructed from the electron density $\varrho(\underline{r})$ (in Wien2k, this is done by the program `lapw0`),

$$h_{\underline{k}}(\underline{r}) = -\frac{1}{2}(\nabla + i\underline{k})^2 + v_{KS}(\underline{r}). \tag{2.4}$$

It consists of the kinetic energy term and the effective one-body potential $v_{KS}(\underline{r})$, which is

$$v_{KS}(\underline{r}) = v(\underline{r}) + v_H(\underline{r}) + v_{xc}(\underline{r}), \tag{2.5}$$

i.e., the sum of the external potential, the Hartree potential $v_H(\underline{r})$ and the exchange-correlation potential $v_{xc}(\underline{r})$. The choice of the exchange-correlation potential is what differentiates different DFT functionals. As a next step, the KS equation (2.3) is solved (program `lapw1` in Wien2k) to obtain the KS energies $\varepsilon_{\underline{k},\nu}$ and the eigenstates $u_{\underline{k},\nu}(\underline{r})$. From the wave functions, the updated electron density is calculated (`lapw2` in Wien2k) as

$$\varrho(\underline{r}) = \sum_{\underline{k},\ \nu\ \text{occ.}} u^*_{\underline{k},\nu}(\underline{r}) u_{\underline{k},\nu}(\underline{r}), \tag{2.6}$$

where the $\underline{k}$-sum is carried out over the first Brillouin zone and ν is summed only over occupied bands (the Fermi level is determined such that the total number of electrons is correct). As a technicality, the charge density is then mixed (`mixer` in Wien2k[1]) with the previous one to suppress oscillatory behavior over the course of the iterations. Then, the loop continues by constructing a KS Hamiltonian from that new charge density; this process is iterated until a convergence criterion is met.

The mapping between the interacting electron system and the one-particle formulation in KS theory only ensures that the total ground-state energy and the ground-state electron density are the same for both systems[2], but the KS energies and wave functions are, in principle, just auxiliary quantities. While it was later found that the differences of the KS eigenvalues are an approximation in zeroth order in the electron-electron interaction of the excitation energies [30], the spectra (i.e., densities of states DOS) obtained from the KS energies often fail to correctly describe experimental results. Depending on the system under investigation, this can be remedied by using hybrid functionals or by employing the GW approximation. In this thesis, we will focus on an approach for strongly-correlated electrons, DFT+DMFT.

[1] Actually, in Wien2k also core states have to be calculated, which is done with the program `lcore` before the mixing.

[2] In practice, due to the necessary approximation of the functional, they are not the same.

2.2 Dynamical mean-field theory (DMFT)

This section is a concise summary of the review Ref. [10], extended to the multi-orbital case and focusing only on the "recipe" for DMFT calculations without providing the derivations; for them, we refer the reader to the original review article.

The Hamiltonian of a non-interacting system in the (possibly effective) independent-electron picture can be written as

$$H_0 = \sum_{ij,\sigma} t_{ij}^{mm'} c_{im\sigma}^\dagger c_{jm'\sigma} = \sum_{\underline{k},\sigma} \epsilon_{\underline{k}}^{mm'} c_{\underline{k}m\sigma}^\dagger c_{\underline{k}m'\sigma}, \tag{2.7}$$

where $t_{ij}^{mm'}$ is the hopping from orbital m on site i to orbital m' on site j, $c_{im\sigma}^\dagger$ is an operator creating and $c_{im\sigma}$ destroying an electron with spin σ at orbital m on site i, $c_{\underline{k}m\sigma}^\dagger$ is an operator creating and $c_{\underline{k}m\sigma}$ destroying an electron with quantum number $\underline{k}$ and spin σ in orbital m, and $\epsilon_{\underline{k}}^{mm'}$ is the Fourier transform of the hopping. When diagonalizing $\epsilon_{\underline{k}}^{mm'}$ at each $\underline{k}$-point, one obtains as eigenenergies the band structure $\varepsilon_{\underline{k},\nu}$.

Strongly correlated systems cannot be described in the one-electron framework anymore, which means that the band-structure picture breaks down. The electron-electron interaction has to be explicitly accounted for, not just by means of an effective one-electron potential. This means that the hopping Hamiltonian has to be extended to include interaction terms H_{int}, i.e., the Hubbard model

$$H = H_0 + H_{int}. \tag{2.8}$$

Typically, the interaction term is local (i.e., $\underline{k}$-independent). In the simplest, one-band case it is the Hubbard interaction

$$H_{int}^{\text{Hubbard}} = \sum_m U n_{m\uparrow} n_{m\downarrow} = \sum_m U c_{m\uparrow}^\dagger c_{m\uparrow} c_{m\downarrow}^\dagger c_{m\downarrow}, \tag{2.9}$$

where U is the Coulomb interaction strength and $n_{m\sigma} = c_{m\sigma}^\dagger c_{m\sigma}$ is the density operator at site m for spin σ. In the multi-orbital case, the most general interaction can be written as

$$H_{int} = \sum_{\substack{mm'm''m''' \\ \sigma\sigma'\sigma''\sigma'''}} U_{mm'm''m'''}^{\sigma\sigma'\sigma''\sigma'''} c_{m\sigma}^\dagger c_{m'\sigma'}^\dagger c_{m'''\sigma'''} c_{m''\sigma''}. \tag{2.10}$$

Rather than considering the problem solved once the one-particle eigenenergies (i.e., the band structure) are known, for strongly interacting systems Green's function techniques are used to get (possibly $\underline{k}$-dependent) spectral functions $A(\underline{k}, \omega)$ describing the excitation spectra as function of an excitation energy ω. A very successful method that is biased neither towards the localized, atomic-like strong-interaction limit nor towards the itinerant, weak-interaction limit is the dynamical mean-field theory (DMFT). In that theory, the Hubbard model is mapped self-consistently onto the Anderson impurity model, which consists of a strongly-correlated impurity

coupled to a non-interacting bath. The Anderson impurity model is given by the Hamiltonian

$$H = \sum_{mm',\sigma} \epsilon_{loc}^{mm'} c_{m\sigma}^{\dagger} c_{m'\sigma} + H_{int} + \sum_{p,\sigma} \epsilon_{bath}^{p} b_{p\sigma}^{\dagger} b_{p\sigma} + \sum_{mp,\sigma} \zeta_{mp} (c_{m\sigma}^{\dagger} b_{p\sigma} + b_{p\sigma}^{\dagger} c_{m\sigma}), \tag{2.11}$$

where the terms are the local non-interacting Hamiltonian of the impurity described by $\epsilon_{loc}^{mm'}$, the interaction of the impurity, the non-interacting Hamiltonian of the bath described by ϵ_{bath} with creation and annihilation operators $b^{\dagger}$ and b (for the bath), and the hybridization between the impurity and the bath, given by matrix elements ζ. In the Green's function picture, it is possible to describe the bath by the hybridization function

$$\Delta^{mm'}(z) = \sum_{p} \frac{\zeta_{mp}^{*} \zeta_{m'p}}{z - \epsilon_{bath}^{p}}, \tag{2.12}$$

effectively integrating out the bath so that there is just a matrix index for the impurity orbitals. Here, z is a frequency in the complex plane, typically either $z = \omega + i0^{+}$ for the retarded Green's function or $z = i\omega_n$ for the Matsubara Green's function with (fermionic) Matsubara frequencies $\omega_n = \frac{(2n+1)\pi}{\beta}$ at inverse temperature β. Then, the non-interacting Green's function of the impurity model is

$$\mathcal{G}_0^{mm'}(z) = (z - \epsilon_{loc}^{mm'} - \Delta^{mm'}(z))^{-1}. \tag{2.13}$$

In the multi-orbital case, the Green's function, the local Hamiltonian, and the hybridization are all matrices, and the inversion has to be carried out as a matrix inversion. An impurity solver can be used to calculate, from that $\mathcal{G}_0^{mm'}(z)$, an interacting impurity Green's function $G_{imp}^{mm'}(z)$, which fulfills Dyson's equation

$$\left(G_{imp}^{mm'}(z)\right)^{-1} = \left(\mathcal{G}_0^{mm'}(z)\right)^{-1} - \Sigma^{mm'}(z). \tag{2.14}$$

The effect of the electron-electron interaction is contained in the self-energy $\Sigma^{mm'}(z)$.

The Green's function of the lattice (i.e., Hubbard) model is given by

$$G_{latt}^{mm'}(\underline{k}, z) = (z - \epsilon_{\underline{k}}^{mm'} + \mu - \Sigma^{mm'}(\underline{k}, z))^{-1}, \tag{2.15}$$

where μ is the chemical potential that is adjusted to obtain the correct electron filling. Within the DMFT, the self-energy $\Sigma_{mm'}(\underline{k}, z)$ is approximated by the local, i.e. k-independent, self-energy $\Sigma_{mm'}(z)$ of the Anderson impurity model. The local Green's function can be calculated from the lattice Green's function as

$$G_{loc}^{mm'}(z) = \sum_{\underline{k}} G_{latt}^{mm'}(\underline{k}, z), \tag{2.16}$$

where the $\underline{k}$-sum is a correctly weighted summation across the first Brillouin zone. These local quantities allow to construct a connection between the lattice and the impurity model: from the local Green's function $G_{mm'}^{loc}(z)$, an effective non-interacting impurity Green's function can be

obtained using

$$\left(\mathcal{G}_0^{mm'}(z)\right)^{-1} = \left(G_{loc}^{mm'}(z)\right)^{-1} + \Sigma^{mm'}(z); \tag{2.17}$$

that $\mathcal{G}_0$ is analogous to the Weiss field in classical mean-field theory. The solution of the corresponding impurity model yields the impurity Green's function G_{imp} and the self-energy $\Sigma^{mm'}(z)$. This self-energy can the be used to construct, once more, the lattice and, consequently, the local Green's function. If the impurity Green's function G_{imp} matches the local Green's function G_{loc}, the DMFT self-consistent point is reached. Otherwise, it is possible to iterate the construction of a G_{loc}, the mapping onto an effective impurity problem $\mathcal{G}_0$ and the solution of the impurity problem until convergence is reached.

The starting point of Σ does influence the calculation in two ways: First, choosing a "good" initial self-energy can lead to much faster convergence. Second, it is possible that there is more than one self-consistent fixed point in the DMFT loop; in that case, the choice of the initial Σ decides which self-consistent solution will be reached. One example for the existence of several DMFT solutions is the hysteresis found in the Mott transition [31, 32], i.e., the value of U where the transition occurs changes whether one uses a metallic or insulating self-energy as starting point.

In summary, a DMFT calculation consists of the following steps:

1. Initialize Σ,
2. calculate G_{loc} from Σ using (2.15) and (2.16),
3. map the problem onto an impurity model by constructing the effective Weiss field $\mathcal{G}_0$ using (2.17),
4. solve the impurity problem to obtain G_{imp} and an updated Σ which are related by equation (2.14),
5. check if $G_{loc} = G_{imp}$; if yes, the problem has been solved in DMFT, if not, perform another iteration starting from step 2.

2.3 Density functional theory plus dynamical mean-field theory (DFT+DMFT)

The combination of the DFT and the DMFT allows to calculate the properties of strongly-correlated materials from first principles. This section describes the formalism, some problems and steps to overcome, and their implementation and use in the Toolbox for Research on Interacting Quantum Systems (TRIQS) [33, 34].

2.3.1 Wannier functions

The Kohn-Sham states used in DFT are Bloch states with a particular wave vector $\underline{k}$, which implies that they are very delocalized in real space. This is at odds with the basic concept of the DMFT, which requires impurities described by local states. Therefore, Wannier orbitals have to be constructed out of the Bloch states to obtain a localized basis for the DMFT calculation. In that step, also the number of orbitals has to be reduced to a number that can be treated by the impurity solver, typically on the order of 3-7 for highly accurate, modern impurity solvers.

Wannier functions are the Fourier transforms of Bloch states; there are different ways of constructing them from a DFT calculation. First, maximally localized Wannier functions (MLWF) $|w_{\underline{R},m}\rangle$ can be constructed [35, 36]:

$$|w_{\underline{R},m}\rangle = \sum_{\underline{k}} e^{i\underline{k}\,\underline{R}} \sum_{\nu} \mathcal{M}^{m\nu}_{\underline{k}} \, |\psi_{\underline{k},\nu}\rangle \,, \tag{2.18}$$

where the $\underline{k}$-summation is done correctly weighted across the first Brillouin zone (as usual), $\underline{R}$ is a lattice vector and $\mathcal{M}$ is a matrix mixing the bands before the Fourier transform. As indicated by the matrix $\mathcal{M}$, there is the freedom to choose a unitary matrix to mix the Bloch states of different bands at a certain $\underline{k}$-point [36]. That freedom is exploited to find a set of Wannier functions that show a minimal spread (i.e., the minimal sum of the variances of the position operator evaluated with the Wannier functions). This procedure is implemented in the *Wannier90* code [37], for which there are interfaces from many DFT codes. Amongst other quantities, the MLWF procedure produces a hopping Hamiltonian, or equivalently a Hamiltonian $\epsilon^{mm'}_{\underline{k}}$; ideally the band structure from that Hamiltonian matches the Kohn-Sham band structure perfectly. That $\epsilon^{mm'}_{\underline{k}}$ can be straightforwardly used in the DMFT as described in section 2.2.

However, the use of MLWF has a few disadvantages when used for DFT+DMFT. Typically, the construction of MLWF requires user interaction, which prohibits a fully automatized implementation that is desirable especially in the context of fully charge self-consistent DFT+DMFT (see below). Furthermore, using the $\epsilon^{mm'}_{\underline{k}}$ from MLWF is not equivalent to the construction of an effective Hamiltonian in the framework of the Mori-Zwanzig projection formalism [38, 39].

There is an alternative to MLWF, namely projective Wannier functions (PWF) [40–42]. There, a set of localized (possibly atomic-like) orbitals $|\chi^{\alpha\sigma}_m\rangle$ (i.e., orbital m at site/atom α with spin σ) is used to project out a localized basis from the Bloch states. The (temporary) projection operator has the matrix elements

$$\mathcal{P}^{\alpha\sigma}_{m\nu}(\underline{k}) = \langle \chi^{\alpha\sigma}_m | \psi_{\underline{k},\nu} \rangle \,. \tag{2.19}$$

Typically, the number of trial orbitals is lower than the number of bands, which means that $\mathcal{P}^{\alpha\sigma}$ is a non-square matrix. The $\mathcal{P}$ matrix projects out orbitals

$$|\tilde{\chi}^{\alpha\sigma}_m(\underline{k})\rangle = \sum_{\nu\in\mathcal{W}} \mathcal{P}^{\alpha\sigma *}_{m\nu}(\underline{k}) \, |\psi_{\underline{k},\nu}\rangle \,. \tag{2.20}$$

The summation is restricted to a subset of the bands, $\mathcal{W}$, which is usually defined by an energy window. Therefore, the overlap matrix of the projected orbitals, is

$$O^{\alpha\alpha'}_{mm'}(\underline{k},\sigma) = \langle \tilde{\chi}^{\alpha\sigma}_{m}(\underline{k}) | \tilde{\chi}^{\alpha'\sigma}_{m'}(\underline{k}) \rangle = \sum_{\nu\in\mathcal{W}} \mathcal{P}^{\alpha\sigma}_{m\nu}(\underline{k}) \mathcal{P}^{\alpha'\sigma *}_{m'\nu}(\underline{k}) \neq \delta_{mm'}\delta_{\alpha\alpha'}, \tag{2.21}$$

i.e., the $|\tilde{\chi}^{\alpha\sigma}_{m}(\underline{k})\rangle$ are not orthonormal. However, it is possible to orthonormalize them using a simple procedure (which is equivalent to Löwdin orthonormalization [43]), to obtain the PWF

$$|w^{\alpha\sigma}_{m}(\underline{k})\rangle = \sum_{\alpha' m'} (O^{-1/2}(\underline{k},\sigma))^{\alpha\alpha'}_{mm'} \, |\tilde{\chi}^{\alpha'\sigma}_{m'}(\underline{k})\rangle \, . \tag{2.22}$$

This procedure is only possible as long as the overlap matrix is not singular, which happens if a trial function has hardly any weight within the projection window $\mathcal{W}$. The projector matrices connecting the PWF $|w^{\alpha\sigma}_{m}(\underline{k})\rangle$ to the Bloch bands are

$$P^{\alpha\sigma}_{m\nu}(\underline{k}) = \langle w^{\alpha\sigma}_{m}(\underline{k}) | \psi_{\underline{k},\nu} \rangle = \sum_{\alpha' m'} (O^{-1/2}(\underline{k},\sigma))^{\alpha\alpha'}_{mm'} \mathcal{P}^{\alpha'\sigma}_{m'\nu}(\underline{k}). \tag{2.23}$$

Due to the orthonormalization, we have

$$\sum_{\nu} P^{\alpha\sigma}_{m\nu}(\underline{k}) P^{\alpha'\sigma *}_{m'\nu}(\underline{k}) = \delta_{mm'}\delta_{\alpha\alpha'}, \tag{2.24}$$

or, in matrix notation, $P^{\alpha\sigma}(\underline{k}) {P^{\alpha'\sigma}}^{\dagger}(\underline{k}) = \mathbb{1}$. However, the other way round, ${P^{\alpha\sigma}}^{\dagger}(\underline{k}) P^{\alpha'\sigma}(\underline{k}) \neq \mathbb{1}$; therefore, the projector matrices P are not unitary.

The density matrix $\hat{\varrho}$ of the resulting Wannier orbitals can be calculated using a point integration

$$\hat{\varrho}^{\alpha\sigma}_{mm'}(\underline{k}) = \sum_{\nu} P^{\alpha\sigma}_{m\nu}(\underline{k}) f_{\nu}(\underline{k}) P^{\alpha\sigma *}_{m'\nu}(\underline{k}), \tag{2.25}$$

where $f_{\nu}(\underline{k})$ is the filling of the Bloch band ν. As the corresponding local density matrix $\hat{\varrho}^{\alpha\sigma}_{mm'} = \sum_{\underline{k}} \hat{\varrho}^{\alpha\sigma}_{mm'}(\underline{k})$ is a deciding factor for the strength of the correlations in the material (see, e.g., Ref. [44]), the projection window $\mathcal{W}$ has to be chosen with care to avoid a bias in the calculation. Figure 2.1 illustrates the consequences of the choice of the projection window on the filling of the Wannier orbital. When cutting away only filled states with the window, the filling decreases, while it increases when only empty states are discarded. Of course, it is possible to choose a window where the two effects compensate and the filling does not change, when cutting away both filled and unfilled bands.

It is possible to construct a Hamiltonian in the space of PWF much like with MLWF by *downfolding* the Bloch Hamiltonian

$$\epsilon^{\alpha\sigma}_{mm'}(\underline{k}) = \sum_{\nu} P^{\alpha\sigma}_{m\nu} \varepsilon_{\underline{k},\nu} P^{\alpha\sigma *}_{m'\nu}. \tag{2.26}$$

As mentioned above, usually there are more Bloch bands than PWF per $\underline{k}$-point and these Bloch

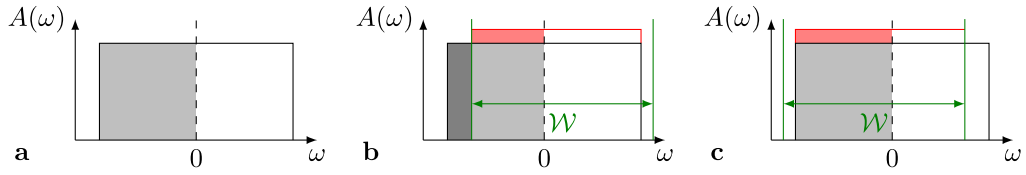

Figure 2.1: Qualitative sketch of the dependency of the density of the Wannier orbital on the projection window. (a) The band is filled (as indicated by the gray shaded area) up to the chemical potential, which is set to $\omega = 0$. The orbital is normalized, i.e. the integral over the spectral function is one, and it is half-filled. (b) When projecting out in a window $\mathcal{W}$ that cuts away filled bands (the cut-away weight is indicated by the dark gray shaded area), but no unfilled bands, the norm of the orbital drops to a value lower than one. After the orthonormalization, the band (red line) is normalized again. But as the filling of the cut-away states (dark gray shaded) is lower than the additional filling due to normalization (red shaded), the filling of the normalized orbital is lower than one half. (c) When cutting away unfilled bands by the projection window $\mathcal{W}$, but no filled bands, once more the norm drops. After the orthonormalization, the band (red line) is normalized again. However, the filling increases (by the red shaded area) to a value higher than one half.

bands are often hybridized, i.e., they show different band character. Then, the corresponding entry of the projector, $P^{\alpha\sigma}_{m\nu}$, will not be one. Let us now assume, for example, that we want to use one PWF to describe two Bloch bands, one with "target weight" 0.6 and one with "target weight" 0.4 (i.e., the character of the PWF matches the character of the Bloch band only by 60% and 40%). Then, the energy of the PWF obtained by the downfolding procedure (2.26) will be in-between the energies of the two involved bands (see figure 2.2). Consequently, there is just one band where there used to be two and it matches neither of the original bands[3]. Note that this is a rather extreme example that does not reflect what is typically encountered in practice. Whenever the projectors P are unitary (this can only be the case when the number of Bloch states and the number of projected orbitals match), this problem does not occur[4]. This is, in particular, the case for MLWF as long as no disentanglement is used.

In principle, one could use the $\epsilon^{\alpha\sigma}_{mm'}(\underline{k})$ from (2.26) to perform DMFT just as described in section 2.2 – the corresponding local Green's function, as obtained when using (2.26) in (2.15) and then (2.16), would then be

$$\tilde{G}^{\alpha\sigma,mm'}_{loc}(z) = \sum_{\underline{k}} \left(z - \sum_{\nu} P^{\alpha\sigma}_{m\nu}(\underline{k}) \varepsilon_{\underline{k},\nu} P^{\alpha\sigma *}_{m'\nu}(\underline{k}) + \mu - \Sigma^{\alpha\sigma}_{mm'}(z) \right)^{-1} \tag{2.27}$$

(the tilde is used to show that this is not what we use in the end). Nevertheless, it is advisable to use a more sophisticated approach that avoids the problem that has just been described. That

[3] Constructing a second PWF could, of course, improve the quality of this approach significantly. However, when dealing with heavily entangled Bloch bands where just a small number of correlated orbitals shall be projected out, adding more PWF is not an option.

[4] In that case, the approaches (2.27) and (2.29) presented below are equivalent.

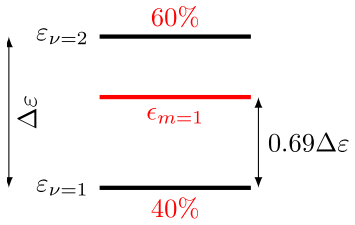

Figure 2.2: Energy level diagram of a system with two Bloch bands (black, $\varepsilon_{\nu=1}$ and $\varepsilon_{\nu=2}$) separated by an energy $\Delta\varepsilon$, where one has 60% and the other has 40% of the character of the PWF. Then, the energy of the Hamiltonian $\epsilon_{m=1}$ of the PWF, downfolded according to (2.26), lies in-between the energies of the Bloch bands, separated from the lower band by an energy $0.6^2\Delta\varepsilon/(0.6^2+0.4^2) = 0.69\Delta\varepsilon$.

better approach will be introduced in the next section.

2.3.2 DFT+DMFT with projective Wannier functions

The theory presented in this section follows Ref. [42].

Instead of working with the downfolded Hamiltonian from (2.26), one can keep the Hamiltonian in Bloch space and rather *upfold* the self-energy

$$\hat{\Sigma}^{\alpha\sigma}_{\nu\nu'}(\underline{k}, z) = \sum_{nn'} P^{\alpha\sigma *}_{n\nu}(\underline{k}) \Sigma^{\alpha\sigma}_{nn'}(z) P^{\alpha\sigma}_{n'\nu'}(\underline{k}) \tag{2.28}$$

and downfold the lattice Green's function, which leads to the local Green's function

$$G^{\alpha\sigma,mm'}_{loc}(z) = \sum_{\underline{k}} \sum_{\nu} P^{\alpha\sigma}_{m\nu}(\underline{k}) \left(z - \varepsilon_{\underline{k},\nu} + \mu - \hat{\Sigma}^{\alpha\sigma}_{\nu\nu'}(\underline{k}, z) + \mathrm{DC} \right)^{-1} P^{\alpha\sigma *}_{m'\nu}(\underline{k}). \tag{2.29}$$

Using that G_{loc}, one can perform the usual DMFT steps of calculating the impurity Weiss field $\mathcal{G}_0$, solving the impurity problem and getting back a new self-energy (just as discussed in section 2.2). That self-energy is then upfolded according to (2.28) and subsequently reinserted into (2.29). Adjusting the chemical potential μ to get the correct filling is done in the upfolded space, i.e., before downfolding the lattice Green's functions.

There is one slight complication, the double-counting correction DC. As laid out in section 2.1, the effects of the interaction Hamiltonian H_{int} are already included in KS-DFT in the effective one-electron picture. Therefore, adding the full interaction by means of the DMFT leads to an overestimation of the correlation, which has to be corrected by means of the double counting term DC. There have been several proposals of how to choose the DC [45–49], among them the

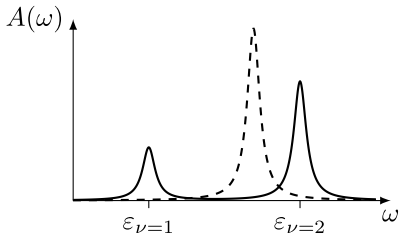

Figure 2.3: Spectral function $A(\omega) = \lim_{\gamma\to 0^+}(-\operatorname{Im} G(\omega+i\gamma)/\pi)$ (plotted for $\gamma = 0.05\Delta\varepsilon$) of the model introduced for figure 2.2. Once (solid line), the approach to downfold the Green's function as in (2.29) is used, once (dashed line), the approach to downfold the Hamiltonian as in (2.27).

fully-localized limit (FLL) [45], which was used throughout this work and reads

$$(\mathrm{DC})^{\sigma}_{mm'} = \delta_{mm'}\left(U\cdot\left(N_{imp}-\frac{1}{2}\right)-J\cdot\left(N^{\sigma}_{imp}-\frac{1}{2}\right)\right), \tag{2.30}$$

where U is the average Coulomb interaction and J is Hund's coupling; it is assumed that the interaction is parametrized in the Slater picture (see below). The total occupancy of the impurity is N_{imp}, and the occupancy per spin channel is N^{σ}_{imp}. The value of the double-counting correction for the density of the initial non-interacting local Green's function serves as a reasonable initial value of Σ (see also the discussion in section 2.2), since it is a good estimate of the Hartree-Fock energy of the system (which is the value of $\lim_{\omega_n\to\infty}\Sigma(i\omega_n)$).

When using the projection formalism on the Green's function rather than the Hamiltonian, the information of the Bloch bands is better preserved when going to the low-energy correlated subspace model. Coming back to the two-band model represented by one PWF introduced for figure 2.2, the spectral function resulting from downfolding the non-interacting (i.e., $\Sigma = 0$ and $\mathrm{DC} = 0$) Green's function can be found in figure 2.3. There are now two peaks at the correct positions rather than the one peak that results from the one level of the downfolded Hamiltonian. The ratio of the peak heights of the two bands with 0.4 and 0.6 PWF character is $0.4^2/0.6^2$. Furthermore, the non-interacting limit, i.e., $\Sigma = 0$, naturally reproduces the DFT result, which is not guaranteed with a downfolded Hamiltonian.

2.3.3 Parametrization of the interaction

This section is presented as in Refs. [50, 51].

The most general expression for a static, local interaction term in the Hubbard model (2.10) is determined by a Coulomb interaction matrix $U^{\sigma\sigma'\sigma''\sigma'''}_{mm'm''m'''}$. Given a set of orbitals $w^{\sigma}_{m}(\underline{r})$, the bare interaction matrix can be calculated as

$$(U_{bare})^{\sigma\sigma'\sigma''\sigma'''}_{mm'm''m'''} = \int d^3r\, d^3r'\, w^{\sigma *}_{m}(\underline{r})\, w^{\sigma'''}_{m'''}(\underline{r})\,\frac{1}{|\underline{r}-\underline{r}'|}\, w^{\sigma'*}_{m'}(\underline{r}')\, w^{\sigma''}_{m''}(\underline{r}'), \tag{2.31}$$

where $V(\underline{r},\underline{r}') = 1/|\underline{r}-\underline{r}'|$ is the bare Coulomb operator. However, the uncorrelated bands *screen* the interaction, which has to be taken into account. Therefore, the bare interaction is always too big. Given the screened interaction operator

$$W(\underline{r},\underline{r}',\omega) = V(\underline{r},\underline{r}')/\kappa(\underline{r},\underline{r}',\omega), \tag{2.32}$$

with the dielectric function κ, the screened interaction is

$$U^{\sigma\sigma'\sigma''\sigma'''}_{mm'm''m'''}(\omega) = \int d^3r\, d^3r'\, w^{\sigma *}_m(\underline{r})\, w^{\sigma'''}_{m'''}(\underline{r})\, W(\underline{r},\underline{r}',\omega)\, w^{\sigma' *}_{m'}(\underline{r}')\, w^{\sigma''}_{m''}(\underline{r}'). \tag{2.33}$$

As indicated by the frequency dependence of both W and U, this yields dynamic quantities. The static limit $\omega \to 0$ is normally used in the Hubbard model.

The screened operator W is a familiar object in the GW approximation [52, 53] (the W in GW is a reference to the operator W), which is closely related to the random-phase approximation (RPA) [54]. There, $\kappa = 1 - \Pi V$ is used, and the polarization function Π is approximated to be just a simple particle-hole pair ring diagram (i.e., $\Pi = -iGG$). The fully screened Coulomb interaction used for RPA calculations can be calculated from a DFT calculation, by using the polarization [55–57]

$$\begin{aligned}\Pi^{RPA}(\underline{r},\underline{r}',\omega) = &-\sum_{k\nu}^{occ.}\sum_{k'\nu'}^{unocc.} \frac{\psi_{k\nu}(\underline{r})\psi^*_{k\nu}(\underline{r}')\psi_{k'\nu'}(\underline{r}')\psi^*_{k'\nu'}(\underline{r})}{\omega + \varepsilon_{\nu'} - \varepsilon_{\nu} - i\gamma} \\ &+\sum_{k\nu}^{occ.}\sum_{k'\nu'}^{unocc.} \frac{\psi_{k\nu}(\underline{r}')\psi^*_{k\nu}(\underline{r})\psi_{k'\nu'}(\underline{r})\psi^*_{k'\nu'}(\underline{r}')}{\omega - \varepsilon_{\nu'} + \varepsilon_{\nu} + i\gamma},\end{aligned} \tag{2.34}$$

where the KS states and energies are used in the sums over occupied and unoccupied states, and the limit $\gamma \to 0^+$ has to be taken.

When calculating the screened Coulomb interaction for the orbitals of a correlated subspace $\mathcal{W}$, the full interaction should be taken into account for these correlated orbitals, and only the screening due to the uncorrelated orbitals shall be included. Therefore, one does not use the fully screened interaction for DMFT calculations. It is possible to limit the evaluation of Π^{RPA} in (2.34) to transitions between the correlated and uncorrelated subspace and within the uncorrelated subspace, but exclude transitions within the correlated subspace. That procedure is called constrained RPA (cRPA) [58, 59]. We stress once more that in that case, the screened operator W depends on the choice of correlated subspace $\mathcal{W}$.

Of course, cRPA is just one possible method to calculate the interaction from ab-initio calculations, others being, e.g., the constrained LDA (cLDA) [60] or a method based on the self-consistent GW approach [61].

While it is possible to use the static part of (2.33) as $U^{\sigma\sigma'\sigma''\sigma'''}_{mm'm''m'''}$, which for M correlated orbitals consists of M^4 entries, often one uses a parametrization of the interaction tensor by a set of some parameters. The extraction of just some useful parameters from the ab-initio

$U^{\sigma\sigma'\sigma''\sigma'''}_{mm'm''m'''}$ facilitates the reproducibility and adaptability of the scheme; the full interaction is then reconstructed only from these parameters. This practice allows us to rely on ab-initio calculations of the interaction from the literature, without having to perform them ourselves.

A very popular choice for a parametrization of the interaction is by means of Slater integrals [62],

$$F^k = \int r^2\, dr\, r'^2\, dr' \, \frac{\min(r,r')^k}{\max(r,r')^{k+1}} \mathcal{R}^2(r)\mathcal{R}^2(r'), \tag{2.35}$$

where just the radial part $\mathcal{R}$ of the wave function enters. In an atom, spherical symmetry is present (i.e., any rotation of the orbitals around the atom in real space is a symmetry operation), and so the radial and spherical part of the wave function can be separated. While that symmetry is not present in crystals, the Slater parametrization can nevertheless be used as an approximation. Given these Slater integrals, the interaction matrix in the basis of hydrogen-like wave functions with spherical harmonics $Y_\ell^{m_\ell}$ is

$$U_{mm'm''m'''} = \sum_{k=0}^{2\ell} \mathcal{A}_{k\ell}(m,m',m'',m''')F^k, \tag{2.36}$$

with the integrals of the angular parts (also called Racah-Wigner numbers)

$$\begin{aligned}\mathcal{A}_{k\ell}(m,m',m'',m''') =& (2\ell+1)^2 \begin{pmatrix} \ell & k & \ell \\ 0 & 0 & 0 \end{pmatrix}^2 \cdot \\ & \sum_{q=-k}^{k} (-1)^{m+m'+q} \begin{pmatrix} \ell & k & \ell \\ -m & q & m'' \end{pmatrix} \begin{pmatrix} \ell & k & \ell \\ -m' & -q & m''' \end{pmatrix}.\end{aligned} \tag{2.37}$$

Here, the Wigner 3-j-symbols are used. The U-tensor in (2.36) is the same for both spins, therefore no explicit spin-dependence is given. The parametrization in terms of Slater integrals is equivalent to the parametrization in terms of interaction parameters U (the Coulomb interaction strength) and J (Hund's coupling). In general, we have $U = F^0$. The relationship between J and the Slater integrals depends on the ℓ quantum number; for d-electrons ($\ell = 2$), $J = (F^2 + F^4)/14$. For F^4, usually $F^4/F^2 = 0.625$ (i.e., the atomic value) is used for d-orbitals[5].

In the t_{2g} subspace of cubic systems (as many transition metal oxides are perovskites, this is a relevant case), the Slater interaction can be parametrized differently, using so-called Kanamori

[5] TRIQS uses 0.63 instead of 0.625.

parameters U_K, U'_K and J_K. The Slater Hamiltonian can be approximated as

$$\begin{aligned} H_{int} &= \frac{1}{2} \sum_{\substack{mm'm''m''' \\ \sigma\sigma'}} U_{mm'm''m'''}\, c^\dagger_{m\sigma} c^\dagger_{m'\sigma'} c_{m'''\sigma'} c_{m''\sigma} \\ &\simeq \frac{1}{2} \sum_{mm'} \sum_{\sigma\sigma'} (U_{mm'mm'} - \delta_{\sigma\sigma'}\, U_{mm'm'm})\, n_{m\sigma} n_{m'\sigma'} \\ &\quad + \frac{1}{2} \sum_{m\neq m'} \sum_{\sigma} U_{mm'm'm}\, c^\dagger_{m\sigma} c^\dagger_{m'\bar{\sigma}} c_{m\bar{\sigma}} c_{m'\sigma} + \frac{1}{2} \sum_{m\neq m'} \sum_{\sigma} U_{mmm'm'}\, c^\dagger_{m\sigma} c^\dagger_{m\bar{\sigma}} c_{m'\sigma} c_{m'\bar{\sigma}}, \end{aligned} \tag{2.38}$$

where $\bar{\sigma}$ means the opposite spin of σ. The three terms are called the density-density, spin-flip and pair-hopping term. This expression includes all terms where there are no more than two different orbital indices involved. It turns out that in the t_{2g}-subset all the other terms are zero.

It is possible to split the density-density term into intraorbital and interorbital contributions,

$$\begin{aligned} H_{int} &\simeq \sum_m U_{mmmm}\, n_{m\uparrow} n_{m\downarrow} + \frac{1}{2} \sum_{m\neq m'} \sum_{\sigma\sigma'} (U_{mm'mm'} - U_{mm'm'm}\delta_{\sigma\sigma'})\, n_{m\sigma} n_{m'\sigma'} \\ &\quad + \frac{1}{2} \sum_{m\neq m'} \sum_{\sigma} U_{mm'm'm}\, c^\dagger_{m\sigma} c^\dagger_{m'\bar{\sigma}} c_{m\bar{\sigma}} c_{m'\sigma} + \frac{1}{2} \sum_{m\neq m'} \sum_{\sigma} U_{mmm'm'}\, c^\dagger_{m\sigma} c^\dagger_{m\bar{\sigma}} c_{m'\sigma} c_{m'\bar{\sigma}}. \end{aligned} \tag{2.39}$$

Now, a set of new parameters is introduced,

$$U_K = U_{mmmm} = F^0 + \frac{4}{49}(F^2 + F^4) = U + \frac{8}{7}J, \tag{2.40}$$

$$U'_K = U_{mm'mm'}(m \neq m') = F^0 - \frac{2}{49}F^2 - \frac{4}{441}F^4 \simeq U - \frac{328}{819}J, \tag{2.41}$$

$$J_K = U_{mm'm'm}(m \neq m') = U_{mmm'm'}(m \neq m') = \frac{3}{49}F^2 + \frac{20}{441}F^4 \simeq \frac{632}{819}J \tag{2.42}$$

(the equality of $U_{mm'm'm}$ and $U_{mmm'm'}$ for $m \neq m'$ only holds for real-valued basis wave functions, see Ref. [62]; the relations written with $\simeq$ only hold assuming $F_4/F_2 = 5/8$). Then, the *Kanamori* Hamiltonian is obtained [63],

$$\begin{aligned} H_{int} &\simeq U_K \sum_m n_{m\uparrow} n_{m\downarrow} + \frac{1}{2} \sum_{m\neq m'} \sum_{\sigma\sigma'} (U'_K - J_K\delta_{\sigma\sigma'})\, n_{m\sigma} n_{m'\sigma'} \\ &\quad + \frac{1}{2} J_K \sum_{m\neq m'} \sum_{\sigma} (c^\dagger_{m\sigma} c^\dagger_{m'\bar{\sigma}} c_{m\bar{\sigma}} c_{m'\sigma} + c^\dagger_{m\sigma} c^\dagger_{m\bar{\sigma}} c_{m'\bar{\sigma}} c_{m'\sigma}). \end{aligned} \tag{2.43}$$

As for the Slater matrix, spherical symmetry is assumed (as Slater integrals and angular momentum operators are evaluated separately and independently), $U'_K + 2J_K = U_K$ holds. In general, for cubic systems, spherical symmetry is not given, but choosing the parameters U_K, U'_K and J_K (instead of U and J) is still possible [62]; often, still $U'_K + 2J_K = U_K$ is chosen. Furthermore, when not restricting the orbitals to the t_{2g} subspace, the equality of the Kanamori parameters and the matrix elements of the Slater matrix $U_{mm'm''m'''}$ does not hold anymore, because the

elements are not the same for the individual values of m and m'. For instance, Hund's coupling J_K is not the same in the t_{2g} subsystem and the e_g subsystem. Then, as an approximation, a parametrization with U_K, U'_K and J_K is still possible; the effective Kanamori parameters can be calculated from the Slater matrix as

$$U_K = \frac{1}{M}\sum_{m}^{M} U_{mmmm}, \tag{2.44}$$

$$J_K = \frac{1}{M(M-1)}\sum_{m\neq m'}^{M} U_{mm'm'm}, \tag{2.45}$$

$$U'_K = \frac{1}{M(M-1)}\sum_{m\neq m'}^{M} U_{mm'mm'}. \tag{2.46}$$

2.3.4 Basis transformation

For all physical properties (including Green's functions), it does not matter in which basis the problem is formulated. It is possible to transform between different one-particle bases by means of a unitary basis transformation matrix T, which is equivalent to constructing a new set of creation and annihilation operators as linear combinations of the old ones.

We define the transformation of the single-particle basis, as given by the transformation of the second quantization operators, as follows[6]

$$\begin{aligned} \tilde{c}_n &= \sum_m T_{nm} c_m, & \tilde{c}^\dagger_n &= \sum_m T^*_{nm} c^\dagger_m, \\ c_m &= \sum_n T^*_{nm} \tilde{c}_n, & c^\dagger_m &= \sum_n T_{nm} \tilde{c}^\dagger_n. \end{aligned} \tag{2.47}$$

The operators with a tilde are in the new basis. We do not use explicit spin indices, but rather can the indices m and n be thought of as compound indices of orbital and spin. This allows to treat in the same framework transformations that just act in the orbital degrees of freedom as well as transformations that mix spins.

The Green's function is given by the Lehmann representation

$$G_{mm'}(z) = \sum_a \frac{\langle 0|c_m|a\rangle \langle a|c^\dagger_{m'}|0\rangle}{z-(E_a-E_0)} + \sum_b \frac{\langle 0|c^\dagger_{m'}|b\rangle \langle b|c_m|0\rangle}{z-(E_b-E_0)}, \tag{2.48}$$

where $|0\rangle$ is the ground state with N particles, the sum over a runs over the eigenstates with

[6] The convention in TRIQS/DFTTools `pytriqs.applications.dft.trans_basis` and in some articles found in the literature (e.g., Ref. [64]) uses $T^\dagger$ instead of T. In the TRIQS module `pytriqs.operators.U_matrix`, the transformation convention is such that T^* has to be used instead of T. The input transformation matrix for the `fromfile` functionality of the TRIQS/DFTTools program `dmftproj` also uses T^* instead of T, but the transformation in the TRIQS/DFTTools module `pytriqs.applications.sumk_dft` (`SumkDFT.T`) and the TRIQS/DFTTools Wien2k converter `pytriqs.applications.dft.converters.wien2k_converter` is the same as presented here.

$N+1$ particles and the sum over b runs over the eigenstates with $N-1$ particles. Here, the E_i are the many-body eigenenergies of the system.

By inserting the transformations, one obtains

$$G_{mm'}(z) = \sum_{nn'} T^*_{nm} T_{n'm'} \left(\sum_a \frac{\langle 0|\tilde{c}_n|a\rangle \langle a|\tilde{c}^\dagger_{n'}|0\rangle}{z-(E_a-E_0)} + \sum_b \frac{\langle 0|\tilde{c}^\dagger_{n'}|b\rangle \langle b|\tilde{c}_n|0\rangle}{z-(E_b-E_0)} \right), \tag{2.49}$$

where the expression in parentheses can be identified as the Green's function in the transformed basis,

$$G_{mm'}(z) = \sum_{nn'} T^*_{nm} T_{n'm'} \tilde{G}_{nn'}(z). \tag{2.50}$$

In matrix formulation,

$$G(z) = T^\dagger \tilde{G}(z) T, \tag{2.51}$$

or, vice versa,

$$\tilde{G}(z) = T G(z) T^\dagger. \tag{2.52}$$

The interaction tensor U follows the convention introduced in (2.10), which is

$$H_{int} = \sum_{mm'm''m'''} U_{mm'm''m'''}\ c^\dagger_m c^\dagger_{m'} c_{m'''} c_{m''}. \tag{2.53}$$

By inserting the transformation, one gets

$$H_{int} = \sum_{nn'n''n'''} \sum_{mm'm''m'''} T_{nm} T_{n'm'} U_{mm'm''m'''} T^*_{n'''m'''} T^*_{n''m''}\ \tilde{c}^\dagger_n \tilde{c}^\dagger_{n'} \tilde{c}_{n'''} \tilde{c}_{n''}. \tag{2.54}$$

Thus, the transformed interaction matrix is

$$\tilde{U}_{nn'n''n'''} = \sum_{mm'm''m'''} T_{nm} T_{n'm'} U_{mm'm''m'''} T^*_{n'''m'''} T^*_{n''m''}. \tag{2.55}$$

When the Kanamori Hamiltonian is used in the t_{2g} subshell, it is equivalent to the Slater Hamiltonian and, thus, transforms as such. While the Kanamori Hamiltonian is invariant under orbital transformations, whenever the transformation mixes spins (e.g., due to spin-orbit coupling, see chapter 3), this is not the case. When using the Kanamori interaction as an alternative parametrization, it is not clear *per se* in which basis to even write down the Kanamori Hamiltonian initially, although one could probably argue that the cubic harmonic basis is best suited. Because of these complications and to avoid possible inconsistencies, in this work always the Slater parametrization has been used.

2.3.5 Fully charge self-consistent DFT+DMFT

This section is based on Ref. [65].

So far, only one-shot DMFT calculations on top of a DFT calculation have been discussed. However, it is possible to self-consistently iterate DFT and DMFT. Just as in a one-shot calculation, PWF are constructed after having converged the DFT calculation, and DMFT is performed. However, instead of iterating the DMFT loop until convergence, a bigger self-consistent cycle is run. Then, having performed a DMFT step[7], an update to the charge density caused by the correlations is calculated. This is why this procedure is called fully charge self-consistent (fcsc) DFT+DMFT.

The charge density in DFT is given as

$$\varrho(\underline{r}) = \sum_{\underline{k},\nu} u^*_{\underline{k}\nu}(\underline{r}) u_{\underline{k}\nu}(\underline{r})\, f_{\underline{k}\nu} \tag{2.56}$$

(this is equivalent to (2.6), but instead of summing just over the occupied bands the occupation number $f_{\underline{k}\nu}$ of the bands is explicitly used). In the DFT+DMFT formalism with PWF, the correlated density matrix is

$$\hat{\varrho}_{\nu\nu'}(\underline{k}) = -G_{\nu\nu'}(\underline{k}, \tau = \beta) = -\frac{1}{\beta}\sum_n e^{i\omega_n\beta} G_{\nu\nu'}(\underline{k}, i\omega_n) = \frac{1}{\beta}\sum_n G_{\nu\nu'}(\underline{k}, i\omega_n), \tag{2.57}$$

where $G_{\nu\nu'}(\underline{k}, \tau = \beta)$ is the inverse Fourier-transformed[8] lattice Green's function

$$G_{\nu\nu'}(\underline{k}, i\omega_n) = \left(i\omega_n - \varepsilon_{\underline{k}} + \mu - \hat{\Sigma}^{\alpha\sigma}(\underline{k}, z) + \mathrm{DC}\right)^{-1}_{\nu\nu'}; \tag{2.58}$$

all the quantities in the parenthesis are matrices. Given the correlated density matrix, the charge density is now

$$\varrho(\underline{r}) = \sum_{\underline{k},\nu} u^*_{\underline{k}\nu}(\underline{r}) u_{\underline{k}\nu}(\underline{r})\, f_{\underline{k}\nu} + \sum_{\underline{k},\nu\nu'\in\mathcal{W}} u^*_{\underline{k}\nu}(\underline{r}) u_{\underline{k}\nu'}(\underline{r})(\hat{\varrho}_{\nu\nu'}(\underline{k}) - \delta_{\nu\nu'} f_{\underline{k}\nu}), \tag{2.59}$$

where the last sum features the change of the density due to correlations; the trace of $\hat{\varrho}_{\nu\nu'}(\underline{k}) - \delta_{\nu\nu'} f_{\underline{k}\nu}$ has to be zero. Using the updated charge density, a new KS effective potential is constructed, the corresponding KS Hamiltonian is solved, and new KS eigenstates and energies are obtained. Then, once more the construction of PWF can be performed and another DMFT iteration can be executed. This process is then iterated until convergence.

An important quantity in DFT is the total energy, which is given by the total energy functional.

[7] Depending on the situation at hand, it might be necessary and beneficial to perform a larger number of DMFT steps between DFT steps.

[8] As soon as the high-frequency expansion of the Matsubara Green's function ("tail") is (at least approximately) known, that part of the Green's function can be Fourier transformed analytically, giving an improved result. This is used in the TRIQS implementation of both the (inverse) Fourier transform and the evaluation of the density.

It is possible to calculate it including the DMFT corrections,

$$E = E_{DFT}[\varrho] + \sum_{\underline{k},\nu\in\mathcal{W}} (\hat{\varrho}_{\nu\nu}(\underline{k}) - f_{\underline{k}\nu})\varepsilon_{\underline{k}\nu} + E_{corr} - E_{dc}. \tag{2.60}$$

The first term is the total energy from DFT from (2.1), the second term is the change in band energy due to the changes in occupancy caused by the correlations, the third term E_{corr} is the correlation energy from DMFT and the fourth term E_{dc} is the double-counting energy. Depending on the point of view, one can therefore see the method as a correction to DFT or as a modified DFT functional (as, e.g., suggested by the name "DFT + Embedded DMFT Functional" used by Haule [66]).

The correlation energy E_{corr} is the expectation value of the interaction Hamiltonian H_{int}, which can either be calculated by the solver (e.g., by measuring it in a Quantum Monte Carlo solver) or approximately evaluated using the Galitskii-Migdal formula [67]

$$E_{corr} \simeq \frac{1}{2}\frac{1}{\beta}\sum_m \sum_n \Sigma^{mm}(i\omega_n) G^{mm}_{imp}(i\omega_n). \tag{2.61}$$

The double-counting energy depends on the flavor of double-counting correction used (see section 2.3.2); in the FLL it is [45]

$$E_{dc} = \frac{1}{2}UN_{imp}(N_{imp}-1) - \frac{1}{2}J\sum_\sigma N_\sigma(N_\sigma - 1). \tag{2.62}$$

The evaluation of the total energy functional allows, for example, to optimize the total energy with respect to structural parameters.

2.3.6 Implementation in TRIQS

The TRIQS package [33] provides, by means of the main TRIQS library, a way to conveniently handle and manipulate Green's function objects. There are also several TRIQS applications, based on the library, that provide the ingredients for DMFT and DFT+DMFT calculations; among them impurity solvers (see chapter 4) and the TRIQS/DFTTools [34] package.

The latter provides the interface to DFT codes and the tools necessary to carry out the DMFT in Bloch space, as discussed in section 2.3.2.

Interface to DFT codes

There is a program called `dmftproj` shipped with TRIQS/DFTTools that takes as input the results from a Wien2k [24] calculation and produces, among other things, orthogonalized PWF. After the Wien2k calculation has converged, the `lapw2` program has to be run with the `-almd`

switch, which produces intermediate files describing the KS wave functions. Then `dmftproj` is used to orthonormalize the projectors[9] and to write out another set of intermediate files. These files can the be read in by a python module called `wien2k_converter`, which produces an HDF5 file containing the information that is relevant for the DMFT calculation.

The VASP program package [25–29] offers the possibility to write out a file called `LOCPROJ` that contains the projection of the KS wavefunctions onto localized orbitals (however, these are not orthonormalized). In TRIQS/DFTTools, there is a program called `plovasp` that performs the orthonormalization of these orbitals to get PWF [12]. In analogy to the `wien2k_converter` module, there is also a `vasp_converter` module that creates the necessary entries in the HDF5 file. It is worth noting that the structure of the HDF5 file is the same regardless of which interface was used.

Both the Wien2k and VASP interface offer the possibility to perform fcsc DFT+DMFT calculations, where TRIQS/DFTTools implements a way to write a file (called `case.qdmft` in the case of Wien2k and `GAMMA` for VASP) containing the charge update that can then be read by the DFT code.

In addition to these two interfaces for PWF, there is an interface to Wannier90. As mentioned above, many DFT codes can be used with the Wannier90 [37] package to construct MLWF from a DFT calculation. In TRIQS/DFTTools, there is a converter that can create an HDF file from the output of the Wannier90 program. However, fcsc calculations are not possible within that framework.

Similarly, it is possible to use a $\underline{k}$-dependent Hamiltonian as input to the `hk_converter` module to create an HDF file. The $\epsilon(\underline{k})$ can, for instance, be taken from a Wannier90 calculation. In that case, however, no up and downfolding on the level of Green's functions is performed, but the $\epsilon(\underline{k})$ has the characteristics of an effective low-energy model, which can be seen as a downfolded Hamiltonian. Of course, no fcsc calculations can be done in that framework, either.

Performing the DMFT calculation

After the construction of the correlated orbitals, the TRIQS/DFTTools package provides a set of python modules that allow the concise implementation of the DFT+DMFT loop (see section 2.3.2). The most important one is called `SumkDFT`, which can be given a self-energy Σ (method `put_Sigma`) and produce a local Green's function (method `extract_G_loc`). Furthermore, the double-counting correction (method `calc_dc`) and the chemical potential (method `calc_mu`) can be easily calculated. Most importantly, this is totally independent of the way chosen to construct the correlated orbitals. One feature of `SumkDFT` is to calculate the minimal block structure of the Green's functions, i.e., to find a block-diagonal form where there are no non-zero

[9] The author of this thesis developed a python program that can perform the orthonormalization of the projectors in a more flexible manner, e.g., choosing k-dependent energy windows, and the construction of molecular orbital projectors as in Ref. [68].

off-diagonal elements between the blocks. An extension (the `BlockStructure` class) to the features already implemented for block structures was developed by the author of this thesis.

2.4 TRIQS Interface to VASP

The author of this thesis is coauthor of a paper in preparation [12], that presents two approaches to introduce correlations on top of VASP calculations, one being a DFT+DMFT(HF) scheme related to the so-called DFT+U method and the other one being the PWF interface to TRIQS. Here, the latter will be discussed.

2.4.1 Projectors in VASP

This section is based on Refs. [12, 29, 69, 70].

While Wien2k uses the LAPW+LO basis, VASP has a plane-wave basis in the projector-augmented wave (PAW) formalism [29, 69]. There, the all-electron KS wave function $|\psi_{\underline{k},\nu}\rangle$ can be reconstructed from a so-called pseudo wave function $|\tilde{\psi}_{\underline{k},\nu}\rangle$, which is the wave function solved in the pseudopotential approach (where the potential stemming from the nucleus is replaced by an effective potential that the valence electrons feel). These two wave functions only differ in a so-called augmentation region around the nuclei, but coincide in the interstitial region. In order to perform the mapping from $|\tilde{\psi}_{\underline{k},\nu}\rangle$ to $|\psi_{\underline{k},\nu}\rangle$, partial waves are introduced; all-electron partial waves $|\phi_i\rangle$ (e.g., the solution of the linearized radial Schrödinger equation at certain reference energies for the atom) and pseudo partial waves $|\tilde{\phi}_i\rangle$ (e.g., solutions of the Schrödinger equation for the atom with a potential derived from the pseudopotential). Outside the augmentation spheres, $|\phi_i\rangle$ and $|\tilde{\phi}_i\rangle$ coincide. Furthermore, projectors $|\tilde{p}_i\rangle$ are defined that fulfill $\langle\tilde{p}_j|\tilde{\phi}_j\rangle = \delta_{ij}$. Then,

$$|\psi_{\underline{k},\nu}\rangle = |\tilde{\psi}_{\underline{k},\nu}\rangle + \sum_i (|\phi_i\rangle - |\tilde{\phi}_i\rangle)\,\langle\tilde{p}_i|\tilde{\psi}_{\underline{k},\nu}\rangle\,. \tag{2.63}$$

The partial waves and projectors $|\tilde{p}_i\rangle$ actually have indices $|\tilde{p}_{\ell m_\ell \eta}\rangle$, with the usual orbital momentum quantum numbers ℓ and m_ℓ and a PAW channel η (corresponding to different linearization energies).

While it is possible to choose hydrogen-like test functions $|\chi_m^{\alpha\sigma}\rangle$ for the PWF, the projectors allow a better way to construct the test functions (i.e., they have a higher overlap with the KS wave functions). This method is activated by using `LORBIT=14` in the VASP input file. The projectors already have ℓ and m_ℓ indices; the only problem is how to choose which PAW channel η (or which linear combination of the channels) to use. First, the projectors $|\tilde{p}_{\ell m_\ell \eta}\rangle$ and the all-electron partial waves $|\phi_{\ell m_\ell \eta}\rangle$ are transformed to the eigenbasis of the overlap matrix $Q^{\ell m_\ell}$ of the all-electron partial waves,

$$Q^{\ell m_\ell}_{\eta\eta'} = \langle\phi_{\ell m_\ell \eta}|\phi_{\ell m_\ell \eta'}\rangle\,. \tag{2.64}$$

We denote the quantities in the eigenbasis as $|\hat{\tilde{p}}_{\ell m_\ell \hat{\eta}}\rangle$ and $|\hat{\phi}_{\ell m_\ell \hat{\eta}}\rangle$. Then, in that basis, we calculate the density matrix $\hat{\varrho}^{\ell m_\ell}$ in a user-defined energy window as

$$\hat{\varrho}^{\ell m_\ell}_{\hat{\eta}\hat{\eta}'} = \sum_{\underline{k},\nu}{}' f_\nu(\underline{k}) \, \langle \hat{\tilde{p}}_{\ell m_\ell \hat{\eta}} | \psi_{\underline{k},\nu} \rangle \, \langle \psi_{\underline{k},\nu} | \hat{\tilde{p}}_{\ell m_\ell \hat{\eta}'} \rangle \,, \tag{2.65}$$

where $f_\nu(\underline{k})$ is the filling of the Bloch band and the summation is carried out over states within the user-defined energy window only. Finally, we diagonalize the density matrix $\hat{\varrho}^{\ell m_\ell}$ and take the eigenvector $\underline{v}^{\ell m_\ell}$ with the largest eigenvalue (i.e., the largest overlap of the projector test function with the KS wave functions). Then, the orbitals on which we project are

$$|\chi_{\ell m_\ell}\rangle = \sum_{\hat{\eta}} v^{\ell m_\ell}_{\hat{\eta}} \, |\hat{\phi}_{\ell m_\ell \hat{\eta}}\rangle \tag{2.66}$$

and the corresponding PAW projectors are

$$\langle \tilde{\pi}_{\ell m_\ell}| = \sum_{\hat{\eta}} v^{\ell m_\ell \, *}_{\hat{\eta}} \, \langle \hat{\tilde{p}}_{\ell m_\ell \hat{\eta}}| \,. \tag{2.67}$$

The unorthonormalized projectors are

$$\mathcal{P}_{\ell m_\ell \nu}(\underline{k}) = \langle \tilde{\pi}_{\ell m_\ell} | \psi_{\underline{k},\nu} \rangle \,. \tag{2.68}$$

Subsequently, these projectors are orthonormalized just as in Wien2k and the relevant results of the DFT calculation are converted to the HDF5 format, which allows the use of the same DMFT scripts as for the Wien2k code.

2.4.2 Fully charge self-consistent calculation of layered $SrVO_3$

The following is based on the work the author of this thesis contributed to Ref. [12].

We benchmark the DFT+DMFT implementation of TRIQS/DFTTools with VASP on the example of a monolayer of $SrVO_3$. In this system, the DMFT corrections to the DFT result leads to a non-negligible rearrangement of charges, therefore making the use of a fully charge self-consistent DFT+DMFT scheme imperative. This compound has already been studied using a similar methodology, but based on the Wien2k DFT code; this allows us to compare our results to the published study [71]. In agreement with that study, we use an in-plane lattice constant of 3.92 Å, simulating the epitaxial growth of $SrVO_3$ on $SrTiO_3$ (see the schematic of the unit cell in figure 2.4). However, the substrate is not directly taken into account, but rather a free-standing monolayer of $SrVO_3$ is considered; a vacuum layer of about 16 Å is used to isolate the individual layers in a periodic VASP calculation. Based on geometry relaxations on the DFT level, in the out-of-plane direction, the V-O distance is reduced from 1.96 Å to 1.93 Å and the Sr-Sr distance from 3.92 Å to 3.52 Å. The Brillouin zone was sampled using a $15 \times 15 \times 1$ Γ-centered Monkhorst-Pack k-grid.

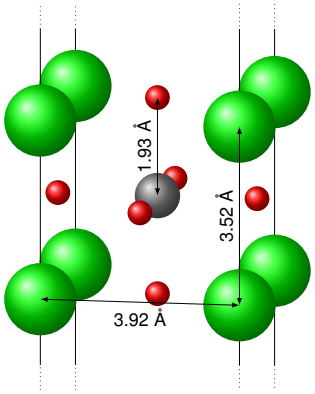

Figure 2.4: Unit cell of the monolayer of $SrVO_3$. The Sr atoms are green, the V atom gray and the O atoms red. The lattice constant in the z-direction is 20 Å, i.e., there is about 16 Å of vacuum between the periodic replica of the layers, effectively giving an isolated monolayer.

The energy cutoff of the plane wave basis set was 400 eV, in accordance with the default value for the PAW pseudopotentials used. The projectors onto the V d-states were calculated as described in section 2.4.1. In the t_{2g} subspace, a Hubbard-Kanamori interaction with $U_K = 5.5$ eV and $J_K = 0.75$ eV (in agreement with Ref. [71]) is added; the double-counting is estimated in the Held-FLL scheme [47]. The impurity problem was solved using the TRIQS/CTHYB Quantum Monte Carlo [72] (see chapter 4) solver at inverse temperature $\beta = 40$ eV^{-1}.

In DFT, the compound is metallic; the strong interaction drives it through a Mott transition, so that it becomes insulating (see figure 2.5). In the one-shot DFT+DMFT calculation, there is a nearly complete polarization of the orbitals (see fillings in table 2.1), which is equal in VASP and Wien2k. When using the charge feedback in the fully charge self-consistent framework, the empty orbitals get partly repopulated. This effect is stronger in VASP, but the agreement of the two DFT codes is within the error bars of the method. This repopulation can also be seen in the spectral function (figure 2.5), which is obtained using analytic continuation of the local lattice Green's function. In the fully charge self-consistent calculation, a lower Hubbard band with non-negligible spectral weight can be found also for the degenerate d_{xz} and d_{yz} orbitals. The same Mott gap is found starting from both DFT codes, and the peak positions are basically identical. The difference in peak height is compatible with the difference of filling between the two methodologies.

Calculating the total energy depending on a structural parameter allows to determine the lowest-energy structure in DFT+DMFT. Here, as a proof of principle, we calculate the total energy of the compound when moving the Sr-O planes in z direction by Δz with respect to the DFT-optimized structure. Positive Δz means that the upper Sr-O plane gets shifted upwards and the lower plane gets shifted downwards, thus increasing the thickness of the slab in z direction. This changes the splitting between the d_{xy}, which is close to half-filling, and the degenerate d_{xz} and d_{yz} orbitals, which are nearly empty. For more negative Δz, the d_{xy} orbital gets closer to half-filling (see

Table 2.1: Filling of the correlated orbitals in DFT+DMFT for one-shot and fully charge self-consistent calculations based on VASP and Wien2k.

	one-shot		fcsc	
	d_{xy}	d_{xz}, d_{yz}	d_{xy}	d_{xz}, d_{yz}
VASP	0.48	0.01	0.34	0.08
Wien2k	0.48	0.01	0.38	0.06

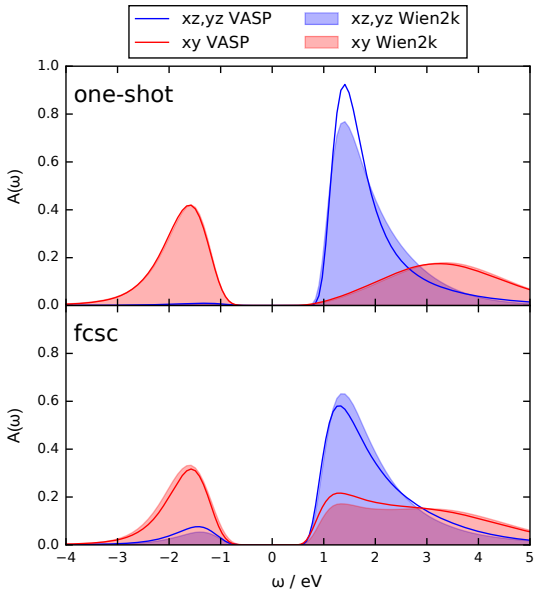

Figure 2.5: Spectral function of the single layer of $SrVO_3$ in DFT+DMFT in a one-shot (top) and a fully charge self-consistent (bottom) calculation. The calculations have been performed using TRIQS/DFTTools, once with Wien2k and once with VASP as DFT code. The resulting imaginary-time Green's function was analytically continued using the Maximum Entropy Method (see chapter 5).

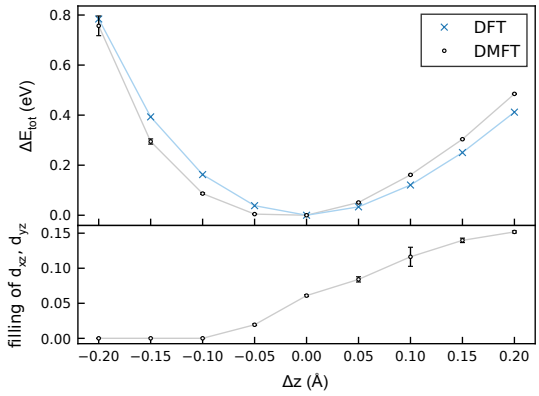

Figure 2.6: Top: Total energy change of the single layer of $SrVO_3$ when moving the upper and lower Sr-O-plane symmetrically by Δz in DFT and in fully charge self-consistent DFT+DMFT. The reference energy (i.e., the energy for $\Delta z = 0$, which is set to 0 in this plot) is different for DFT and DFT+DMFT. Bottom: Filling of the degenerate d_{xz} and d_{yz} orbitals depending on Δz. The total filling of the impurity is 1 electron. The lines in both plots are guides to the eye. The values and error bars of the DFT+DMFT calculations in both plots were obtained by calculating the quantity for the four last iterations and then getting the mean and the standard deviation. For many data points, the error is so small that it is invisible on the scale of the plot. The total energy in DFT was converged to 10^{-6} eV.

figure 2.6, bottom) and the bandwidth decreases, which increases the correlations and thus the size of the Mott gap (not shown here). The total energy curve calculated with DFT+DMFT is shifted towards lower Δz (figure 2.6, top), indicating that the structure with the lowest energy has a lower slab width than obtained by DFT. For the purpose of this benchmark, we refrain from moving the Sr and O atoms individually to further refine the crystal structure.

3 Spin-orbit coupling

For many compounds, the spin-orbit coupling (SOC) only plays a minor role for the valence electrons and can be neglected. This is, however, not the case for materials where these valence bands stem from sufficiently heavy atoms. In that case, it is absolutely necessary to take that relativistic effect into account.

This chapter reviews the SOC, from general considerations to implications for DMFT calculations.

3.1 Relativistic quantum mechanics and spin-orbit coupling

This section is based on Refs. [73] and [74].

In non-relativistic quantum mechanics, the central equation is the Schrödinger equation. The results of Einstein's special theory of relativity, in particular the relation between energy and momentum

$$E^2/c^2 - p^2 = m^2c^2 \tag{3.1}$$

(with the speed of light c [in atomic units, $c = 1/\alpha_F \approx 137$ with the fine structure constant α_F], the energy E, the momentum p, and the mass m) can be incorporated into that framework by means of the Dirac equation

$$i\frac{\partial\psi}{\partial t} = \frac{c}{i}\left(\sum_i \hat{\alpha}_i \frac{\partial\psi}{\partial x_i}\right) + \hat{\beta}mc^2\psi = H\psi. \tag{3.2}$$

There, the wave function ψ is a four-component object and the coefficients $\hat{\alpha}_i$ and $\hat{\beta}$ are (at least) 4×4 matrices. In the Bjorken-Drell convention, one uses

$$\hat{\alpha}_i = \begin{pmatrix} 0 & \sigma_i \\ \sigma_i & 0 \end{pmatrix} \qquad \text{and} \qquad \hat{\beta} = \begin{pmatrix} \mathbb{1} & 0 \\ 0 & -\mathbb{1} \end{pmatrix}. \tag{3.3}$$

We use the Pauli matrices

$$\sigma_x = \begin{pmatrix} 0 & 1 \\ 1 & 0 \end{pmatrix}, \qquad \sigma_y = \begin{pmatrix} 0 & -i \\ i & 0 \end{pmatrix}, \qquad \sigma_z = \begin{pmatrix} 1 & 0 \\ 0 & -1 \end{pmatrix}. \tag{3.4}$$

We want to focus on a hydrogen-like atom, for which the Dirac equation reads

$$H\psi = (c\sum_i \hat{\alpha}_i p_i + \hat{\beta}mc^2 + v)\psi = E\psi. \tag{3.5}$$

Note that the electron mass is $m = 1$ in atomic units. The central potential is given by

$$v = -\frac{Z_N}{r}\alpha_F, \tag{3.6}$$

where Z_N is the atomic number. The four-component wave function ψ can be written using two two-component objects $\psi = (\phi, \chi)^T$. Then, (3.5) becomes

$$\begin{pmatrix} (mc^2 + v)\mathbb{1} & c\underline{\sigma}\,\underline{p} \\ c\underline{\sigma}\,\underline{p} & (-mc^2 + v)\mathbb{1} \end{pmatrix} \begin{pmatrix} \phi \\ \chi \end{pmatrix} = E \begin{pmatrix} \phi \\ \chi \end{pmatrix}. \tag{3.7}$$

This leads to the coupled equations

$$c\underline{\sigma}\,\underline{p}\chi = (\tilde{E} - v)\phi \tag{3.8}$$

$$c\underline{\sigma}\,\underline{p}\phi = (\tilde{E} + 2mc^2 - v)\chi. \tag{3.9}$$

We introduced $\tilde{E} = E - mc^2$, the energy on top of the rest energy mc^2, which is the energy of the Schrödinger equation. It is possible to rewrite (3.9) as

$$\begin{aligned} \chi &= \frac{1}{2mc}\left(1 + \frac{\tilde{E} - v}{2mc^2}\right)^{-1} \underline{\sigma}\,\underline{p}\phi \\ &=: K\underline{\sigma}\,\underline{p}\phi. \end{aligned} \tag{3.10}$$

By substituting (3.10) into (3.8), one obtains[1]

$$c\underline{\sigma}\,\underline{p}K\underline{\sigma}\,\underline{p}\phi = (\tilde{E} - v)\phi \tag{3.11}$$

$$(c\underline{p}K\underline{p} + ic\underline{\sigma}\underline{p}K \times \underline{p} + v)\phi = \tilde{E}\phi \tag{3.12}$$

The first term is independent of spin, it is the scalar-relativistic kinetic energy. The second term is the spin-orbit coupling.

When introducing approximations to facilitate the solution of the Dirac equation, we can treat the scalar-relativistic kinetic energy part and the spin-orbit part differently, i.e.,

$$(c\underline{p}K_1\underline{p} + ic\underline{\sigma}\underline{p}K_2 \times \underline{p} + v)\phi = \tilde{E}\phi. \tag{3.13}$$

The crudest approximation for K_2 is zeroth order in $(\tilde{E} - v)/2mc^2$ (which is small in the

[1] To go from the first to the second line, the vector identity $(\underline{\sigma}\,\underline{a})(\underline{\sigma}\,\underline{b}) = \underline{a}\,\underline{b} + i\underline{\sigma}\,\underline{a} \times \underline{b}$ is used.

non-relativistic limit),

$$K_2 = \frac{1}{2mc}\left(1 + \frac{\tilde{E} - v}{2mc^2}\right)^{-1} \approx \frac{1}{2mc}. \tag{3.14}$$

Using that, we obtain the scalar-relativistic Schrödinger equation, where the spin-orbit term is zero,

$$(c\underline{p}K_1\underline{p} + v)\phi = \tilde{E}\phi. \tag{3.15}$$

Inserting this into (3.10), one sees that χ is way smaller than ϕ; therefore, we call ϕ the "large" and χ the "small" component of ψ. Often, the small component is neglected.

Considering one more term in the expansion,

$$K_2 \approx \frac{1}{2mc}\left(1 - \frac{\tilde{E} - v}{2mc^2}\right), \tag{3.16}$$

one obtains the spin-orbit coupled Schrödinger equation

$$(c\underline{p}K_1\underline{p} + \frac{i}{4m^2c^2}\underline{\sigma p}v \times \underline{p} + v)\phi = \tilde{E}\phi. \tag{3.17}$$

Using the same approximation for K_1 and performing some algebra, one obtains

$$\left(\frac{p^2}{2m} + v - \frac{p^4}{8m^3c^2} - \frac{1}{4m^2c^2}\frac{dv}{dr}\frac{\partial}{\partial \underline{r}} + \frac{1}{2m^2c^2}\frac{1}{r}\frac{dv}{dr}\underline{L}\,\underline{S}\right)\phi = \tilde{E}\phi. \tag{3.18}$$

We have thus broken down the Dirac equation to a Schrödinger equation by perturbing around the non-relativistic limit. The first two terms are the familiar terms of the Schrödinger equation. The third term is the mass term, which takes into account the relativistic increase of the mass (in first order). The fourth term is the Darwin term, which only affects s-orbitals. The final term is the spin-orbit coupling in its familiar form.

The prefactor of the spin-orbit term is

$$\lambda = \frac{1}{2m^2c^2}\frac{1}{r}\frac{dv}{dr} = \frac{Z_N\alpha_F}{2m^2c^2}\frac{1}{r^3}, \tag{3.19}$$

where the derivative was evaluated with the central hydrogen-like potential from (3.6),

$$\frac{dv}{dr} = \frac{Z_N}{r^2}\alpha_F. \tag{3.20}$$

The energy expectation value of the $1/r^3$ term using hydrogen wave functions is

$$\left\langle \frac{1}{r^3} \right\rangle = \frac{Z_N^3}{n^3}\frac{1}{\ell(\ell + \frac{1}{2})(\ell + 1)}, \tag{3.21}$$

(n is the principal quantum number) and thus the energy correction stemming from the spin-orbit coupling term is $\sim Z_N^4/n^3$.

3.2 Implementation of the spin-orbit coupling in Wien2k

The spin-orbit term is predominantly a *local* term, i.e., it affects mainly the local non-interacting Hamiltonian of the problem. In DFT+DMFT, there are, in general, two different ways of treating the SOC, namely by including it in the DFT calculation (which is typically a functionality provided by the DFT code) and then using bands $\varepsilon_{\underline{k},\nu}$ and projectors P including the effects of the SOC, or by adding the $\underline{L} \cdot \underline{S}$ term to the local Hamiltonian. In the latter case, the prefactor has to be estimated, e.g., by fitting the band structure to a DFT calculation including SOC. In this work, we exclusively use the former case.

By default, all Wien2k calculations consider relativistic effects for the valence electrons in the scalar-relativistic approximation (i.e., without SOC). This means that m_ℓ and m_s are good quantum numbers. On top of that, the SOC can be included in a so-called *second variational treatment* [75]. There, the total Hamiltonian including the spin-orbit term, which in this case only affects the large component of the wave function, is evaluated in the basis of the KS eigenfunctions of the scalar-relativistic Hamiltonian and subsequently diagonalized. This reduces the effort because the number of KS eigenfunctions is typically much lower than the number of basis functions used for the initial calculation. It is possible to perform this correction self-consistently or not; we always perform self-consistent SOC calculations on top of converged "normal" calculations.

In the presence of a crystal field, the rotational symmetry of an atom is broken. Therefore, the spin quantization axis (for the definition of up and down spin) is not arbitrary anymore, and choosing a different quantization axis changes the result (when, e.g., choosing as quantization axis the z-axis, the orientation of the spin vector in the xy-plane cannot be described). In a spin-polarized DFT calculation, the presence of SOC lowers the symmetry; Wien2k offers a program to analyze the symmetry in that case and change the space group accordingly. The fact that the spin-orbit operator features complex entries leads to complex-valued eigenfunctions, which means that the complex version of the program calculating the KS density has to be employed.

3.3 Natural bases for the spin-orbit coupling

This section is partly based on the discussion of the SOC bases in Ref. [76].

In non-interacting atoms, the electrons can be labeled by the principal quantum number n, the orbital angular momentum quantum number ℓ, the orbital magnetic quantum number m_ℓ, the spin quantum number s (which is 1/2 for electrons), and the spin magnetic quantum number m_s. As soon as the angular and spin angular momentum of an electron are coupled by means of the SOC, neither m_ℓ nor m_s are good quantum numbers anymore. Nevertheless, the quantum numbers of the total angular momentum, j and m_j, are still good.

3.3.1 Angular momentum operators and spin-orbit coupling

First, let us introduce the orbital angular momentum operator

$$\underline{L} = \begin{pmatrix} L_x \\ L_y \\ L_z \end{pmatrix}. \tag{3.22}$$

Using the quantum-mechanical states $|\ell, m_\ell\rangle$, where $\langle\theta, \varphi|\ell, m_\ell\rangle = Y_\ell^{m_\ell}(\theta, \varphi)$ (with the spherical harmonics $Y_\ell^{m_\ell}$), the eigenvalue equations for these operators are

$$L^2 |\ell, m_\ell\rangle = \ell(\ell+1) |\ell, m_\ell\rangle , \tag{3.23}$$
$$L_z |\ell, m_\ell\rangle = m_\ell |\ell, m_\ell\rangle . \tag{3.24}$$

The z-axis is not special in any way; we just use it as quantization axis.

The spin angular momentum operator is

$$\underline{S} = \begin{pmatrix} S_x \\ S_y \\ S_z \end{pmatrix}. \tag{3.25}$$

In its eigenbasis, designated by the states $|s, m_s\rangle$, we get the relations

$$S^2 |s, m_s\rangle = s(s+1) |s, m_s\rangle , \tag{3.26}$$
$$S_z |s, m_s\rangle = m_s |s, m_s\rangle . \tag{3.27}$$

Furthermore, for spin-$\frac{1}{2}$ particles, these operators are related to the Pauli matrices σ_i by

$$S_i = \frac{1}{2}\sigma_i. \tag{3.28}$$

The total angular momentum operator is

$$\underline{J} = \underline{L} + \underline{S}. \tag{3.29}$$

In analogy to the other operators, we get

$$J^2 |j, m_j\rangle = j(j+1) |j, m_j\rangle , \tag{3.30}$$
$$J_z |j, m_j\rangle = m_j |j, m_j\rangle . \tag{3.31}$$

The SOC term, $\underline{L} \cdot \underline{S} = L_x S_x + L_y S_y + L_z S_z$, does

- commute with L^2: $[\underline{L}\,\underline{S}, L^2] = \sum_{ab}(L_a L_b L_b - L_b L_b L_a) S_a = \sum_{ab}(L_a L_b L_b - L_a L_b L_b +$

$[L_a, L_b]L_b + L_b[L_a, L_b])S_a = i\sum_{abc}\varepsilon_{abc}(L_cL_b + L_bL_c)S_a$. In the double-sum over b and c, the term with the Levi-Civita symbol ε_{abc} and the term with ε_{acb} both occur, where the Levi-Civita tensor gives an opposite sign; thus $[\underline{L}\,\underline{S}, L^2] = 0$. Therefore, ℓ is a good quantum number even with SOC.

- commute with S^2. This can be seen analogously to the L^2 case. Therefore, s is a good quantum number even with SOC.
- not commute with L_z: $[\underline{L}\,\underline{S}, L_z] = \sum_a [L_a, L_z]S_a = -iL_yS_x + iL_xS_y \neq 0$. Therefore, m_ℓ is not a good quantum number with SOC.
- not commute with S_z: This can be seen analogously to the L_z case. Therefore, m_s is not a good quantum number with SOC.
- commute with J^2: $[\underline{L}\,\underline{S}, J^2] = [\underline{L}\,\underline{S}, L^2 + 2\underline{L}\,\underline{S} + S^2] = [\underline{L}\,\underline{S}, L^2] + 2[\underline{L}\,\underline{S}, \underline{L}\,\underline{S}] + [\underline{L}\,\underline{S}, S^2] = 0$. Therefore, j is a good quantum number even with SOC.
- commute with J_z: $[\underline{L}\,\underline{S}, L_z] = \sum_a [L_aS_a, J_z] = \sum_a [L_aS_a, L_z + S_z] = \sum_a [L_aS_a, L_z] + [L_aS_a, S_z] = -iL_yS_x + iL_xS_y - iL_xS_y + iL_yS_x = 0$. Therefore, m_j is a good quantum number even with SOC.

3.3.2 Atomic j-basis of the d-shell

In the following, we consider the d-shell of an atom. For an isolated atom without relativistic corrections, the non-interacting eigenenergies are only dependent on the principal quantum number, i.e., ten-fold degenerate for a d-shell. After introducing the SOC, when simultaneously diagonalizing $\underline{L} \cdot \underline{S}$, J^2 and J_z, one obtains the eigenstates in the atomic j-basis

$$
\begin{aligned}
\left|j=\frac{3}{2}, m_j=-\frac{3}{2}\right\rangle &= -\frac{2}{\sqrt{5}}\left|m_\ell=-2, m_s=\frac{1}{2}\right\rangle + \frac{1}{\sqrt{5}}\left|m_\ell=-1, m_s=-\frac{1}{2}\right\rangle \\
\left|j=\frac{3}{2}, m_j=-\frac{1}{2}\right\rangle &= \sqrt{\frac{3}{5}}\left|m_\ell=-1, m_s=\frac{1}{2}\right\rangle - \sqrt{\frac{2}{5}}\left|m_\ell=0, m_s=-\frac{1}{2}\right\rangle \\
\left|j=\frac{3}{2}, m_j=\frac{1}{2}\right\rangle &= \sqrt{\frac{2}{5}}\left|m_\ell=0, m_s=\frac{1}{2}\right\rangle - \sqrt{\frac{3}{5}}\left|m_\ell=1, m_s=-\frac{1}{2}\right\rangle \\
\left|j=\frac{3}{2}, m_j=\frac{3}{2}\right\rangle &= -\frac{1}{\sqrt{5}}\left|m_\ell=1, m_s=\frac{1}{2}\right\rangle + \frac{2}{\sqrt{5}}\left|m_\ell=2, m_s=-\frac{1}{2}\right\rangle \\
\left|j=\frac{5}{2}, m_j=-\frac{5}{2}\right\rangle &= \left|m_\ell=-2, m_s=-\frac{1}{2}\right\rangle \\
\left|j=\frac{5}{2}, m_j=-\frac{3}{2}\right\rangle &= \frac{1}{\sqrt{5}}\left|m_\ell=-2, m_s=\frac{1}{2}\right\rangle + \frac{2}{\sqrt{5}}\left|m_\ell=-1, m_s=-\frac{1}{2}\right\rangle \\
\left|j=\frac{5}{2}, m_j=-\frac{1}{2}\right\rangle &= -\sqrt{\frac{2}{5}}\left|m_\ell=-1, m_s=\frac{1}{2}\right\rangle - \sqrt{\frac{3}{5}}\left|m_\ell=0, m_s=-\frac{1}{2}\right\rangle \\
\left|j=\frac{5}{2}, m_j=\frac{1}{2}\right\rangle &= -\sqrt{\frac{3}{5}}\left|m_\ell=0, m_s=\frac{1}{2}\right\rangle - \sqrt{\frac{2}{5}}\left|m_\ell=1, m_s=-\frac{1}{2}\right\rangle
\end{aligned}
\tag{3.32}
$$

$$\left|j=\frac{5}{2},m_j=\quad\frac{3}{2}\right\rangle=\quad\frac{2}{\sqrt{5}}\left|m_\ell=\quad1,m_s=\frac{1}{2}\right\rangle+\frac{1}{\sqrt{5}}\left|m_\ell=\quad2,m_s=-\frac{1}{2}\right\rangle$$
$$\left|j=\frac{5}{2},m_j=\quad\frac{5}{2}\right\rangle=\qquad\left|m_\ell=\quad2,m_s=\frac{1}{2}\right\rangle.$$

All these states have $\ell=2$, $s=1/2$. For a Hamiltonian that consists solely of the $\underline{L}\cdot\underline{S}$ term with a constant prefactor, the eigenenergies of the $j=3/2$ states are (four-fold) degenerate and the eigenenergies of the $j=5/2$ states are (six-fold) degenerate.

When the atom is put into a crystal, the rotational symmetry is broken. Apart from the hopping between the atom and neighboring atoms, this also affects the local, on-site part of the Hamiltonian describing the atom. This effect is best described in the so-called cubic harmonic basis,

$$\begin{aligned}
|d_{z^2}\rangle &= |\ell=2,m_\ell=0\rangle\,,\\
|d_{x^2-y^2}\rangle &= \frac{1}{\sqrt{2}}\left(|\ell=2,m_\ell=-2\rangle+|\ell=2,m_\ell=2\rangle\right),\\
|d_{xy}\rangle &= \frac{1}{\sqrt{2}}\left(-|\ell=2,m_\ell=-2\rangle+|\ell=2,m_\ell=2\rangle\right),\\
|d_{xz}\rangle &= \frac{1}{\sqrt{2}}\left(|\ell=2,m_\ell=-1\rangle-|\ell=2,m_\ell=1\rangle\right),\\
|d_{yz}\rangle &= \frac{1}{\sqrt{2}}\left(|\ell=2,m_\ell=-1\rangle+|\ell=2,m_\ell=1\rangle\right).
\end{aligned}\tag{3.33}$$

Note that this is the definition that is used in Wien2k, where the transformation matrix T between spherical and cubic harmonics is real, but the d_{xy} and d_{yz} wavefunctions are purely imaginary (the others are real). Often, a different convention is used, where all cubic harmonics have real wavefunctions.

For an octahedral field, as found in cubic crystals, without SOC, the d-shell splits into two subgroups (irreducible representations), the e_g subshell (d_{z^2} and $d_{x^2-y^2}$) and the t_{2g} subshell (d_{xy}, d_{xz}, and d_{yz}). In the following, even when t_{2g} and e_g are not irreducible representations, we will call the d_{z^2} and $d_{x^2-y^2}$ states the "e_g states" and the d_{xy}, d_{xz}, and d_{yz} states the "t_{2g} states". For perfect octahedral symmetry, the e_g orbitals are degenerate, as are the t_{2g} orbitals. They are split by an energy called the crystal-field splitting $\mathcal{C}$; in that case, the crystal-field operator is diagonal in the cubic harmonic basis.

In that cubic basis, the $\underline{L}\cdot\underline{S}$ term is a block-diagonal matrix, where the first block consists of the orbitals $\{d^\uparrow_{z^2},d^\uparrow_{x^2-y^2},d^\uparrow_{xy},d^\downarrow_{xz},d^\downarrow_{yz}\}$ and the second block of the same orbitals, but with swapped

spin. The first block reads

$$(\underline{L}\cdot\underline{S})_{\text{Block 1}} = \begin{array}{c} \begin{array}{ccccc} |d^{\uparrow}_{z^2}\rangle & |d^{\uparrow}_{x^2-y^2}\rangle & |d^{\uparrow}_{xy}\rangle & |d^{\downarrow}_{xz}\rangle & |d^{\downarrow}_{yz}\rangle \end{array} \\ \begin{pmatrix} 0 & 0 & 0 & \frac{\sqrt{3}}{2} & \frac{\sqrt{3}}{2}i \\ 0 & 0 & -i & \frac{1}{2} & -\frac{1}{2}i \\ 0 & i & 0 & -\frac{1}{2}i & -\frac{1}{2} \\ \frac{\sqrt{3}}{2} & \frac{1}{2} & \frac{1}{2}i & 0 & -\frac{1}{2}i \\ -\frac{\sqrt{3}}{2}i & \frac{1}{2}i & -\frac{1}{2} & \frac{1}{2}i & 0 \end{pmatrix} \end{array}. \tag{3.34}$$

The second block is the complex conjugate of the first block. Interestingly, when just looking at the d_{z^2} and $d_{x^2-y^2}$ states, the spin-orbit coupling seems to be zero there (apart, of course, from the off-diagonal elements with the other states). This is why it is often noted that the SOC is fully quenched in the e_g subshell.

Often, DFT+DMFT calculations are restricted (for the DMFT part) to the t_{2g} subshell, when the e_g states are far from the Fermi level and there is no hybridization between t_{2g} and e_g. It is possible to describe the t_{2g} shell with spin-orbit coupling using the *t-p-equivalence*, which states that the orbital angular momentum operator $\underline{L}$ of the t_{2g} shell looks like the $\underline{L}$ operator of a p-shell, but with opposite sign,

$$L_x = \left(\begin{array}{cc|ccc} 0 & 0 & 0 & -\sqrt{3} & 0 \\ 0 & 0 & 0 & -1 & 0 \\ \hline 0 & 0 & 0 & 0 & 1 \\ -\sqrt{3} & -1 & 0 & 0 & 0 \\ 0 & 0 & 1 & 0 & 0 \end{array}\right) \qquad L_y = \left(\begin{array}{cc|ccc} 0 & 0 & 0 & 0 & \sqrt{3} \\ 0 & 0 & 0 & 0 & -1 \\ \hline 0 & 0 & 0 & -1 & 0 \\ 0 & 0 & -1 & 0 & 0 \\ \sqrt{3} & -1 & 0 & 0 & 0 \end{array}\right)$$

$$L_z = \left(\begin{array}{cc|ccc} 0 & 0 & 0 & 0 & 0 \\ 0 & 0 & 2i & 0 & 0 \\ \hline 0 & -2i & 0 & 0 & 0 \\ 0 & 0 & 0 & 0 & -i \\ 0 & 0 & 0 & i & 0 \end{array}\right); \tag{3.35}$$

the matrices are written in the cubic basis in the order as in (3.33), i.e., the lower right block is the t_{2g} block. The transformation T from the spherical harmonics to the t_{2g} shell is not unitary, because $TT^\dagger = 1$ (the 3×3 identity matrix) but $T^\dagger T \neq 1$. Therefore, $TL_zT^\dagger TL_zT^\dagger \neq T(L_zL_z)T^\dagger$. In the framework of *t-p*-equivalence, one needs to transform the orbital operators as $\tilde{L}_i = -TL_iT^\dagger$ (where $i \in \{x, y, z\}$ and the minus sign is due to the negative sign in the *t-p*-equivalence) and the spin operators as $\tilde{S}_i = TS_iT^\dagger$. Then, the L^2, S^2, J_i, J^2 and $\underline{L}\,\underline{S}$ operators are already well-defined. Note that for the $\underline{L}\,\underline{S}$ term it does not matter whether the whole term is transformed or the components are transformed separately.

Using the t-p-equivalence, the $\underline{L} \cdot \underline{S}$-term reads

$$(\underline{L} \cdot \underline{S})_{\text{Block 1}} = \begin{array}{c} \begin{matrix} |d^{\uparrow}_{xy}\rangle & |d^{\downarrow}_{xz}\rangle & |d^{\downarrow}_{yz}\rangle \end{matrix} \\ \begin{pmatrix} 0 & -\frac{1}{2} & -\frac{1}{2} \\ -\frac{1}{2} & 0 & \frac{1}{2} \\ -\frac{1}{2} & \frac{1}{2} & 0 \end{pmatrix} \end{array}. \tag{3.36}$$

Again, the second block is the conjugate of the first block[2].

The eigenbasis of that $\underline{L} \cdot \underline{S}$ term in the t_{2g} subshell is given by the effective atomic j-basis (as opposed to the real j-basis, where the sign of the $\underline{L}$-operator is not flipped)

$$\begin{aligned}
\left|j_{eff} = \frac{3}{2}, m_j = -\frac{3}{2}\right\rangle &= -\left|m_\ell = 1, m_s = -\frac{1}{2}\right\rangle \\
\left|j_{eff} = \frac{3}{2}, m_j = -\frac{1}{2}\right\rangle &= \frac{1}{\sqrt{3}}\left|m_\ell = 1, m_s = \frac{1}{2}\right\rangle + \frac{1}{\sqrt{3}}\left|m_\ell = -2, m_s = -\frac{1}{2}\right\rangle - \frac{1}{\sqrt{3}}\left|m_\ell = 2, m_s = -\frac{1}{2}\right\rangle \\
\left|j_{eff} = \frac{3}{2}, m_j = \frac{1}{2}\right\rangle &= -\frac{1}{\sqrt{3}}\left|m_\ell = -2, m_s = \frac{1}{2}\right\rangle + \frac{1}{\sqrt{3}}\left|m_\ell = 2, m_s = \frac{1}{2}\right\rangle + \frac{1}{\sqrt{3}}\left|m_\ell = -1, m_s = -\frac{1}{2}\right\rangle \\
\left|j_{eff} = \frac{3}{2}, m_j = \frac{3}{2}\right\rangle &= -\left|m_\ell = -1, m_s = \frac{1}{2}\right\rangle \\
\left|j_{eff} = \frac{1}{2}, m_j = -\frac{1}{2}\right\rangle &= \frac{2}{\sqrt{6}}\left|m_\ell = 1, m_s = \frac{1}{2}\right\rangle - \frac{1}{\sqrt{6}}\left|m_\ell = -2, m_s = -\frac{1}{2}\right\rangle + \frac{1}{\sqrt{6}}\left|m_\ell = 2, m_s = -\frac{1}{2}\right\rangle \\
\left|j_{eff} = \frac{1}{2}, m_j = \frac{1}{2}\right\rangle &= \frac{1}{\sqrt{6}}\left|m_\ell = -2, m_s = \frac{1}{2}\right\rangle - \frac{1}{\sqrt{6}}\left|m_\ell = 2, m_s = \frac{1}{2}\right\rangle + \frac{2}{\sqrt{6}}\left|m_\ell = -1, m_s = -\frac{1}{2}\right\rangle
\end{aligned} \tag{3.37}$$

or expressed in cubic harmonics

$$\begin{aligned}
\left|j_{eff} = \frac{3}{2}, m_j = -\frac{3}{2}\right\rangle &= -\frac{1}{\sqrt{2}}\left|d^{\downarrow}_{xz}\right\rangle + \frac{1}{\sqrt{2}}\left|d^{\downarrow}_{yz}\right\rangle \\
\left|j_{eff} = \frac{3}{2}, m_j = -\frac{1}{2}\right\rangle &= -\frac{2}{\sqrt{6}}\left|d^{\downarrow}_{xy}\right\rangle + \frac{1}{\sqrt{6}}\left|d^{\uparrow}_{xz}\right\rangle - \frac{1}{\sqrt{6}}\left|d^{\uparrow}_{yz}\right\rangle \\
\left|j_{eff} = \frac{3}{2}, m_j = \frac{1}{2}\right\rangle &= \frac{2}{\sqrt{6}}\left|d^{\uparrow}_{xy}\right\rangle + \frac{1}{\sqrt{6}}\left|d^{\downarrow}_{xz}\right\rangle + \frac{1}{\sqrt{6}}\left|d^{\downarrow}_{yz}\right\rangle \\
\left|j_{eff} = \frac{3}{2}, m_j = \frac{3}{2}\right\rangle &= -\frac{1}{\sqrt{2}}\left|d^{\uparrow}_{xz}\right\rangle - \frac{1}{\sqrt{2}}\left|d^{\uparrow}_{yz}\right\rangle \\
\left|j_{eff} = \frac{1}{2}, m_j = -\frac{1}{2}\right\rangle &= \frac{1}{\sqrt{3}}\left|d^{\downarrow}_{xy}\right\rangle + \frac{1}{\sqrt{3}}\left|d^{\uparrow}_{xz}\right\rangle - \frac{1}{\sqrt{3}}\left|d^{\uparrow}_{yz}\right\rangle \\
\left|j_{eff} = \frac{1}{2}, m_j = \frac{1}{2}\right\rangle &= -\frac{1}{\sqrt{3}}\left|d^{\uparrow}_{xy}\right\rangle + \frac{1}{\sqrt{3}}\left|d^{\downarrow}_{xz}\right\rangle + \frac{1}{\sqrt{3}}\left|d^{\downarrow}_{yz}\right\rangle.
\end{aligned} \tag{3.38}$$

[2] As the cubic basis, (3.33), has two purely imaginary wave functions, the complex conjugate gives an additional minus sign for off-diagonal elements between purely real and purely imaginary wave functions. Written differently, $(\underline{L} \cdot \underline{S})_{\text{Block 2}} = T^{\dagger}(T\,(\underline{L} \cdot \underline{S})_{\text{Block 1}}\,T^{\dagger})^{*}T$, where the matrix T is

$$T = \begin{pmatrix} i & 0 & 0 \\ 0 & 1 & 0 \\ 0 & 0 & i \end{pmatrix}.$$

3.3.3 Numerical j-basis

When treating materials with DFT and then using projective Wannier functions to extract a local description of the correlated shells, often the local Hamiltonian is more complicated than a simple $\underline{L} \cdot \underline{S}$ term with a constant prefactor. In many cases, the ligand field leads to a crystal-field term that need not even be diagonal (e.g., when there are distortions of the octahedral oxygen cages around transition metal atoms in perovskite transition metal oxides). Furthermore, the assumption that the SOC strength is orbital-independent is not always satisfied.

In analogy to the atomic (possibly effective) j-basis, a natural basis for the system can be found by diagonalizing the local non-interacting Hamiltonian. Whenever the SOC is dominant, this basis will be close to the atomic j-basis, which is why we refer to it as *numerical* j-basis. However, this does not mean that in this basis the states can be labeled by j and m_j quantum numbers. Nevertheless, it is possible that the expectation value of the J^2 and J_z operators are close to the expected values for the atomic (possibly effective) j-basis, in which case the states of the numerical j-basis can be interpreted as an approximation to the atomic j-basis.

Sometimes, in the literature, other natural bases for the problem are used, e.g., by diagonalizing the density matrix or the hybridization function at a suitable frequency.

3.3.4 Density-density interaction in the atomic effective j-basis

In order to understand the basic difference of the interaction in the cubic harmonics basis and the atomic effective j-basis, we look at the density-density terms in the Kanamori Hamiltonian. The interaction Hamiltonian in the density-density approximation is

$$H_{int}^{dens} = \sum_{mm'} U_{mm'}^{dens}\ n_m n_{m'}, \tag{3.39}$$

where $U_{mm'}^{dens}$ is the U-matrix describing the interaction of the density-density terms. Note that m is a compound index of orbital and spin again.

In the cubic harmonic basis, the density-density U-matrix is

$$U^{dens} = \begin{array}{c} \begin{array}{cccccc} d_{xy}^{\uparrow} & d_{xz}^{\uparrow} & d_{yz}^{\uparrow} & d_{xy}^{\downarrow} & d_{xz}^{\downarrow} & d_{yz}^{\downarrow} \end{array} \\ \begin{pmatrix} 0 & U_K - 3J_K & U_K - 3J_K & U_K & U_K - 2J_K & U_K - 2J_K \\ U_K - 3J_K & 0 & U_K - 3J_K & U_K - 2J_K & U_K & U_K - 2J_K \\ U_K - 3J_K & U_K - 3J_K & 0 & U_K - 2J_K & U_K - 2J_K & U_K \\ U_K & U_K - 2J_K & U_K - 2J_K & 0 & U_K - 3J_K & U_K - 3J_K \\ U_K - 2J_K & U_K & U_K - 2J_K & U_K - 3J_K & 0 & U_K - 3J_K \\ U_K - 2J_K & U_K - 2J_K & U_K & U_K - 3J_K & U_K - 3J_K & 0 \end{pmatrix} \end{array}. \tag{3.40}$$

The basis states are marked above the matrix.

In the atomic effective j-basis, it is

$$U^{dens} = \begin{array}{c} \begin{matrix} \left|j_{eff}=\frac{3}{2},m_j=-\frac{3}{2}\right\rangle & \left|j_{eff}=\frac{3}{2},m_j=-\frac{1}{2}\right\rangle & \left|j_{eff}=\frac{3}{2},m_j=\frac{1}{2}\right\rangle & \left|j_{eff}=\frac{3}{2},m_j=\frac{3}{2}\right\rangle & \left|j_{eff}=\frac{1}{2},m_j=-\frac{1}{2}\right\rangle & \left|j_{eff}=\frac{1}{2},m_j=\frac{1}{2}\right\rangle \end{matrix} \\ \begin{pmatrix} 0 & U_K-\frac{7}{3}J_K & U_K-\frac{7}{3}J_K & U_K-J_K & U_K-\frac{5}{3}J_K & U_K-\frac{8}{3}J_K \\ U_K-\frac{7}{3}J_K & 0 & U_K-J_K & U_K-\frac{7}{3}J_K & U_K-2J_K & U_K-\frac{7}{3}J_K \\ U_K-\frac{7}{3}J_K & U_K-J_K & 0 & U_K-\frac{7}{3}J_K & U_K-\frac{7}{3}J_K & U_K-2J_K \\ U_K-J_K & U_K-\frac{7}{3}J_K & U_K-\frac{7}{3}J_K & 0 & U_K-\frac{8}{3}J_K & U_K-\frac{5}{3}J_K \\ U_K-\frac{5}{3}J_K & U_K-2J_K & U_K-\frac{7}{3}J_K & U_K-\frac{8}{3}J_K & 0 & U_K-\frac{4}{3}J_K \\ U_K-\frac{8}{3}J_K & U_K-\frac{7}{3}J_K & U_K-2J_K & U_K-\frac{5}{3}J_K & U_K-\frac{4}{3}J_K & 0 \end{pmatrix} \end{array}. \tag{3.41}$$

In the cubic harmonic basis, the same-spin density-density interaction between different orbitals is $U_K - 3J_K$ (i.e., the lowest energy, which gives rise to Hund's first rule, stating that the total spin has to be maximized), the different-spin density-density interaction between different orbitals is $U_K - 2J_K$, and the different-spin density-density interaction between equal orbitals is U_K. In the atomic effective j-basis, there is much more variety. The lowest energy is reached when two electrons have different j_{eff}, different $|m_j|$ and different m_j. When considering just the $j_{eff} = 3/2$ part, the density-density interaction is always $U_K - 7/3J_K$, except for the pairing of two states with same j_{eff} but flipped m_j, which is energetically much more expensive at $U_K - J_K$. In general, the energy spread of the terms is smaller in the j-basis. In the cubic basis, the largest term is U_K and the smallest is $U_K - 3J_K$ (i.e., the difference is $3J_K$); in the j-basis, the largest is $U_K - J_K$ and the smallest is $U_K - 8J_K/3$ (i.e., the difference is $5J_K/3$). This means that Hund's coupling is less effective in the j-basis than in the cubic basis, at least considering just the density-density terms.

4 Impurity Solver

Typically, the most expensive part of a DMFT calculation is solving the impurity problem, which is done by means of an impurity solver. In the following, an introduction to different, widely used impurity solvers will be given. Then, the continuous time Quantum Monte Carlo algorithm in interaction expansion will be explained in more detail, and the implications of complex local Green's functions $G(\tau)$ will be explained. Furthermore, a study of the fermionic sign of a model system in different bases is carried out (the study of that model system is original work by the author of this thesis). Finally, the tail fitting procedure that is necessary due to the statistical error of the results of Quantum Monte Carlo programs is explained, by first summarizing well-known properties of Green's functions and their high-frequency behavior. The introduction of a frequency-dependent error to the tail fit and some modifications of the code for complex-valued Green's functions (in imaginary time) are contributions by the author of this thesis to the TRIQS library.

4.1 Introduction

Since the advent of the DMFT, all kinds of methods have been used to actually solve the Anderson impurity model onto which the Hubbard model is mapped.

In the first work on DMFT [9], iterated perturbation theory [10, 77–80] was used to solve the model. In its most basic form, this just allows the treatment of systems with a single half-filled band, but extensions to multi-orbital systems and away from half-filling can be found in the literature [81, 82]. But even there, that method constitutes an approximation.

An important class of methods for solving the impurity problem are Quantum Monte Carlo methods. At first, the Hirsch-Fye algorithm [83] was employed for DMFT calculations [84–86]. It calculates the impurity Green's function in imaginary time, where the axis is discretized in finite steps, which produces a discretization error. This shortcoming of the method can be remedied by using Monte Carlo algorithms that work in continuous imaginary time; this class of algorithms is called *Continuous Time Quantum Monte Carlo* (CTQMC) [87]. These methods involve expanding the partition function, which is sampled, in orders of parts of the Hamiltonian; depending on the part, there are different flavors of CTQMC, e.g., hybridization expansion (CTHYB) [88], which was used in this work and will be discussed below, and interaction expansion (CTINT) [89]. This allows a statistically exact treatment of the impurity problem, which means that the error, in

principle, vanishes for infinite run times of the algorithm. However, the fact that these methods work on the imaginary time axis also means that it is necessary to perform an analytic continuation (see chapter 5).

Another, widely employed, method is exact diagonalization [10, 90]. There, typically a fit of the hybridization function is performed in order to replace the infinite bath of the Anderson impurity model by a finite number of bath sites. The resulting problem can then be diagonalized; this involves an error due to the bath discretization, but gives access to real-frequency properties without analytic continuation.

Other approaches include slave bosons [91], non-crossing approximation (NCA) [92], numerical renormalization group [93], cluster perturbation theory [94], and density matrix renormalization group and tensor network based approaches [95–97].

In the following, we will only discuss the CTHYB algorithm, which was used in this work.

4.2 Continuous-time Quantum Monte Carlo in hybridization expansion (CTHYB)

The following summary of the CTHYB algorithm follows Emanuel Gull's thesis [98] and review paper [87].

The goal is to solve the Anderson impurity model (2.11), i.e., to calculate its interacting Green's function (in imaginary time). That Hamiltonian H is split into the hybridization term H_{hyb} and the rest H_{lb} (which is the local Hamiltonian and the bath Hamiltonian). Then, the partition function $\mathcal{Z}$ can be written as

$$\mathcal{Z} = \operatorname{Tr} e^{-\beta H} = \operatorname{Tr}\left(e^{-\beta H_{lb}} T_\tau \exp\left\{ -\int_0^\beta d\tau\, H_{hyb}(\tau) \right\} \right), \tag{4.1}$$

where T_τ is the imaginary time-ordering operator and we have

$$H_{hyb}(\tau) = e^{\tau H_{lb}} H_{hyb} e^{-\tau H_{lb}} \tag{4.2}$$

in interaction representation. Here, τ is the imaginary time. The expression for $\mathcal{Z}$ can be expanded in a power series

$$\mathcal{Z} = \sum_{k=0}^{\infty} \int_0^\beta d\tau_1 \cdots \int_{\tau_{k-1}}^\beta d\tau_k \, \operatorname{Tr}\left(e^{-\beta H_{lb}} H_{hyb}(\tau_k) \cdots H_{hyb}(\tau_1) \right). \tag{4.3}$$

Then, the trace can be split into a part only containing bath creation and annihilation operators and a part with only impurity creation and annihilation operators. The non-interacting bath partition function $\mathcal{Z}_{bath}$ can be calculated analytically. It can be shown that the contribution of

the rest of the bath part is the determinant of the hybridization function. Thus,

$$\mathcal{Z} = \mathcal{Z}_{bath} \sum_k \int d\tau_1 \cdots d\tau_k \sum_{l_1 \cdots l_k} \mathrm{Tr}\left(e^{-\beta H_{loc}} T_\tau o_{l_k}(\tau_k) \cdots o_{l_1}(\tau_1)\right) \det \Delta. \tag{4.4}$$

Here, the operators o_l are one of the $c_m^\dagger$ or c_m.

Instead of summing over all the contributions in that expression, we can estimate the total partition function by *importance sampling*. Given the contribution of one of the terms in the sum and integrals, which we call configuration and which is given by the information which operator acts at which time, we want to add the contribution of another configuration if its contribution to the total sum is high. We want to do that such that the probability of being in a certain state is its contribution to the partition function divided by the total partition function. This allows to perform a Markov chain Monte Carlo process with detailed balance, where new states are proposed according to certain updates and accepted according to the probabilities of the current and new state.

While the partition function is sampled, in reality we are interested in the Green's function. Measuring the latter can be achieved by reweighting the determinant, for which fast-update formulas exist. As the expansion is carried out in the hybridization, it is not possible to calculate matrix elements G_{ij} of the Green's function where $\Delta_{ij}(\tau) = 0$.

Unfortunately, there is (in general) no way of ensuring that the contributions to the partition function of all the configurations are positive. But then, it is not possible to interpret the normalized contribution as the probability of the configuration. There is, however, a trick to carry out the Monte Carlo anyway; we express the expectation value of an observable O as

$$\begin{aligned}
\langle O \rangle_p &= \frac{\sum_x O(x) p(x)}{\sum_x p(x)} && (4.5)\\
&= \frac{\sum_x O(x) |p(x)| \operatorname{sign} p(x)}{\sum_x |p(x)| \operatorname{sign} p(x)} \\
&= \frac{\sum_x O(x) |p(x)| \operatorname{sign} p(x)}{\sum_x |p(x)|} \Big/ \frac{\sum_x |p(x)| \operatorname{sign} p(x)}{\sum_x |p(x)|} \\
&= \frac{\langle O \operatorname{sign} p \rangle_{|p|}}{\langle \operatorname{sign} p \rangle_{|p|}}. && (4.6)
\end{aligned}$$

Here, the summation over x is a summation (or, possibly, integration) over all possible configurations x. This means that instead of measuring O, we measure $O \operatorname{sign} p$, but we do that according to the probability distribution $|p|$ which is guaranteed to be positive. We also have to measure the average sign and then reweight the expectation value of the observable.

If the different configurations that are sampled do not mostly have the same sign, the average sign will be small; then the division by a small number in (4.6) will increase the statistical error (as both the numerator and denominator have a statistical error). Considering the free energy $F_p = -\beta^{-1} \log \mathcal{Z}_p = f_p V$ (for the real partition function $\mathcal{Z}_p$ using the positive and negative

contributions) and $F_{|p|} = -\beta^{-1} \log \mathcal{Z}_{|p|} = f_{|p|} V$ (for the ficticious partition function using the absolute value of the contributions), with free energy densities f_p and $f_{|p|}$, the configuration space volume V, and the inverse temperature β, we get

$$\Delta f = f_p - f_{|p|} = -(\beta V)^{-1} \log \frac{\mathcal{Z}_p}{\mathcal{Z}_{|p|}}. \tag{4.7}$$

Therefore,

$$\langle \operatorname{sign} p \rangle = \frac{\mathcal{Z}_p}{\mathcal{Z}_{|p|}} = e^{-\beta V \Delta f}. \tag{4.8}$$

Thus, the statistical error of the measured quantities grows exponentially with configuration space volume and inverse temperature. This exponential scaling of the algorithm is referred to as the *sign problem*; it prevents getting good statistics without exponentially increasing computation time. Unlike expectation values of physical observables, the average value of the sign changes upon a basis transformation with unitary matrices, as in (2.47).

4.3 Complex hybridization and local Hamiltonian

In many highly symmetric crystals, the local Green's function (and, thus, the DMFT self-energy) is diagonal in the cubic basis. However, lattice distortions can often lead to hybridizations between orbitals, which is seen as off-diagonal elements in G_{loc}. Nevertheless, the Hermitian $G(\tau)$ often remains real in the cubic basis or can be transformed, by means of a unitary transformation, to a basis where all matrix elements are real. The presence of spin-orbit coupling, in general, leads to a complex-valued $G(\tau)$ that is not purely real in any basis (due to the Hermiticity its diagonal elements, however, are real).

In that case, usually both the hybridization $\Delta(\tau)$ and the local Hamiltonian (i.e., the local non-interacting Hamiltonian and the interaction term) are complex. This requires a CTHYB code that can handle these complex numbers; the TRIQS application TRIQS/CTHYB [72] has that functionality. Then, the individual terms of the partition function (4.4) can be complex as well; the possibility of interpreting the contributions as probabilities as in (4.6) using a sign has to be modified. The role of the sign is then played by $e^{i \operatorname{phase} p(x)}$. Note that the average sign (4.8) is the quotient of two partition functions and, thus, real-valued.

From a user's point of view, during the installation of TRIQS/CTHYB, in order to use the complex version the two cmake-flags `HYBRIDISATION_IS_COMPLEX` and `LOCAL_HAMILTONIAN_IS_COMPLEX` have to be turned on. As mathematical operations with complex numbers are slower than with real numbers, it is recommended to use the complex version only when necessary. The usage of the solver is then exactly the same as with real numbers (see, however, the notes on the tail fit in section 4.5), but complex hybridizations and local Hamiltonians are possible.

Apart from the slowdown due to the complex arithmetic, typically the sign problem is more severe with complex off-diagonal elements. In some cases, a change of basis can be performed to

get a reasonable sign (see below).

4.4 Sign study

Depending on the system, the cause of the sign problem can be primarily

1. the local non-interacting Hamiltonian H^0_{loc} [99, 100],
2. the hybridization $\Delta(i\omega)$ [101], or
3. the interaction H_{int} [64],

or a combination thereof. Typically, for vanishing H^0_{loc} or $\Delta(i\omega)$, no sign problem appears. If the sign problem vanishes for $U \to 0$, it is caused by the interaction. In that case, a different basis has to be chosen (but as usual, there is no guarantee that there is a basis with acceptable sign). This case is extensively discussed in Ref. [64]. However, for the case that the sign problem is not mainly due to the interaction, there are three regimes:

1. H^0_{loc} dominates the sign problem,
2. $\Delta(i\omega)$ dominates, or
3. both contribute to the sign problem on equal footing.

If H^0_{loc} dominates, the best basis is empirically the one that diagonalizes H^0_{loc}; if $\Delta(i\omega)$ dominates, it is advisable to choose a basis that minimizes the off-diagonal elements of $\Delta(i\omega)$. Due to the frequency dependence of the hybridization, this is less clearly defined. One possible approach is to diagonalize the first moment of the high-frequency tail of $\Delta(i\omega)$, i.e., the leading order in $(i\omega)^{-1}$ of $\Delta(i\omega)$ for $i\omega \to \infty$. In the regime where both are important factors, there is in general no basis that diagonalizes both influences and no transformation gives an acceptable sign. Then, the chances of finding a good basis for the sign (at least for low temperature) are low.

4.4.1 Model definition

To illustrate these points, we construct a two-band model on the square lattice, given by the following Hamiltonian:

$$H = \sum_{\sigma} \left(\sum_{i} \varepsilon_{mm'} c^{\dagger}_{im\sigma} c_{im'\sigma} + \sum_{\langle ij \rangle} t_{mm'} c^{\dagger}_{im\sigma} c_{jm'\sigma} \right) . \tag{4.9}$$

The matrix $\varepsilon_{mm'}$ characterizes the local Hamiltonian H^0_{loc} and the hopping term $t_{mm'}$ influences the hybridization Δ. The parameters are chosen as

$$\varepsilon = s_\varepsilon \begin{pmatrix} 1 & \frac{1}{3}e^{-i} \\ \frac{1}{3}e^{i} & 1 \end{pmatrix},$$
$$t = s_t \begin{pmatrix} 1 & \frac{1}{3}e^{i} \\ \frac{1}{3}e^{-i} & 1 \end{pmatrix}.$$

For simplicity, this model is investigated in the non-interacting case, which is a non-trivial task for the CTHYB algorithm. The Brillouin zone was sampled with 100×100 k-points.

The one-particle basis is varied by rotating, according to (2.52), the problem using a special unitary transformation parametrized by

$$R(\chi, \phi, \psi) = \begin{pmatrix} \cos\chi \cdot e^{-i\phi} & -\sin\chi \cdot e^{i\psi} \\ \sin\chi \cdot e^{-i\psi} & \cos\chi \cdot e^{i\phi} \end{pmatrix}. \tag{4.10}$$

4.4.2 Sign of the model in different bases

Figure 4.1 shows the fermionic sign for different bases. Only in the vicinity of the bases that diagonalize H^0_{loc} (which we call H^0_{loc}-basis from now on) or the first moment of $\Delta(i\omega)$ (called Δ-basis) is the sign close to one. The lower the temperature (the higher β), the narrower is the region around these good bases where the sign is high. In order to investigate which of these two bases is better suited, we look at different regimes of the model by scaling the on-site term by a factor s_ε and the hopping term by a factor s_t (see bottom of figure 4.1).

Whenever the hopping is completely turned off ($s_t = 0$), the problem reduces to a single atom; this problem cannot be solved in hybridization expansion as the hybridization is zero. If the hopping is significantly lower than the on-site term, in both the H^0_{loc}- and the Δ-basis a good sign is achieved. However, if both terms have a similar magnitude ($s_\varepsilon = s_t$; then, the relevant energies of the two terms have the same magnitude), diagonalizing the local Hamiltonian leads to much better results than going to the Δ-basis. For low on-site energy but a high hopping term, the Δ-basis works better; the difference between the two bases is not large at $\beta = 10$, but at lower temperature (higher β), this can be expected to make a larger difference.

This study shows why the strategy to diagonalize H^0_{loc}, which can be found throughout the literature [99, 100], is beneficial; most of the time it is this basis which gives the best sign.

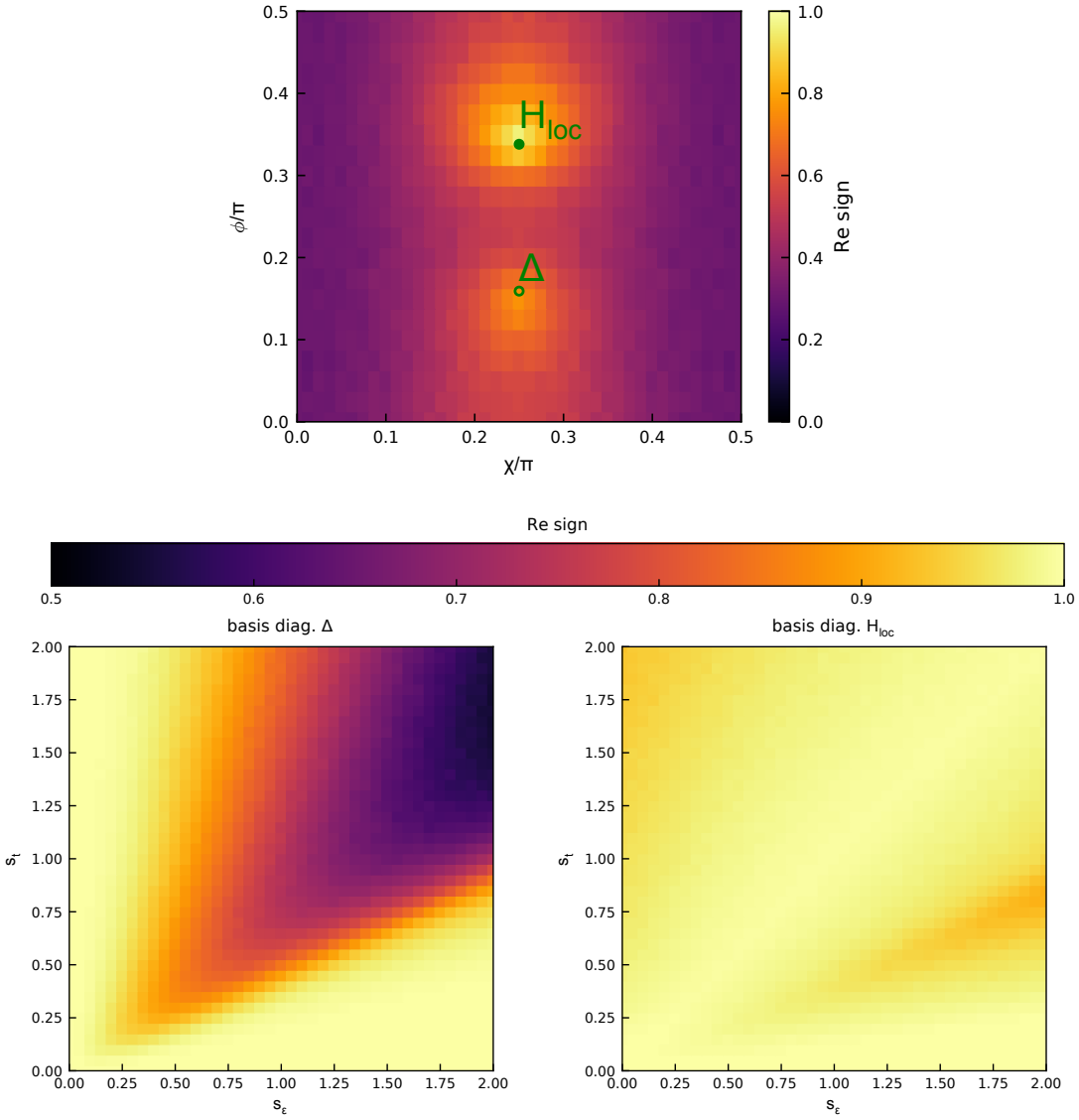

Figure 4.1: Top: Average fermionic sign (real part, the imaginary part is $< 3 \cdot 10^{-2}$) of the model (4.9) in different one-particle bases parametrized by the rotation matrix $R(\chi, \phi, \phi)$ from (4.10) for $s_\varepsilon = s_t = 1$ at $\beta = 10$. Empirically one sees that the sign only depends on $\phi + \psi$ and therefore $\phi = \psi$ has been used. A set of parameters equivalent to the one that diagonalizes H^0_{loc} is marked with a filled green circle, a transformation equivalent to the one that diagonalizes the first moment of $\Delta(i\omega)$ is marked with an empty green circle. Bottom: For these two special bases, the real part of the sign is plotted as a function of the scaling parameters s_ε and s_t.

4.5 Tail fitting

When performing a CTHYB calculation, the error of the self-energy increases (roughly quadratically, see below) with $|\omega_n|$. This means that, typically, the quality of the self-energy data is only acceptable around $\omega_n = 0$. In the self consistency cycle of the DMFT, the large noise for large Matsubara frequencies can lead to instabilities and unphysical behavior. Therefore, a strategy to stabilize the cycle by suppressing that noise is necessary.

It is possible to limit the noise by several schemes. For instance, it is possible to measure the impurity Green's function (and, thus, the self-energy) in τ represented by a basis of Legendre polynomials [102]. Then, the coefficients of the Legendre polynomials drop towards zero for high orders. Setting all coefficients above a certain threshold to zero eliminates the noise of Σ for high Matsubara frequencies.

Another, related, strategy is the use of an intermediate representation [103] between real and imaginary frequencies, which is given by the singular value basis obtained by singular value decomposition (SVD) of the kernel of the analytic continuation (see below, chapter 5). Again, the coefficients of the singular vectors drop to zero with lower singular values, allowing to introduce a cutoff that reduces the noise.

The classical approach to tackle the problem, however, is to perform a so-called *tail fit* (TF), where the coefficients of the high-frequency Laurent expansion of the self-energy are fitted to the data. Of course, in practice, only terms up to a finite order in $i\omega_n$ are considered. This is the route chosen in this work, and in the following some peculiarities of the tail fit for self-energies corresponding to complex-valued Green's functions $G(\tau)$ will be discussed.

4.5.1 Symmetries of Green's functions

The Matsubara Green's function obeys the symmetry relations

$$G^*_{m'm}(-i\omega) = G_{mm'}(i\omega), \tag{4.11}$$

which means that

$$\operatorname{Re} G_{m'm}(-i\omega) = \operatorname{Re} G_{mm'}(i\omega) \qquad \text{and} \qquad \operatorname{Im} G_{m'm}(-i\omega) = -\operatorname{Im} G_{mm'}(i\omega). \tag{4.12}$$

This works both for interacting and non-interacting Green's functions. Furthermore, the inverse of G obeys the same symmetry relations as G itself[1]. Knowing that, from Dyson's equation

$$\Sigma_{mm'}(i\omega) = (G_0^{-1})_{mm'}(i\omega) - (G^{-1})_{mm'}(i\omega), \tag{4.13}$$

[1] This result can be obtained from (4.11) by multiplying with the inverse of $G(i\omega)$ from the left and the inverse of $G^\dagger(-i\omega)$ from the right.

it can be deduced that also $\Sigma(i\omega)$ behaves that way. It is possible to use this symmetry to increase statistics after a QMC run by averaging the two symmetric partners.

The Matsubara Green's function is the Fourier transform of the imaginary-time Green's function

$$G_{mm'}(i\omega_n) = \int_0^\beta d\tau\, e^{i\omega_n\tau} G_{mm'}(\tau). \tag{4.14}$$

Therefore, if $G(\tau)$ is real,

$$G_{mm'}(i\omega_n) = \int_0^\beta d\tau\, (\cos(\omega_n\tau) + i\sin(\omega_n\tau))\, \mathrm{Re}\, G_{mm'}(\tau), \tag{4.15}$$

then $\mathrm{Re}\, G(i\omega_n)$ is symmetric while $\mathrm{Im}\, G(i\omega_n)$ is anti-symmetric. That symmetry is not present once $G(\tau)$ has complex off-diagonal elements.

4.5.2 High-frequency expansion

The expansion of Green's functions can be deduced from the expansion of $(i\omega - H)^{-1}$ around $\omega_n \to \infty$,

$$\begin{aligned}(i\omega - H)^{-1} = \sum_{n=1}^{\infty} H^{n-1}(i\omega)^{-n} &\approx \frac{1}{i\omega}\mathrm{Id} + \frac{H}{(i\omega)^2} + \frac{H^2}{(i\omega)^3} + \frac{H^3}{(i\omega)^4} + \cdots \\ &\approx -\frac{i}{\omega}\mathrm{Id} - \frac{H}{\omega^2} + \frac{iH^2}{\omega^3} + \frac{H^3}{\omega^4} - \frac{iH^4}{\omega^5} - \frac{H^5}{\omega^6} + \frac{iH^6}{\omega^7} + \cdots .\end{aligned} \tag{4.16}$$

Furthermore, the expansion can be expressed by means of the (interacting or non-interacting) spectral function [104],

$$G_{mm'}(i\omega) = \sum_{n=1}^{\infty} \frac{\int_{-\infty}^{\infty} d\omega'\, A_{mm'}(\omega')\omega'^{n-1}}{(i\omega)^n}. \tag{4.17}$$

This means that the nth expansion coefficient a_n is the $(n-1)$st moment of the spectral function. From the fact that the 0th moment (i.e., the norm) of $A_{mm'}(\omega)$ is $\delta_{mm'}$, one finds that the lowest-order contribution is $1/(i\omega)$ for the diagonals and $\sim 1/(i\omega)^2$ for the off-diagonals of $G(i\omega)$. If $A_{mm'}(\omega)$ is real (as is always the case at least for its diagonal elements), the expansion coefficients will be real; then, the even orders constitute the real part of the high-frequency tail of $G(i\omega)$ and the odd orders form the imaginary part. For complex $A_{mm'}(\omega)$, all the orders contribute both to the real and the imaginary part of the tail. This expansion also shows that the expansion coefficients for $i\omega \to +i\infty$ and $i\omega \to -i\infty$ are equal. As $A(\omega)$ is Hermitian for physical systems, also the expansion coefficients are: $(a_n)_{mm'} = (a_n)^*_{m'm}$.

The expansion coefficients b_j of the inverse G^{-1} of a Green's function G with expansion coefficients

a_j can be written recursively (for $m \geq 0$) as

$$b_m = -\sum_{p=-1}^{m-1} a_1^{-1} a_{m+1-p} b_p, \tag{4.18}$$

where $b_{-1} = a_1^{-1}$.

As $\Sigma(i\omega) = G_0^{-1}(i\omega) - G^{-1}(i\omega)$ and both G_0^{-1} and G^{-1} share the same linear $i\omega$ term, this order vanishes in Σ and the first order in the self-energy is the constant term. Then,

$$\Sigma(i\omega) \approx \sum_{n=0}^{\infty} c_n \cdot (i\omega)^{-n}. \tag{4.19}$$

When separating that into real and imaginary part, we get

$$\begin{aligned}
\operatorname{Re}\Sigma(i\omega) &\approx \sum_{k=0}^{\infty} (\operatorname{Re} c_{2k}) \cdot \operatorname{Re}[(i\omega)^{-2k}] + \sum_{k=0}^{\infty} (\operatorname{Im} c_{2k+1}) \cdot \operatorname{Re}[i(i\omega)^{-(2k+1)}], \\
\operatorname{Im}\Sigma(i\omega) &\approx \sum_{k=0}^{\infty} (\operatorname{Im} c_{2k}) \cdot \operatorname{Im}[i(i\omega)^{-2k}] + \sum_{k=0}^{\infty} (\operatorname{Re} c_{2k+1}) \cdot \operatorname{Im}[(i\omega)^{-(2k+1)}].
\end{aligned} \tag{4.20}$$

This means that it is possible to fit the real and imaginary part of Σ separately using a fit routine working with real numbers, but that the resulting fit parameters determine either the real or imaginary part of the final complex fit coefficient depending on the order of the fit coefficient (even or odd).

Given that $\Sigma(i\omega) = \Sigma^\dagger(-i\omega)$ and that the coefficients for $i\omega \to +i\infty$ and for $i\omega \to -i\infty$ are the same, there are actually four different tails of a matrix-valued self-energy that are described by the same tail fit coefficients: $\Sigma_{mm'}(i\omega)$, $\Sigma_{mm'}(-i\omega)$, $\Sigma_{m'm}(-i\omega)$, $\Sigma_{m'm}(i\omega)$. The first condition, $\Sigma(i\omega) = \Sigma^\dagger(-i\omega)$, can be enforced in Σ (typically the noisy Σ) by performing an appropriate symmetrization. The second condition is not valid for Σ, but only for its tail, so it cannot be incorporated into the data of Σ itself. Therefore, it is advisable to fit the positive and negative tail of $\Sigma_{mm'}$ in one go. For real $G(\tau)$, this is not necessary, because then the real part of $\Sigma(i\omega_n)$ is symmetric and the imaginary part is antisymmetric.

In practice, the fit is performed in a so-called fit window $\mathcal{F}$; only Matsubara frequencies within that window are taken into account for the misfit of the least-squares fit. The lower bound of the fit window is introduced because the data for low $|\omega_n|$ is typically not noisy and does not follow the analytic behavior of the high-frequency tail. The upper bound has to be used because the data gets too noisy for large $|\omega_n|$ (but, this can be omitted, see below).

For complex $G(\tau)$, the fit window consists of two parts, $\mathcal{F}_- = [n_1^-, n_2^-]$ and $\mathcal{F}_+ = [n_1^+, n_2^+]$ (where $n_1^- < n_2^-$ are negative and $n_1^+ < n_2^+$ are positive Matsubara frequency indices) for positive and negative frequencies. To ensure that the fit parameters are Hermitian, (for fermions) the fit for $\Sigma_{m'm}$ (note the swapped matrix indices) has to be performed with $\mathcal{F}'_- = [-n_2^+ - 1, -n_1^+ - 1]$ and

$\mathcal{F}'_+ = [-n_2^- - 1, -n_1^- - 1]$. The switch between the positive and the negative part of the window is due to the minus sign in $\Sigma(i\omega) = \Sigma^\dagger(-i\omega)$, and the additional offsets by -1 are because the fermionic Matsubara frequencies are $i\omega_n = i(2n+1)\pi/\beta$, i.e., $i\omega_n = -i\omega_{-n-1}$. When using two symmetric parts of the window, $\mathcal{F}_- = [-n_2 - 1, -n_1 - 1]$ and $\mathcal{F}_+ = [n_1, n_2]$ can be used for both $\Sigma_{mm'}$ and $\Sigma_{m'm}$.

4.5.3 Error estimate[2]

When fitting the tail, one searches for fit parameters p – written here as argument of the fit function $f(i\omega; p)$ – that minimize the function

$$\chi^2 = \sum_k \left(\frac{f(i\omega_k; p) - \Sigma(i\omega_k)}{\sigma(i\omega_k)} \right)^2 . \tag{4.21}$$

Although in principle accessible from CTQMC calculations, the errors $\sigma(i\omega_k)$ are usually not known in practice. The simplest case is to assume that $\sigma(i\omega_k)$ is constant; then it can be ignored because it does not play a role in the minimization.

However, it is a better approximation to assume that the error is constant in $G(\tau)$ as a function of τ than to assume a constant error in $\Sigma(i\omega)$. The Fourier transform of white Gaussian noise is white Gaussian noise, so also $G(i\omega)$ has a roughly constant error. According to the Dyson equation, $\Sigma(i\omega) = G_0^{-1}(i\omega) - G^{-1}(i\omega)$. Assuming that $G_0(i\omega)$ has no statistical error (which is the case in the first DMFT iteration), the error of Σ only comes from the error in $G(i\omega)$.

In leading order, for $i\omega \to i\infty$, $\operatorname{Re} G(i\omega) \sim 1/\omega^2$ and $\operatorname{Im} G(i\omega) \sim 1/\omega$. Then, in leading order, both $\Delta \operatorname{Re} \Sigma(i\omega)$ and $\Delta \operatorname{Im} \Sigma(i\omega)$ go like $\sim \omega^2$.

This is consistent to Ref. [105], where the error of the self-energy is given as

$$\Delta\Sigma(i\omega_n) = G^{-2}(i\omega_n)\Delta G(i\omega_n) \tag{4.22}$$

and $\Delta G(i\omega_n)$ is linearly related to the (assumedly constant) error of $G(\tau)$. Applying our logic that $G(i\omega_n) \sim \omega_n^{-1}$ to this expression leads again to $\Delta\Sigma(i\omega_n) \sim \omega_n^2$.

Any constant prefactor can, of course, be ignored. Then, one needs to minimize

$$\chi^2 \sim \sum_k \left(\frac{f(i\omega_k; p) - \Sigma(i\omega_k)}{|(i\omega_k)^2|} \right)^2 . \tag{4.23}$$

This can be achieved in the fit routine by dividing both the fit function $f(i\omega)$ and the self-energy $\Sigma(i\omega)$ by $|(i\omega_k)^2|$.

Introducing this Matsubara-frequency dependent error, the necessity of using an upper bound

[2] I want to thank Michael Rumetshofer, who inspired me to think about this improvement of the tail fit.

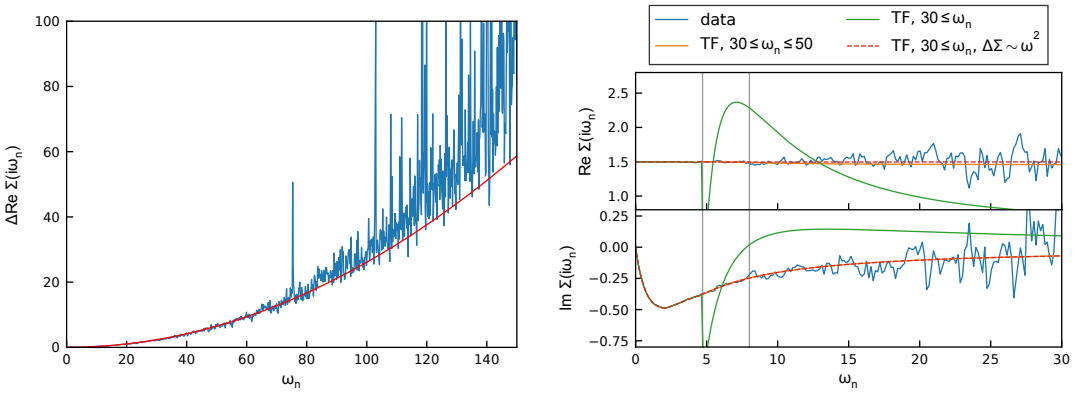

Figure 4.2: Left: Estimated error of the real part of $\Sigma(i\omega_n)$ (blue curve). The estimated error of the imaginary part qualitatively looks the same (apart from different noise). Fit of a curve $\sim \omega_n^2$, taking into account only $\omega_n < 70$ (red curve). Right: Tail fit of the real and imaginary part of the self-energy Σ. All tail fits use 4 fitted moments. The usual tail fit (orange curve) is a tail fit performed assuming constant error in Σ, with a tail fit window from Matsubara index 30 ($i\omega_n = 4.79i$) to 50 ($i\omega_n = 7.93i$), marked by the vertical gray lines. The other two tail fits (green and dashed red curve) were performed in a window from Matsubara index 30 to 1024 (i.e., the last available Matsubara index). Once (green curve), the error was assumed constant, resulting in a poor fit; once (dashed red curve), it was assumed to be $\sim \omega_n^2$, giving a very good tail fit.

for the tail fit window drops; it is possible to fit all the way to the highest available Matsubara frequency. Furthermore, the sensitivity of the fit result to the expansion order is reduced.

To illustrate this, the self-energy of the first DMFT iteration of the single-band Bethe lattice with $t = 1$, $U = 3$ was calculated 100 times (i.e., with 100 different Monte Carlo runs using different random number seeds) to estimate[3] the ω_n-dependence of the error at $\beta = 40$.

The error estimate is found in the left plot in figure 4.2. The behavior is roughly quadratic in ω_n. This is compatible to the estimate given above, which neglects higher orders.

Using a quadratic error for weighting the contributions of χ^2 in the tail fit, the upper end of the tail fit window can be set to the maximum Matsubara index (e.g., 1024 by default). This is demonstrated in the right plot of figure 4.2. The usual tail fit assuming a constant error of $\Sigma(i\omega_n)$ performed in a tail fit window chosen by the author's trained eye and the fit using a $\Delta\Sigma \sim \omega_n^2$ without setting the upper bound of the tail fit window give an equally good result. Thus, there is one less parameter for the tail fit when taking into account the error. All in all, just one tail fit parameter remains: the start position of the fit.

[3]The usual expression for the standard error is used, i.e. $\Delta\Sigma = \sqrt{\sum_i (\Sigma_i - \bar{\Sigma})^2} / \sqrt{N(N-1)}$ where the 100 different self-energies are the Σ_i, their mean is $\bar{\Sigma}$ and $N = 100$.

4.5.4 Implementation

Here, a quick overview of the implementation of the tail fit in TRIQS is given[4].

As mentioned above, in the real-valued case (i.e., the case where the $G(\tau)$ corresponding to $G_0(i\omega)$, $G(i\omega)$ and, thus, $\Sigma(i\omega)$ is real-valued), the odd orders only contribute to the real part of Σ and the even orders only to the imaginary part; all fit coefficients are real. Therefore, the fit is performed in two steps, once for the even and once for the odd orders. The fit itself is performed using the standard `gelss` program for a least-squares fit; it solves a system of linear equations, where the design matrix M consists of one column per order and one row per data point (its entries are the frequencies ω_n^k, where k is the fitted order). The inhomogeneity vector are the values of the self-energy at the individual frequencies. Thus, the $2N$ equations (where N is the number of Matsubara frequencies inside the fit window $\mathcal{F}$)

$$\begin{aligned} \sum_{k \text{ odd}} a_k \omega_n^k &= \operatorname{Re} \Sigma(i\omega_n) \\ \sum_{k \text{ even}} a_k \omega_n^k &= \operatorname{Im} \Sigma(i\omega_n) \end{aligned} \tag{4.24}$$

are solved for a_k in the least-squares sense. The sum over the orders goes from the minimal unknown order to the maximal order to be fitted, which has to be set by the user. The Matsubara frequency-dependence of the error can be incorporated by appropriately scaling the input to the fit routine, see (4.23). For matrix-valued self energies, each element is fitted separately.

In the complex-valued case, the general procedure is the same. As mentioned above, the data in two fit windows, $\mathcal{F}_+$ and $\mathcal{F}_-$ are considered simultaneously. Again, the fit is performed using a real-valued fit routine, but the even and odd orders are used according to (4.20), which yields the real or imaginary part of the complex-valued fit parameters.

Typically, after fitting, the data of Σ for Matsubara frequencies in and above the fit window (below for negative frequencies) are replaced by evaluating the fit function.

The way to use this in a python script is the following, where `Sigma` is a block Green's function, `fit_min_n` defines the Matsubara index of the lower boundary of the fit window, and `fit_max_moment` is the maximum order to be fitted.

```
fit_known_moments = {}
for name, sig in Sigma:
    fit_known_moments = TailGf(len(sig.indicesL),len(sig.indicesR),0,0)
    sig.fit_tail(fit_known_moments,
        fit_max_moment,
        -Sigma[name].mesh.last_index()-1,
        -fit_min_n-1,
        fit_min_n,
```

[4] The author supplied a pull request to the TRIQS library that corrected the code of the tail fit in the complex-valued case (namely by fitting the two windows in one go) and introduced the frequency-dependent error from the previous section.

```
        Sigma[name].mesh.last_index(),
        error_omega=2.0)
```

5 Analytic continuation of matrix-valued Green's functions

The CTHYB impurity solver (and also many other commonly used methods) gives results on the imaginary-time or imaginary-frequency axis. If one is interested in real-frequency (or real-time) quantities (such as, e.g., spectral functions), an analytic continuation has to be performed. While many methods exist for that procedure, as soon as the Green's function of self-energy of interest has off-diagonal elements, there are some additional complications. Therefore, we conceived a method based on the Maximum Entropy formalism that gives results also for the off-diagonal elements of matrix-valued spectral functions.

This method was presented in a paper both on the arXiv and in Physical Review B [106]. The author devised the idea of the positive-negative entropy, which was further developed with Robert Triebl, who put it on a more rigorous footing. Furthermore, the parametrization in the full matrix formulation was conceived by the author. He implemented a maximum entropy code in python that can handle different expressions for the cost function, among them the ones used in the paper. The poor man's matrix method is largely due to Manuel Zingl, who also tested the different ways to analytically continue the self-energy. The two-band model was designed and studied by the author. The $LaTiO_3$ calculations were performed by Manuel Zingl; the analytic continuation was carried out by Manuel Zingl and the author. Appendix 5.6 was the work of Robert Triebl, while the other appendices, 5.7 and 5.8, were done by the author. The paper, especially the parts not yet attributed to a certain author, was written up as a collaborative effort between all authors, and all authors contributed their ideas and improvements to all parts of the paper.

In the following, that paper is included in its entirety[1].

[1] In order to remain consistent, the use of Eq., Sec., Fig., etc. before references has been adapted with respect to the original paper. The bibliographic references are merged with the references of the thesis, in order to provide one homogeneous list of citations.

PHYSICAL REVIEW B **96**, 155128 (2017)

Maximum entropy formalism for the analytic continuation of matrix-valued Green's functions

Gernot J. Kraberger, Robert Triebl, Manuel Zingl, and Markus Aichhorn*
Institute of Theoretical and Computational Physics, Graz University of Technology, NAWI Graz, 8010 Graz, Austria
(Received 6 June 2017; revised manuscript received 25 August 2017; published 17 October 2017)

Abstract

We present a generalization of the maximum entropy method to the analytic continuation of matrix-valued Green's functions. To treat off-diagonal elements correctly based on Bayesian probability theory, the entropy term has to be extended for spectral functions that are possibly negative in some frequency ranges. In that way, all matrix elements of the Green's function matrix can be analytically continued; we introduce a computationally cheap element-wise method for this purpose. However, this method cannot ensure important constraints on the mathematical properties of the resulting spectral functions, namely positive semidefiniteness and Hermiticity. To improve on this, we present a full matrix formalism, where all matrix elements are treated simultaneously. We show the capabilities of these methods using insulating and metallic dynamical mean-field theory (DMFT) Green's functions as test cases. Finally, we apply the methods to realistic material calculations for $LaTiO_3$, where off-diagonal matrix elements in the Green's function appear due to the distorted crystal structure.

5.1 Introduction

In condensed matter physics, response functions are often calculated in imaginary-time formulation, especially when electronic correlations are taken into account. This is not only true for numerical approaches like Quantum Monte Carlo [83, 87, 107], but also for perturbative techniques such as the random phase approximation [108–110]. However, these quantities cannot be directly related to measurable quantities in real frequency. Quite generally, the Wick rotation $i\tau \to t$, where τ is the imaginary-time argument and t is the real-time argument (or equivalently $i\omega_n \to \omega$, with the nth fermionic Matsubara frequency $\omega_n = (2n+1)\pi/\beta$ and the real frequency ω), transforms the calculated quantities to real frequencies. In practice, this analytic continuation (AC) is not possible straightforwardly, since the kernel of this mapping is ill-conditioned when going from imaginary times to real frequencies. As a result of the kernel being ill-conditioned, small changes of the input will correspond to largely different outputs, rendering the inversion of this problem highly unstable due to numerical noise, where even an error at the level of machine precision can lead to nonsensical results in practice.

This fact has lead to the development of a plethora of different methods trying to efficiently perform the AC. Among them are series expansions (e.g., the Padé method [111–113]), information-

theoretical approaches such as the maximum entropy method (MEM) [114–117] and stochastic methods [118–122]. Other algorithms based on singular value decomposition (SVD) [123], machine learning [124] or sparse modeling [125] tackling the AC have also been presented. Despite all those interesting other developments, the workhorse method for the AC of noisy Monte Carlo data is the MEM.

The methods based on the MEM are well established for the diagonal elements of the Green's function, where the corresponding spectral function can be interpreted as a probability distribution (non-negative normalizable function). There are several freely available codes performing this task, such as ΩMAXENT [126] and the MAXENT code by Levy *et al.* [127].

Nowadays, numerical algorithms do also provide imaginary-time solutions for off-diagonal Green's functions, e.g., in the multiorbital DFT + DMFT [8–10] context relevant for real-material applications. However, due to the lack of reliable methods for performing the AC of the whole Green's function matrix, still the off-diagonal elements are often neglected on different levels of the calculation. One strategy is to transform the impurity problem to some local basis, where the Hamiltonian and hybridization functions are as diagonal as possible and to neglect the off-diagonal elements in the solution of the impurity problem [128]. However, this is an uncontrolled approximation because it is impossible to check the accuracy of this approximation without actually taking the off-diagonal elements into account.

Particularly important is a proper AC for the self-energy. The full matrix form of the self-energy on the real axis is required in the Dyson equation to calculate lattice (k-dependent) quantities of interest. Without ensuring analytic properties such as positive semidefiniteness of this matrix, the results for quantities such as the k-dependent spectral function $A(\mathbf{k}, \omega)$ or derived quantities (e.g., transport, optics) are physically questionable. We will present a method to remedy this problem.

For certain cases, the AC of off-diagonal Green's functions has been tackled before: In general, it is possible to construct an auxiliary Green's function by adding a (possibly frequency-dependent) shift to the off-diagonal elements of the spectral function so that their positivity is ensured. Then, they can be treated with the MEM [129–131]. An example of a work where off-diagonal elements of the impurity spectral function are calculated are the DFT+DMFT calculations of the two perovskites $LaVO_3$ and YVO_3 [132]. Additionally, a stochastic regularization method also suitable for off-diagonal elements has been proposed [133]. However, these methods cannot ensure important matrix properties, e.g., positive semidefiniteness and Hermiticity of the spectral function. Additionally, given the probability theoretical background of the MEM [134], it is unclear how the shift method fits into this theoretical framework.

In other disciplines, such as astronomy and nuclear magnetic resonance (NMR), the MEM has been successfully extended to extract data without the constraint of non-negativity [135–139]. This generalization is not straightforward, as non-negative functions cannot be directly interpreted as probability distributions.

But even with this generalization, important matrix properties are not respected. The purpose of this paper is, thus, to introduce a consistent *matrix* formulation of the MEM completely from probability theory. Using the full matrix enables us to consistently formulate the constraint that the resulting spectral functions are indeed positive semidefinite and Hermitian.

The paper is organized as follows: First, we present the probability theoretical background of the continuation of matrix-valued Green's functions and some computational and implementation details in section 5.2. In section 5.3, we perform a benchmark of the MEM and discuss some practical considerations using a DMFT calculation for a model system. Finally, in section 5.4, we apply the introduced methodology within the framework of DFT+DMFT to the strongly-correlated perovskite $LaTiO_3$.

5.2 Methodology and theory

5.2.1 Basic principles of the maximum entropy method

The retarded one-electron Green's function $G(\omega + i0^+)$ and the Matsubara Green's function $G(i\omega_n)$ are related through the analyticity of $G(z)$ in the whole complex plane with the exception of the poles below the real axis. This connection is explicit by writing the Green's function $G(z)$ in terms of the spectral function $A(\omega)$ as

$$G_{ab}(z) = \int d\omega \frac{A_{ab}(\omega)}{z - \omega}. \tag{5.1}$$

In general, both $G(z)$ and $A(\omega)$ are matrix-valued (with indices a, b), but (5.1) is valid for each matrix element separately. For a given $G_{ab}(\omega + i0^+)$, the matrix-valued $A_{ab}(\omega)$ can be obtained as

$$A_{ab}(\omega) = \frac{i}{2\pi} \left[G_{ab}(\omega + i0^+) - G^*_{ba}(\omega + i0^+) \right]. \tag{5.2}$$

Note that for matrices, the spectral function is not proportional to the element-wise imaginary part of the Green's function.

A drawback of expression (5.1) is that the real and imaginary parts of G and A are coupled due to the fact that z is complex-valued. This is avoided by Fourier-transforming $G(z = i\omega_n)$ to the imaginary time Green's function $G(\tau)$ at inverse temperature β;

$$G_{ab}(\tau) = \int d\omega \, \frac{e^{-\omega\tau}}{1 + e^{-\omega\beta}} A_{ab}(\omega). \tag{5.3}$$

The real part of the spectral function is only connected to the real part of $G(\tau)$, and analogously for the imaginary part. In the following, we will first recapitulate the maximum entropy theory for a real-valued single-orbital problem as presented in Ref. [115] and later generalize to matrix-valued problems.

In order to handle this problem numerically, the functions $G(\tau)$ and $A(\omega)$ in (5.3) can be discretized to vectors $G_n = G(\tau_n)$ and $A_m = A(\omega_m)$; then, (5.3) can be formulated as

$$\underline{G} = K\underline{A}, \tag{5.4}$$

where the matrix

$$K_{nm} = \frac{e^{-\omega_m \tau_n}}{1 + e^{-\omega_m \beta}} \Delta\omega_m \tag{5.5}$$

is the kernel of the transformation. Calculating $G(\tau)$ from $A(\omega)$ is straightforward, but the inversion of the matrix equation (5.4), i.e., calculating $\underline{A}$ via $\underline{A} = K^{-1}\underline{G}$, is an *ill-posed* problem. To be more specific, the condition number of K is very large due to the exponential decay of K_{nm} with ω_m and τ_n, so that the direct inversion of K is numerically not feasible by standard techniques.

The task of the AC is to find an approximate spectral function $\underline{A}$ whose reconstructed Green's function $\underline{G}_{rec} = K\underline{A}$ reproduces the main features of the given data $\underline{G}$, but does not follow the noise (note that here and in the following we use $\underline{G}$ and $\underline{A}$ for the numerical quantities to keep the notation simple). However, a bare minimization of the misfit $\chi^2(\underline{A}) = (K\underline{A} - \underline{G})^T C^{-1} (K\underline{A} - \underline{G})$, with the covariance matrix C, leads to an uncontrollable error [113].

One efficient way to regularize this ill-posed problem is to add an entropic term $S(A)$. This leads to the maximum entropy method (MEM), where one does not minimize $\chi^2(A)$, but

$$Q_\alpha(A) = \frac{1}{2}\chi^2(A) - \alpha S(A). \tag{5.6}$$

The prefactor of the entropy, usually denoted α, is a hyperparameter that is introduced *ad hoc* and needs to be specified. The way to choose α marks various flavors of the maximum entropy approach and will be discussed later (section 5.2.2). This regularization with an entropy has been put on a rigorous probabilistic footing by Skilling in 1989, using Bayesian methods [134]. He showed that the only consistent way to choose the entropy for a non-negative function $A(\omega)$ is

$$S(A) = \int d\omega \left[A(\omega) - D(\omega) - A(\omega) \log \frac{A(\omega)}{D(\omega)} \right], \tag{5.7}$$

where $D(\omega)$ is the default model. The default model influences the result in two ways (see Appendix 5.6 for details): First, it defines the maximum of the prior distribution, which means that in the limit of large α one has $A(\omega) \to D(\omega)$. Second, it is also related to the width of the distribution, since the variance of the prior distribution is proportional to $D(\omega)$. Unless otherwise specified (see, especially, section 5.2.5), we use a flat $D(\omega)$, corresponding to no prior knowledge.

5.2.2 Hyperparameter α

The simplest way to determine α is to choose it such that χ^2 equals the number of τ points [116, 140], which is today known as the historic MEM. Usually, it tends to underfit the data [141]. Other, more sophisticated ways are delivered by the probabilistic picture of Skilling and Gull [134, 142], which are recapitulated in Appendix 5.6. Two frequently used flavors are the classical MEM [142] and the Bryan MEM [143]. A disadvantage is that these probabilistic methods tend to overfit the data as the probability is only evaluated approximately in practice (see Appendix 5.6) [144, 145]. Furthermore, all methods presented so far strongly depend on the provided covariance matrix C. If the statistical error of Monte Carlo measurements, for example, is not estimated accurately, the data could be over- or underfitted.

A rather heuristic approach to overcome these problems is not to consider probabilities, but rather the quality of the reconstruction as a function of α. One way to quantify this is to detect the characteristic kink in the function $\log \chi^2(\log \alpha)$, which indicates the boundary between the noise-fitting and information-fitting regimes [126]. In the noise-fitting region, $\log \chi^2(\log \alpha)$ is essentially constant, while in the information-fitting region, it behaves linearly. In this approach, the optimal α is at the crossover of these regimes, which can be detected, e.g., through the maximum of the second derivative $\partial^2 \log \chi^2 / \partial (\log \alpha)^2$, as implemented the ΩMAXENT code [126].

We propose another way, which is to fit a piecewise linear function to $\log \chi^2(\log \alpha)$, consisting of two straight lines: one for the noise-fitting region (with slope zero) and one for the information-fitting region. The intersection of the two lines, and hence the optimal α, is determined such that the overall fit residual is minimized. This way of determining the optimal α is used throughout the rest of this paper, as it turns out to be stable even in difficult cases where the curvature of $\log \chi^2(\log \alpha)$ shows multiple local maxima.

5.2.3 Positive-negative MEM

For the case of non-matrix-valued or diagonal spectral functions, the MEM described so far became a standard tool used in many different contexts. However, this ordinary MEM is only rigorous for non-negative, additive functions [134]. Nonzero off-diagonal elements of spectral functions clearly violate the non-negativity since their norm

$$\int d\omega A_{ab}(\omega) = \delta_{ab} \tag{5.8}$$

is zero (this follows directly from the Lehmann representation of the spectral function and the anticommutation relations of fermionic operators). Keeping the additivity, one could imagine that the off-diagonal spectral functions originate from a subtraction of two artificial positive functions, i.e., $A(\omega) = A^+(\omega) - A^-(\omega)$. Assuming independence of $A^+(\omega)$ and $A^-(\omega)$, the resulting entropy

is the sum of the respective entropies

$$S(A^+(\omega), A^-(\omega)) = S(A^+(\omega)) + S(A^-(\omega)), \tag{5.9}$$

which was first used for the analysis of NMR spectra [135, 136]. To illustrate the plausibility of this entropy, we use the analogy of the horde of monkeys, which has a long tradition in the field of Bayesian methods. The conventional entropy can be explained by monkeys randomly throwing balls into slots which correspond to different frequencies ω_i on a grid [134]. Then, the number of balls in each slot, related to $A(\omega_i)$, obeys a Poisson distribution with a mean value given beforehand, related to the default model $D(\omega_i)$. From now on, the ω_i dependence of A and D is dropped for simplicity. The subtraction of two positive functions $A = A^+ - A^-$ can be understood with two different hordes of monkeys, one throwing "positive" balls and one throwing "negative" balls. Individually, both the number of positive ($\sim A^+$) and negative ($\sim A^-$) balls again obey a Poisson distribution. The total number of balls in each slot, however, follows a Skellam distribution, which is the convolution of two Poisson distributions. The entropy S describing this process depends on both A^+ and A^- [see (5.9)]. Due to the independence of A^+ and A^-, $S(A^+)$ and $S(A^-)$ follow the same functional form as the conventional entropy (5.7) that stems from the Poisson distribution. Thus,

$$\begin{aligned} S(A^+, A^-) = \int d\omega \Big[& A^+ - D^+ - A^+ \log \frac{A^+}{D^+} \\ & + A^- - D^- - A^- \log \frac{A^-}{D^-} \Big]. \end{aligned} \tag{5.10}$$

The fact that two default models (D^+ and D^-) enter will be discussed later. Several configurations of positive and negative balls give the same net number of balls ($\sim A$), since only their difference $A^+ - A^-$ matters. Hence, an additional superfluous degree of freedom is present once two hordes are acting. Just as the two Poisson distributions of the respective balls lead to a Skellam distribution by integrating out the additional degree of freedom, a reduction of the parameter space from A^+ and A^- to $A = A^+ - A^-$ leads to an entropy $S^{\pm}(A)$ that differs from the conventional entropy in (5.7). The derivation of $S^{\pm}(A)$ was first carried out in the context of cosmic microwave background radiation [137–139], an available software package providing this entropy is MEMSYS5 [146]. This framework is recapitulated here in the context of spectral functions.

The main objective of the MEM is to minimize Q_α as given by (5.6), but the entropy S depends now on both A^+ and A^- as shown in (5.10). The minimum of

$$Q_\alpha(A^+, A^-) = \frac{1}{2}\chi^2(A = A^+ - A^-) - \alpha S(A^+, A^-) \tag{5.11}$$

has to be found with respect to both A^+ and A^-. The misfit χ^2 only depends on the difference $A = A^+ - A^-$. For any fixed A, the minimum of $Q_\alpha(A, A^+)$ is, therefore, realized for the particular choice of A^+ and A^- that maximizes the entropy under the constraint that $A = A^+ - A^-$.

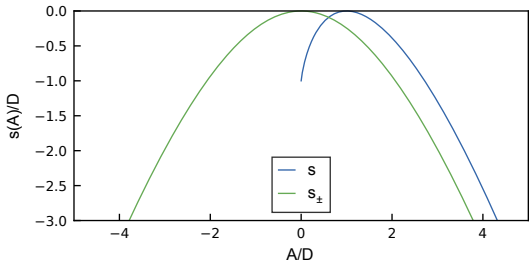

Figure 5.1: Comparison of the "entropy density" of non-negative spectral functions $s(A)$ compatible to (5.7) and of positive and negative spectral functions $s^{\pm}(A)$ compatible to (5.14). The entropy is related to the entropy density via $S(A) = \int d\omega\ s(A(\omega))$. Here, $D^+ = D^- = D$ was assumed.

Expressing A^- in terms of A via $A^- = A^+ - A$, the minimum of $Q_\alpha(A, A^+)$ with respect to A^+ is given by

$$A^+ = \frac{\sqrt{A^2 + 4D^+D^-} + A}{2}, \tag{5.12}$$

$$A^- = \frac{\sqrt{A^2 + 4D^+D^-} - A}{2}. \tag{5.13}$$

A new entropy for functions that can be both positive and negative is then obtained by $S^{\pm}(A) = S\left(A^+(A), A^-(A)\right)$, which we call positive-negative entropy and which reads [139]

$$S^{\pm}(A) = \int d\omega \left[\sqrt{A^2 + 4D^+D^-} - D^+ - D^- - A \log \frac{\sqrt{A^2 + 4D^+D^-} + A}{2D^+} \right]. \tag{5.14}$$

The Bayesian probabilistic interpretation of this entropy is described in Appendix 5.6. In the special case $D^- = 0$, the limit of purely positive functions is recovered since then $S^{\pm}(A) = S(A)$ [the latter being the conventional entropy from (5.7)].

Next, we want to compare the conventional entropy, (5.7), to the positive-negative entropy, (5.14). This comparison can be performed on the level of the integrand of the expression for the entropy, which we refer to as the entropy density $s(A(\omega))$. At a particular frequency value ω_i, the entropy density depends only on the function value of the spectral function $A(\omega_i)$ and the default model $D(\omega_i)$. We therefore plot the entropy density s depending on the function value A at any given ω_i in figure 5.1. The ordinary entropy density $s(A)$ (blue line) is just defined for positive A. Within this definition space, it is concave with a maximum at $A = D$. The variance of the prior distribution around this maximum is also proportional to D (see Appendix 5.6). In the case of $S^{\pm}$, two default models D^+ and D^- are needed, each determining the maximum of the respective spectral functions A^+ and A^- as well as the accompanying variances. Usually, no additional

knowledge about A is available and, therefore, one has to choose $D^+ = D^- = D$ for symmetry reasons (green line in figure 5.1). This is the case for the off-diagonal elements of the spectral functions studied in this work; however, the general case is discussed in Appendix 5.6. For $D^+ = D^- = D$, the maximum of the entropy is at $A = 0$, with a prior variance proportional to D. This demonstrates a fundamental difference of the role of the default model in the conventional and in the positive-negative entropy; in the former, the default model defines both the maximum and the variance of the entropy density, while for the latter it only punishes large values of $|A|/D$. This also means that for $\alpha \to \infty$ the minimization of $Q_\alpha(A)$ gives $A = 0$ for the positive-negative entropy, in contrast to $A = D$ for the conventional entropy.

We note in passing that off-diagonal elements of the spectral function can, of course, be complex-valued. Then, the real and imaginary part of $A(\omega)$ and, correspondingly, $G(\tau)$ can (in principle) be treated separately. The misfit χ^2 and the entropy S for a complex function can therefore be just summed up to a total χ^2 and S. This straightforward generalization of the method is applicable to this and the following sections, but for simplicity we limit ourselves to real-valued spectral functions.

5.2.4 Reduction of the parameter space

In Ref. [143], Bryan presents an algorithm that works in the space of the singular values of K, by means of the singular value decomposition (SVD)[2]

$$K = U \Xi V^T. \tag{5.15}$$

When the problem is discretized with N_τ points on the τ axis and N_ω points on the ω axis, the kernel K is a $N_\tau \times N_\omega$ matrix (we use 684×200) which gets decomposed into the singular-vector matrices U of dimension $N_\tau \times N_\Xi$ and V of dimension $N_\omega \times N_\Xi$ as well as the diagonal matrix Ξ of the singular values. In principle, the number N_Ξ of singular values is given by $\min(N_\tau, N_\omega)$; however, many singular values are on the order of machine precision. Therefore, in practice all singular values below a small threshold (10^{-14} for the results in this paper) can be discarded. This also means that the full vector space of $\underline{A}$, where $A_i = A(\omega_i)$, is larger than necessary (for our calculations, $N_\omega = 200$, while $N_\Xi = 45$).

One important ingredient for each MEM is the optimization of Q_α (5.6) for a given value of α. In Bryan's framework, the stationarity condition $\partial Q_\alpha / \partial \underline{A} = 0$ for the conventional entropy reads

$$-2\alpha \log \frac{\underline{A}}{\underline{D}} = K^T \frac{\partial \chi^2}{\partial (K\underline{A})}, \tag{5.16}$$

[2] We would like to point out that the use of SVD in Bryan's algorithm in the MEM is just for the purpose of choosing a convenient basis for finding the minimum of Q_α. This is fundamentally different from methods where the SVD with a cutoff is used directly for the AC without a regularization by an entropy term (see, e.g., Ref. [123]) or in conjunction with a L_1 regularization to achieve sparseness in the SVD space, as in Ref. [125].

suggesting that a simple way to parametrize $\underline{A}$ in the much smaller singular value basis is

$$\underline{A} = \underline{D} e^{V \underline{u}}, \tag{5.17}$$

where $\underline{u}$ is the new parameter vector of the same dimension as the number of kept singular values. With this parametrization, condition (5.16) becomes

$$\begin{aligned} -2\alpha \underline{u} &= \Xi U^T \frac{\partial \chi^2}{\partial (K \underline{A})} \\ &= \Xi U^T \frac{\partial \chi^2}{\partial (K \underline{D} e^{V \underline{u}})}. \end{aligned} \tag{5.18}$$

The optimization of Q_α has thus been reformulated to the problem of finding the vector $\underline{u}$ that solves (5.18), which does not explicitly depend on $\underline{A}$ anymore. This allows us to carry out the numerical solution in the (smaller) space of $\underline{u}$ instead of $\underline{A}$.

Ansatz (5.17) ensures the positivity of $\underline{A}$, so for the positive-negative approach a different parametrization has to be found in order to use the advantages of the smaller singular space. By doing a similar derivation for $S^\pm$ as the one presented above for the conventional entropy, one realizes that due to

$$\frac{\partial S^\pm}{\partial A_i} = -\log \frac{A_i + \sqrt{A_i^2 + 4 D_i^+ D_i^-}}{2 D_i^+} = -\log \frac{A_i^+}{D_i^+} \tag{5.19}$$

it is easier to express the equations in terms of $\underline{A}^+$ rather than $\underline{A}$. This is possible because of relation (5.12). Given (5.19), a suitable parametrization is given by

$$\underline{A}^+ = \underline{D}^+ e^{V \underline{u}}, \tag{5.20}$$

$$\underline{A}^- = \underline{D}^- e^{-V \underline{u}}, \tag{5.21}$$

$$\underline{A} = \underline{D}^+ e^{V \underline{u}} - \underline{D}^- e^{-V \underline{u}}. \tag{5.22}$$

With this, the condition $\partial Q_\alpha / \partial \underline{A} = 0$ becomes

$$\begin{aligned} -2\alpha \underline{u} &= \Xi U^T \frac{\partial \chi^2}{\partial (K \underline{A})} \\ &= \Xi U^T \frac{\partial \chi^2}{\partial (K (\underline{D}^+ e^{V \underline{u}} - \underline{D}^- e^{-V \underline{u}}))}. \end{aligned} \tag{5.23}$$

Note that this expression looks nearly identical to (5.18). The difference is that $\underline{A}$ is parametrized in terms of $\underline{u}$ by (5.17) in case of non-negative functions and by (5.22) in the generalized case; this enters (5.23) via $\chi^2(\underline{A})$ on the right-hand side.

In principle, the actual search for a vector $\underline{u}$ that fulfills (5.18) or (5.23) can be performed using any suitable numerical procedure; in practice, the Levenberg-Marquardt algorithm is usually (and also in this work) employed [147]. This program to minimize Q_α can be implemented very similarly for both the standard non-negative and the here-presented positive-negative case, the

only changes occur due to the generalization of (5.17) to (5.22).

5.2.5 Poor man's matrix procedure

As discussed before, (5.3) works independently for each element of the matrices $G(\tau)$ and $A(\omega)$. This allows us to perform the AC separately for each matrix element, using the conventional entropy (5.7) for diagonal elements and the modified entropy (5.14) for the off-diagonals.

However, for physical systems, the resulting spectral function matrix has to be positive semidefinite and Hermitian, which is usually not the case when performing the AC separately for each matrix element with a flat default model. Using a flat default model reflects the total absence of previous knowledge on the problem. However, we know that a necessary condition for the positive semidefiniteness of the resulting spectral function matrix is

$$|A_{ll'}| \leq \sqrt{A_{ll} A_{l'l'}}. \tag{5.24}$$

For example, for a problem where all diagonal elements of the spectral function are zero at a certain frequency ω, condition (5.24) implies that also all off-diagonal elements have to be zero at this ω. Thus, once the diagonal elements have been analytically continued, this condition constitutes additional knowledge about the problem which might be incorporated into the MEM framework by choosing the default model for the off-diagonal elements $D_{ll'}(\omega)$ accordingly,

$$D_{ll'}(\omega) = \sqrt{A_{ll}(\omega) A_{l'l'}(\omega)} + \epsilon. \tag{5.25}$$

Here, ϵ is a small number to prevent the default model from becoming zero, so that no division by zero occurs in the entropy term. We will show in section 5.3 and 5.4 that our special choice of the default model (5.25) drastically improves the results of the off-diagonal elements when they are calculated element-wise, although it does not guarantee a positive semidefinite solution. This poor man's matrix approach is especially useful if one wants to upgrade an existing MEM code by only modifying the entropy for off-diagonal elements, as setting the default model is usually a user input.

5.2.6 Full matrix formulation

The only way to ensure that the obtained spectral function is indeed positive semidefinite and Hermitian is by treating the matrix A_{ab} as a whole. Instead of (5.6), the functional to minimize then reads

$$Q_\alpha(A) = \sum_{ab} \left[\frac{1}{2} \chi^2(A_{ab}) - \alpha S(A_{ab}) \right]. \tag{5.26}$$

Here, the ordinary entropy (5.7) is used for the diagonal elements ($a = b$), and accordingly the modified entropy (5.14) is used for off-diagonal elements. One way to ensure the desired

properties of A_{ab} is to introduce an auxiliary matrix B, where $A_{ab} = \sum_c B^*_{ca} B_{cb}$. In contrast to the parametrization of the uncoupled A_{ab} described in section 5.2.4, there is no obvious singular-space parametrization here, since A_{ab} couples different elements of B. However, as the elements B_{ab} can be positive and negative for both diagonal and off-diagonal elements, in the spirit of section 5.2.4 we choose

$$\underline{B}_{ab} = \underline{D}_{ab} \left(e^{V \underline{u}_{ab}} - e^{-V \underline{u}_{ab}} \right). \tag{5.27}$$

Using the resulting parametrization of $\underline{A}_{ab}$ in terms of the singular-space vectors $\underline{u}$, the stationarity condition for Q_α from (5.26) leads to equations which consequently have to be solved for $\underline{u}$ (for a more detailed discussion, see Appendix 5.7). The fact that the expression for A_{ab} now couples the singular-space parameters $\underline{u}$ of different matrix elements means that all matrix elements have to be treated at the same time. Consequently, the configuration space grows quadratically with the matrix size d. Concerning the computational cost, the fundamental difference between the poor man's and the full matrix approach is that in the former, one needs to d^2 times find a solution in a configuration space of size N_Ξ, while in the latter, one searches a solution once in a configuration space of size $N_\Xi \cdot d^2$. As typically solver algorithms take disproportionally longer for larger search spaces, this usually leads to a substantial increase of computational time. Nevertheless, the increased computational effort is justified, as it gives the possibility to ensure the desired properties of A, leading to a large improvement of quality. A flat default model is chosen for all matrix elements when the full matrix method is used in this paper.

5.2.7 Analytic continuation of the self-energy

One of the central quantities of many-body theory is the self-energy Σ. While some of its properties can be understood from $\Sigma(i\omega_n)$, the analytically continued $\Sigma(\omega + i0^+)$ allows a more straightforward interpretation and the calculation of further physical properties.

We will focus our discussion of the AC of the self-energy on DMFT [10], where the self-energy is approximated to be k independent and connects the impurity to the lattice problem. For a given (in general, matrix-valued) Σ, the local (matrix-valued) lattice Green's function is

$$G_{loc}(z) = \sum_k [z - \mu - H_k - \Sigma(z)]^{-1}. \tag{5.28}$$

The matrix H_k is the k-dependent Hamiltonian of the lattice and the inversion has to be understood as matrix inversion. The so-called impurity Weiss field $\mathcal{G}_0(z)$ is obtained from Dyson's equation

$$\mathcal{G}_0^{-1}(z) = G_{loc}^{-1}(z) + \Sigma(z). \tag{5.29}$$

This $\mathcal{G}_0$ is the input for the impurity solver to calculate the self-energy and the interacting impurity Green's function G_{imp}; when inserting Σ back into (5.28), the self-consistency loop can be closed. The DMFT cycle is iterated until convergence is reached, i.e., until $G_{loc} = G_{imp}$. The

self-energy as a function of real frequency is needed within the framework of DMFT to calculate lattice quantities, e.g., $G_{loc}(\omega + i0^+)$ as defined in (5.28), k-resolved spectral functions [148, 149], Fermi surfaces [148] or optical properties of strongly-correlated materials [150].

In contrast to Green's functions, there is no relation equivalent to (5.1) for self-energies and, hence, one needs to find an appropriate method to perform the AC. There are several ways to do so. One could analytically continue both the DMFT Weiss field $\mathcal{G}_0(i\omega_n)$ and the interacting impurity Green's function $G_{imp}(i\omega_n)$ and calculate $\Sigma(\omega + i0^+)$ via the Dyson equation on the real-frequency axis [105]. However, there are two independent analytic continuations involved, and hence, the resulting real-frequency self-energy tends to oscillate heavily and does usually give poor results (see, e.g., Ref. [105]). Another approach is to solve for $\Sigma(\omega + i0^+)$ in the expression for the (analytically continued) $G_{loc}(\omega + i0^+)$ [129, 151, 152].

The most commonly used approach in literature is to continue an auxiliary quantity G_{aux}. Overall, this requires the following five steps: (i) construction of $G_{aux}(i\omega_n)$ from the self-energy $\Sigma(i\omega_n)$, (ii) inverse Fourier transform [3] to $G_{aux}(\tau)$, (iii) AC of $G_{aux}(\tau)$ to $A_{aux}(\omega)$, (iv) construction of $G_{aux}(\omega + i0^+)$ from $A_{aux}(\omega)$ using (5.1), and finally (v) obtaining $\Sigma(\omega + i0^+)$ from $G_{aux}(\omega + i0^+)$.

In the following, we give two possible constructions of $G_{aux}(z)$. First, one can use

$$G_{aux}(z) = \Sigma(z) - \Sigma(i\infty) \tag{5.30}$$

where $\Sigma(i\infty)$ is the constant term of the high-frequency expansion of $\Sigma(i\omega_n)$ [105]. We note here that the resulting quantity G_{aux} is, technically speaking, not a Green's function, since its off-diagonal elements do not have the correct analytic high-frequency behavior (they should fall off like $\sim 1/(\omega_n)^2$, but in (5.30) they fall off like $\sim 1/\omega_n$). Second, there is the inversion method, e.g., used in Ref. [153],

$$G_{aux}(z) = [z + C - \Sigma(z)]^{-1}. \tag{5.31}$$

The constant C is usually set to $C = \Sigma(i\infty) + \mu$ with the chemical potential μ. In this work, we choose to use the inversion method.

5.2.8 Implementation details

We implement a variation of Bryan's MEM algorithm [143] allowing arbitrary expressions for the entropy with the ability to treat the problem in the full matrix formulation. For the minimum search of Q_α we use the Levenberg-Marquardt minimization algorithm [147]. The expressions for the step length and the convergence criterion are chosen as in Ref. [143]. The spectral function is parametrized in singular space as laid out in section 5.2.4 and 5.2.6 and the value of the hyperparameter α is chosen using the piecewise linear fit of $\log \chi^2(\log \alpha)$ (see section 5.2.2). In

[3] In order to avoid spurious oscillations in the inversely Fourier-transformed $G(\tau)$, we fit the high Matsubara frequencies of $\Sigma(i\omega_n)$ with its high-frequency expansion in ω_n ("tail fit") and subtract the resulting tail from G_{aux} before performing the inverse Fourier transform. Then we add the analytic inverse Fourier transform of the tail expansion on the τ axis.

general, the frequency mesh on which $A(\omega)$ is discretized can be freely chosen. In this work, we use a hyperbolic grid, which asymptotically becomes a linear grid for high frequencies but is denser around $\omega = 0$. This allows the use of a smaller overall number of ω points, which speeds up the calculation. However, when calculating the full Green's function from the spectral function according to (5.1), a small broadening ($i0^+$) has to be used. As the hyperbolic grid with a small number of points is not dense enough (we use $N_\omega = 200$ points), this small broadening leads to artefacts, which can be avoided by first interpolating the spectral function on a much finer grid (we use a linear mesh with 10 000 points) and then using $2\Delta\omega$ of the new grid as broadening.

For metallic systems, it is known that the MEM spectra tend to exhibit spurious cusps around the Fermi level [114]. This can be prevented by using the preblur formalism [154], where the so-called "hidden spectral function" is blurred via a convolution with a Gaussian function. Within this algorithm, the hidden spectral function is used to calculate the entropy S, but the misfit χ^2 is evaluated from the blurred spectral function. Also, this blurred spectral function is what is taken in the end as the solution of the problem.

The width b of the Gaussian is another hyperparameter that can be chosen similarly to α, e.g., by searching the maximum of the probability $p(\alpha, b)$ or by locating the characteristic kink in $\log \chi^2(\log \alpha, \log b)$. In accordance to the route employed for determining α, first we determine one value of α for every value of b using the fit method described at the end of section 5.2.2. Then, we take the curves of $\log \chi^2$ at that value of α for the different values of b and fit once more to determine b.

5.3 Two-band model

As a benchmark system for the presented approach, we investigate an artificial particle-hole symmetric two-band model with semicircular density of states. We set the half-band width to $D_1 = 2$ for the first band and to $D_2 = 1$ for the second band. We choose the interaction term in a simple Hubbard-type form $H_{int} = \sum_i U_i n_{i\uparrow} n_{i\downarrow}$ with $U_i/D_i = 3.25$. The chemical potential and the on-site energies are chosen such that both bands are half-filled. For the chosen interaction, the system is a Mott insulator with a spectrum consisting of two distinct Hubbard bands separated by an energy U_i. We treat the problem with DMFT to obtain an interacting impurity Green's function $G_{imp}(\tau)$ and a self-energy $\Sigma(i\omega_n)$ at an inverse temperature of $\beta D_2 = 40$. The simplicity of the problem allows the use of iterated perturbation theory (IPT) [10, 77–80] as impurity solver. The AC of the IPT results are performed using Padé approximants [111, 113]. Because of the noiseless nature of the IPT data, the Padé approximants give reliable results for this specific problem [10]. Additionally we solve our two-band model using the continuous-time hybridization-expansion Quantum Monte Carlo solver (TRIQS/CTHYB) [72, 155], which is based on the TRIQS package [33], and perform the AC with the MEM. We perform $8 \cdot 10^6$ CTHYB measurements. Of course, more measurements would undoubtedly be beneficial for the AC. Nevertheless, we limit ourselves here to emulate more complicated situations where higher-quality data can only

be obtained with a substantial increase in computational effort. Although it would be possible to evaluate the covariance matrix of the Monte Carlo to take into account the correlations of the noise of $G(\tau)$ at different values of τ, for simplicity, we estimate the Monte Carlo noise by manual inspection of the imaginary-time data (5×10^{-4} in our case), and we assume a diagonal covariance matrix with a constant noise for these (and the following) tests. As we determine α by detecting the characteristic kink in $\log \chi^2(\log \alpha)$, the procedure is less sensitive to the given error than, e.g., the classic MEM (see section 5.2.2).

In the following, we will compare the curves obtained by IPT and Padé with those from CTHYB and MEM as two approaches to tackle this problem. The former suffers from a systematic error as it is a perturbative technique, but yields results without statistical error. The latter, on the other hand, is exact in theory, but will always give noisy Green's functions and, thus, uncertainties after AC. In context of multiorbital DMFT calculations away from half-filling, in many cases Quantum Monte Carlo impurity solvers are the only option, making it necessary to analytically continue noisy data.

Some tests benchmarking our implementation of the MEM algorithm and an investigation of the effect of random noise on the data can be found in Appendix 5.8.

In order to model a system with off-diagonal Green's functions and self-energies, we perform a basis transformation for the $G_{imp}(\tau)$ and $\Sigma(i\omega_n)$, which come out as diagonal matrices from the impurity solvers. In this work, we simply use a rotation matrix with an angle $\phi = 0.4\,\mathrm{rad}$, which is representative for the results obtained for other angles.

Figure 5.2 shows the resulting spectral function for the AC of the rotated $G_{imp}(\tau)$. Using a flat default model, the off-diagonal elements of the spectral function feature strong oscillations (dashed green line). This can be explained by the relaxation of the positivity constraint: In general, the AC tends to overfit around $\omega = 0$ and to underfit for large ω, since the kernel is largest for small ω. For metallic spectral functions, these artefacts can be cured as explained in section 5.2.8. For insulating spectral functions, the oscillations around $A = 0$ are suppressed in the diagonal components, because fluctuations to negative values are not possible due to their positivity. In the off-diagonal elements, however, these fluctuations appear. Additionally, for high frequencies, the solution for the off-diagonal elements with flat default model does not tend to zero as in the IPT and Padé solution, but overshoots and goes to negative values. The violation of the particle-hole symmetry is due to the stochastic nature of the Monte Carlo data (it is thus a measure for the quality of the QMC result) and not directly a fault of the MEM (see Appendix 5.8). We refrained from symmetrizing the resulting $G(\tau)$, because in most models one does not have this possibility.

Building the information from the diagonal elements into the default model of the off-diagonal elements (poor man's method), as outlined in section 5.2.5, improves these issues (blue line in figure 5.2). It suppresses oscillations of the off-diagonal elements where the diagonal elements are small, stabilizes a smooth solution, and improves the high-frequency behavior. Nevertheless, care has to be taken as this does not mean that the solution is positive semidefinite, and indeed,

at some frequencies that general property of the spectral function is violated (see the plot of $\det A$ at the bottom of figure 5.2). Therefore, we apply the full matrix formulation (section 5.2.6) to the problem (red lines in figure 5.2). This solves the issues one faces when performing the AC separately for the individual matrix elements. The spurious oscillations of the off-diagonal elements of $A(\omega)$ are efficiently suppressed even for a flat default model and the spectral function matrix is positive semidefinite everywhere.

As a next step, we benchmark the AC of Σ, using the inversion method to construct an auxiliary Green's function (see section 5.2.7) for the off-diagonal model; the obtained $\Sigma(\omega + i0^+)$ is shown in figure 5.3. The separate AC of the individual matrix elements using a flat default model leads to a heavily oscillating self-energy, which is why it is not shown here. But even performing the poor man's matrix method (blue line in figure 5.3) leads to unphysical results. Especially in the regions where the auxiliary spectral function A_{aux} is not positive semidefinite (shaded in gray in figure 5.3), these problems are evident: there are heavy oscillations when the curve overshoots whenever the derivative changes quickly, and for some frequencies even the diagonal elements of the imaginary part of the self-energy become positive. This shows that the poor man's method is not adequate for determining a matrix-valued $\Sigma(\omega + i0^+)$. The full matrix formulation (red line in figure 5.3), however, yields physical solutions just as IPT and Padé; these two solutions are consistent with each other within the limits of the method. Again, the slight deviation from the particle-hole-symmetrized result (dashed purple line) is due to a stochastic violation of that symmetry in the $G(\tau)$ data. This also manifests itself as a spurious peak close to $\omega = 0$ in the off-diagonal element of $\Sigma(\omega + i0^+)$, which can be traced back to a slight mismatch of the position of the poles of $\operatorname{Im}\Sigma(\omega + i0^+)$ (that should be at $\omega = 0$) between different matrix elements. In general models, the particle-hole symmetry is not present and cannot therefore be exploited to improve the result. The real part of $\Sigma(\omega + i0^+)$, which is related to the imaginary part by the Kramers-Kronig relation, also gives plausible results and the two different methods agree very well (not shown). Once $\Sigma(\omega + i0^+)$ has been obtained, other lattice quantities are accessible. However, we do not further discuss this here, but refer the reader to the example in the next section (section 5.4), where we also calculate the local lattice Green's function G_{loc} from $\Sigma(\omega + i0^+)$.

So far, only an insulating solution has been investigated. However, we also put the method to a test in the metallic regime of the model ($U_i/D_i = 1.5$), shown in figure 5.4. As discussed in section 5.2.8, it is necessary to use preblurring to avoid cusps around $\omega = 0$. This is also observed in the generalization of the method to off-diagonal elements. Not only is the preblurred spectral function smoother around $\omega = 0$, but also more details at higher frequencies can be resolved, which can be best seen in the off-diagonal element. In general, in that regime, the results from CTHYB and MEM (employing the preblur technique) and IPT and Padé agree very nicely, similar to what is found for the insulating case.

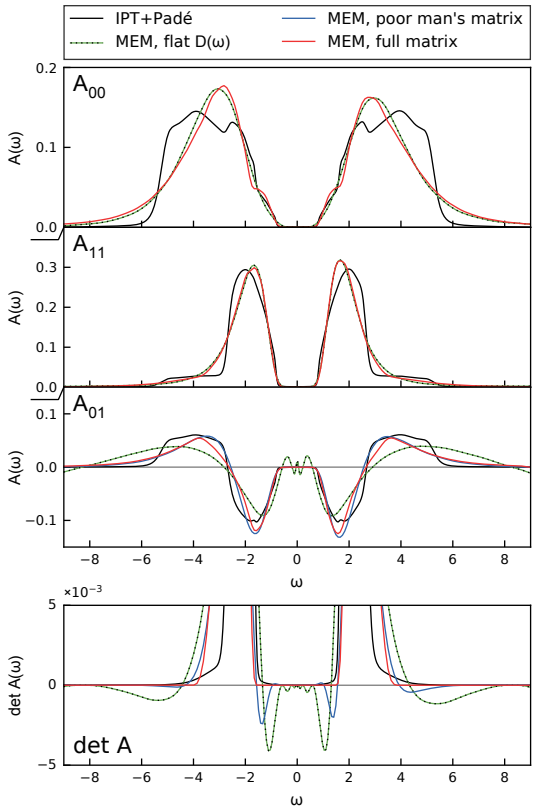

Figure 5.2: Top: Spectral function of the rotated model in the insulating regime. Each subplot represents one matrix element, the two off-diagonal elements A_{01} and A_{10} being the same. The result from IPT and Padé (black) is shown along with the MEM results. For the latter, we compare the continuation treating the matrix elements independently with a flat default model (dashed green) with the poor man's matrix method, i.e., using a default model incorporating the information from the diagonal elements (blue, only for the off-diagonal elements). Furthermore, the result of the matrix formulation (red) that ensures a positive semidefinite, Hermitian spectral function is shown. Bottom: The determinant of the matrix-valued spectral function A as a function of frequency. Wherever $\det A(\omega)$ is negative, the matrix is not positive semidefinite.

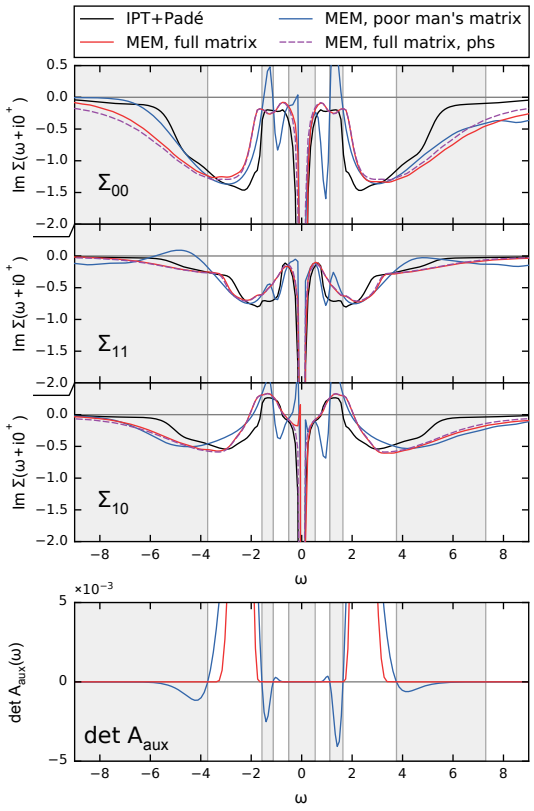

Figure 5.3: Top: Imaginary part of the self-energy $\Sigma(\omega + i0^+)$ for the rotated model obtained with the inversion method. Each subplot represents one matrix element, the two off-diagonal elements Σ_{01} and Σ_{10} being the same. The result from IPT and Padé (black) is compared to the curves obtained with CTHYB and the MEM. The poor man's matrix method (blue) is presented alongside the full matrix method (red). For the latter, also the result where the auxiliary spectral function, A_{aux}, has been particle-hole symmetrized (phs) is shown (dashed purple line). Bottom: The determinant of the matrix-valued auxiliary spectral function A_{aux} as a function of frequency. Wherever $\det A_{aux}(\omega)$ is negative, the matrix is not positive semidefinite. This happens only for the poor man's matrix method. The regions where the corresponding A_{aux} is not positive semidefinite are marked by the gray areas.

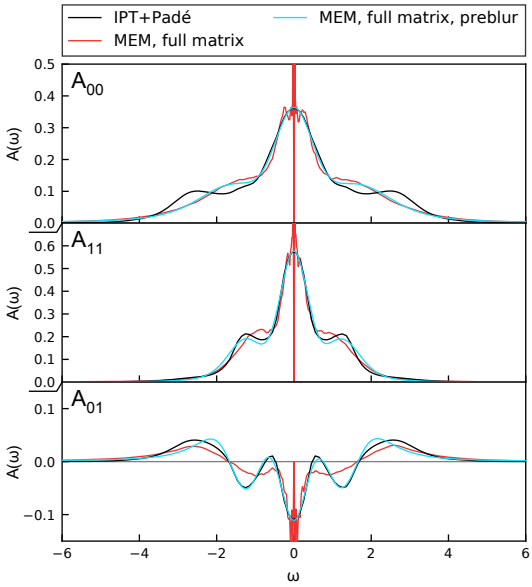

Figure 5.4: Spectral function of the rotated model in the metallic regime. Each subplot represents one matrix element, the two off-diagonal elements A_{01} and A_{10} being the same. The result from IPT and Padé (black) is shown along with the full matrix MEM result. For the latter, we show the result with (cyan) and without (red) using the preblur method.

5.4 Application: $LaTiO_3$

Finally, we apply the matrix formulations presented above in section 5.2.5 and 5.2.6 to $LaTiO_3$, for which we perform a one-shot DFT+DMFT calculation. The transition metal oxide $LaTiO_3$ has a perovskite crystal structure with tilted oxygen octahedra and distorted lanthanum cages. Because of these structural distortions, the material features an off-diagonal hybridization, and thus also an off-diagonal impurity Green's function $G_{imp}(\tau)$. $LaTiO_3$ was already extensively analyzed in literature [156–158], where also the nature of the Mott insulating state was traced back to the tilting and rotation of the oxygen octahedra and the accompanying lifting of the t_{2g} degeneracy.

Here, we do not further elaborate on the physics, but rather use $LaTiO_3$ as a benchmark material to prove the following points: First, we emphasize that the analytic continuation of off-diagonal elements is a problem often encountered in real-materials calculations. Second, the calculations presented here show that the full matrix formalism is feasible for 3×3 matrices. Third, we show that the continuation of the self-energy leads to a local Green's function $G_{loc}(\omega + i0^+)$ which is comparable to the continuation of G_{imp}.

Our calculations were carried out with WIEN2K [24] and the TRIQS/DFTTOOLS package [33, 34, 42, 65]. For the DFT part, we use the crystal structure from Ref. [159], 40000 k points in the full Brillouin zone and employ the standard Perdew-Burke-Ernzerhof (PBE) [23] generalized gradient approximation (GGA) for the exchange-correlation functional. From the DFT Bloch states we construct projective Wannier functions for the t_{2g} subspace of the Ti-3d states in an energy window from -1.0 to 1.2 eV around the Fermi level. In DMFT, we use the Kanamori Hamiltonian with a Coulomb interaction $U = 4.5\,\text{eV}$ and a Hund's coupling $J = 0.65\,\text{eV}$ similar to the values used in Refs. [128, 158]. We solve the impurity model on the imaginary axis with the TRIQS/CTHYB solver [72] at an inverse temperature $\beta = 40\,\text{eV}^{-1}$ and use a total number of $3.2 \cdot 10^7$ measurements. We choose the solver basis such that the density matrix is diagonal. In the case of LaTiO3, this basis has the advantage that all matrix elements of $G_{imp}(\tau)$ are real if the phases are chosen accordingly.

Having obtained $G_{imp}(\tau)$ from the DFT+DMFT calculation, the AC is again performed in two ways: First, with the full matrix formalism for the full Green's function matrix (section 5.2.6) and second, by a separate continuation of the individual elements with the poor man's matrix method introduced in section 5.2.5. Furthermore, we analytically continue $\Sigma(i\omega_n)$ by means of the inversion method (see section 5.2.7). We calculate the local Green's function $G_{loc}(\omega + i0^+)$ with (5.28) and compare it to the direct continuation of the impurity Green's function $G_{imp}(\omega + i0^+)$ in the top graph of figure 5.5.

Within DMFT, the self-consistency condition requires $G_{loc} = G_{imp}$, which is well fulfilled on the Matsubara axis. Nevertheless, the agreement on the real axis shown in figure 5.5 is remarkably good for both the diagonal and the off-diagonal elements, especially when considering the different magnitudes of the individual matrix elements and the fact that the continuation is performed for

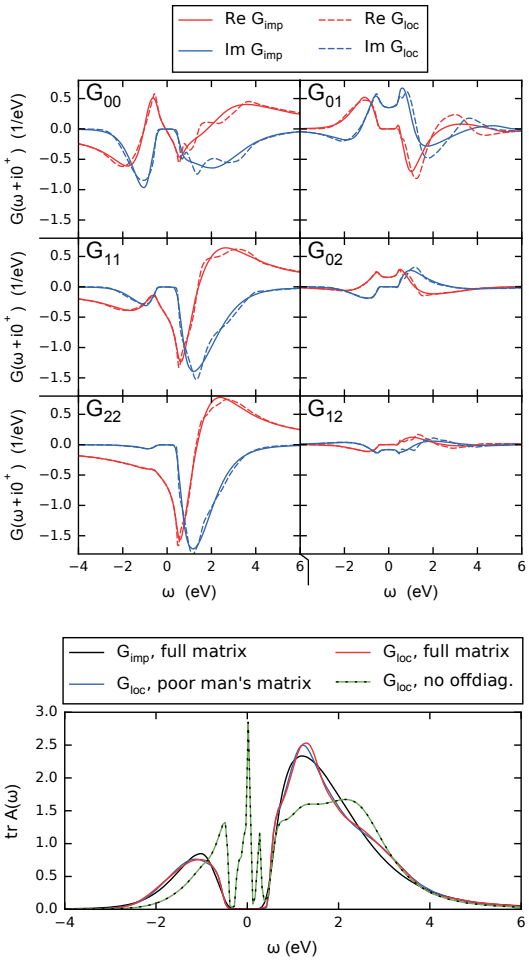

Figure 5.5: Top: Comparison of real (red) and imaginary parts (blue) of the impurity Green's function $G_{imp}(\omega+i0^+)$ (solid lines) and the local lattice Green's function $G_{loc}(\omega+i0^+)$ (dashed lines). The former is obtained by a direct AC, whereas the latter is calculated via (5.28) after the AC of the self-energy. In both cases, the matrix formulation of the MEM code was used. The subplots represent different matrix elements of the Green's function.
Bottom: Total spectral function (i.e., trace over the orbital and spin degrees of freedom) of the Ti-t_{2g} bands from the Green's functions shown above (G_{imp}, black, and G_{loc}, red). For G_{loc}, performing the AC of Σ using the poor man's matrix method is shown as well (blue). Additionally, we show the spectral function of a local Green's function where we have set the off-diagonal elements of the self-energy $\Sigma(i\omega_n)$ to zero before individually continuing its diagonal elements and evaluating G_{loc} from the obtained $\Sigma(\omega + i0^+)$ (dashed green).

different Green's functions, i.e., $G_{imp}(i\omega_n)$ and $G_{aux}(i\omega_n)$. This underlines the capabilities of the presented full matrix method.

Here, we only show the Green's functions obtained with the full matrix formalism; however, it should be emphasized that for $LaTiO_3$ also the poor man's method gives very similar results (see the corresponding spectral function in the bottom graph of figure 5.5). Therefore, here the element-wise continuation with the poor man's method constitutes an efficient alternative to the full matrix method.

Figure 5.5 does not only prove the concept of the AC for the full Green's function, but also shows that the AC of the self-energy via the construction of an auxiliary Green's function is a feasible approach. In contrast, calculating the spectral function from $G_{loc}(\omega + i0^+)$, where we set the off-diagonal elements of the self-energy $\Sigma(i\omega_n)$ to zero (and thus analytically continue only the diagonal elements), does lead to a completely wrong, even metallic, spectral function (see dashed green line in bottom plot of figure 5.5). This clearly shows that the off-diagonal elements must not be neglected at this point of the calculation.

In terms of the gap as well as the overall shape and size of the Hubbard bands, the presented spectra for the Ti-t_{2g} subspace are in good agreement with calculations available in the literature [128, 156, 158].

5.5 Conclusion

In this work, we show how a consistent framework for the analytic continuation of matrix-valued Green's functions can be constructed on a probabilistic footing. In order to enable a treatment of the off-diagonal elements, we use an entropy that allows to relax the non-negativity constraint one has to obey in the usual maximum entropy method. With this generalization, diagonal and off-diagonal elements can, in principle, be treated on a similar footing.

The practical use of this method is studied on two examples, an artificial two-band model and a realistic DFT+DMFT calculation for the insulating compound $LaTiO_3$. First, we propose the poor man's matrix method, where the matrix elements are treated separately. With this scheme, we find satisfactory results for some cases (e.g., for $LaTiO_3$), but also see completely unphysical results in our calculations for the two-band model, since positive semidefiniteness and Hermiticity of the spectral functions cannot be guaranteed.

Only the AC in full matrix formulation cures these problems and produces spectral functions with the correct mathematical properties, such as positive semidefiniteness and Hermiticity. Although being computationally more expensive, it should be employed whenever feasible.

Moreover, these methods for AC introduced here give access to the matrix-valued self-energy on the real-frequency axis, which is indispensable for the study of lattice quantities.

Acknowledgments

The authors want to thank E. Schachinger for fruitful discussions and acknowledge financial support from the Austrian Science Fund, Projects No. Y746, No. P26220, and No. F04103. The computational results presented have been achieved in part using the Vienna Scientific Cluster (VSC). The PYTHON libraries numpy [160] and matplotlib [161] have been used.

5.6 Appendix: Probabilities

5.6.1 Conventional entropy

The framework presented here was developed in the pioneering works by Skilling [134], Gull [142] and Bryan [143], but we will rephrase it here for completeness. In Ref. [134], Skilling used the picture of the monkeys presented in section 5.2.3 to relate the entropy to a prior probability distribution

$$P(\underline{A}|\underline{D},\alpha) = \frac{1}{Z_S}\, e^{\alpha S(\underline{A},\underline{D})}, \qquad (5.32)$$
$$Z_S = \int \frac{d^N A}{\prod_i \sqrt{A_i}}\; e^{\alpha S(\underline{A},\underline{D})}.$$

Note that the measure in (5.32) is not flat, but $\prod_i A_i^{-1/2}$. The metric of the spectral function space is therefore $g_{ij} = \delta_{ij}/A_i$, which is minus the second derivative of the entropy $g_{ij} = -\partial^2 S/\partial A_i \partial A_j$ [134, 162, 163]. The prior distribution is maximized by $A_i = D_i$. When expanding the entropy to second order around the maximum, the variance is therefore αD_i. Thus, the default model determines both the maximum as well as the width of the distribution, as expected from the assumed Poisson process.

Using the likelihood $P(\underline{G}|\underline{A}) = e^{-\chi^2/2}/Z_{\chi^2}$ with $Z_{\chi^2} = \int d^N G\, e^{-\chi^2/2}$, the minimization of Q_α [see (5.6)] can be understood as a maximization of the probability $P(\underline{G},\underline{A}|\alpha,\underline{D}) = e^{-Q_\alpha}/(Z_S Z_{\chi^2})$. This can be used to determine α on a probabilistic footing since marginalizing over $\underline{A}$ gives [142]

$$P(\alpha|\underline{G},\underline{D}) \propto P(\alpha) \int \frac{d^N A}{\prod_i \sqrt{A_i}} e^{-\frac{1}{2}\chi^2 + \alpha S}. \qquad (5.33)$$

The prior $P(\alpha)$ is usually chosen to be Jeffrey's prior $1/\alpha$. The most common way to evaluate the integral (5.33) is to expand the exponent up to second order. The final expression for the probability is [142]

$$P(\alpha|\underline{G},\underline{D}) \propto P(\alpha)\alpha^{\frac{N_\tau}{2}} e^{-Q_\alpha(\underline{A}^*_\alpha)} \left(\det(\Lambda+\alpha)\right)^{-\frac{1}{2}}, \qquad (5.34)$$

where $\underline{A}^*_\alpha$ minimizes Q_α and Λ is a matrix with the elements $\Lambda_{ij} = \frac{1}{2}\sqrt{A_i A_j}\,\partial^2\chi^2/\partial A_i \partial A_j$. The classical MEM by Gull uses the α that maximizes $P(\alpha|\underline{G},\underline{D})$ within this approximation [142],

whereas Bryan suggested to calculate the weighted average $\bar{\underline{A}} = \int d\alpha P(\alpha|\underline{G},\underline{D})\underline{A}_\alpha$ [143]. In most cases, $P(\alpha|\underline{G},\underline{D})$ is sharply peaked, and thus, the classical and the Bryan MEM give very similar results.

5.6.2 Positive-negative entropy

Since $\underline{A}^+$ and $\underline{A}^-$ are assumed to be independent, the entropy is $S(\underline{A}^+,\underline{A}^-) = S(\underline{A}^+) + S(\underline{A}^-)$ and one has to marginalize over both $\underline{A}^+$ and $\underline{A}^-$ in order to find the probability of α:

$$P(\alpha|\underline{G},\underline{D}) \propto P(\alpha) \int \frac{d^N A^+}{\prod_i \sqrt{A_i^+}} \int \frac{d^N A^-}{\prod_i \sqrt{A_i^-}} \times e^{-\frac{1}{2}\chi^2(\underline{A}=\underline{A}^+-\underline{A}^-)+\alpha S(\underline{A}^+,\underline{A}^-)}. \tag{5.35}$$

As in the derivation of $S^\pm$, one can use the fact that χ^2 depends only on the difference $\underline{A}^+ - \underline{A}^-$, so that the remaining degree of freedom can be integrated out. Transforming to $\underline{A} = \underline{A}^+ - \underline{A}^-$ and some auxiliary $\underline{A}' = \underline{A}^+ + \underline{A}^-$, the integral over $\underline{A}'$ is easily evaluated using a second-order expansion of the exponent like in the classical MEM, yielding

$$P(\alpha|\underline{G},\underline{D}) \propto P(\alpha) \int \frac{d^N A}{\prod_i \sqrt[4]{A_i^2 + 4D_i^+ D_i^-}} e^{-\frac{1}{2}\chi^2+\alpha S^\pm}. \tag{5.36}$$

The same form is also obtained in Ref. [139], using a different approach to prove it, with the Skellam distribution of the two monkey hordes as a starting point. Note that either way (5.36) is an approximation. This expression looks similar to the case of positive spectral functions (5.33), but with a different entropy given by (5.14) instead of the ordinary entropy (5.7) and with the measure $\prod_i (A_i^2 + 4D_i^+ D_i^-)^{-1/4}$ instead of $\prod_i A_i^{-1/2}$. Interestingly, the metric is given by the second derivative of the entropy $g_{ij} = -\partial^2 S/\partial A_i \partial A_j$, just as in the ordinary case of non-negative spectral functions. Expanding the exponent of integral (5.36) again to second order, the probability has exactly the same form as in the strictly positive case (5.34), but with a different $Q_\alpha = \frac{1}{2}\chi^2 - \alpha S^\pm$ due to the different entropy and with a different matrix $\Lambda_{ij} = \frac{1}{2}\sqrt[4]{A_i^2 + 4D_i^+ D_i^-}\,\partial^2\chi^2/\partial A_i \partial A_j \sqrt[4]{A_j^2 + 4D_j^+ D_j^-}$ due to the different metric. The prior distribution $e^{\alpha S^\pm(\underline{A})}$ is maximized by $A_i = D_i^+ - D_i^-$. Expanding the entropy up to second order around this maximum gives a variance of $\alpha(D_i^+ + D_i^-)$. Thus, in the usual case $D_i^+ = D_i^- = D_i$, the default model only influences the solution via the width of the distribution, not via the position of the maximum, since this is always at $A_i = 0$.

5.7 Appendix: Stationarity condition in the full matrix formalism

In the full matrix formalism, in practice we formulate the stationarity condition directly in singular space. Let $u_{ab;i}$ be the ith element of the vector $\underline{u}_{ab}$, where a, b are the matrix indices just as in (5.27). Then, the stationarity condition reads $\partial Q_\alpha / \partial u_{ab;i} = 0$ for all a, b, i. Q_α is given by (5.26). Its derivative is

$$\frac{\partial Q_\alpha}{\partial u_{ab;i}} = \sum_{cd;j} \left[\frac{1}{2} \frac{\partial \chi^2(\underline{A}_{cd})}{\partial A_{cd;j}} - \alpha \frac{\partial S(\underline{A}_{cd})}{\partial A_{cd;j}} \right] \frac{\partial A_{cd;j}}{\partial u_{ab;i}}. \tag{5.37}$$

The derivative of the misfit is

$$\frac{\partial \chi^2(\underline{A}_{cd})}{\partial A_{cd;j}} = 2 \sum_l \frac{1}{\sigma^2_{cd;l}} \left(\sum_k K_{lk} A_{cd;k} - G_{cd;l} \right) K_{lj}, \tag{5.38}$$

where the data $G_{cd;l}$ are assumed to have diagonal covariance matrices with diagonal elements $\sigma^2_{cd;l}$ (in practice, a change of basis to diagonalize the covariance matrix is always possible). For the diagonal elements, the derivative of the conventional entropy (5.7) is

$$\frac{\partial S(\underline{A}_{cc})}{\partial A_{cc;j}} = -\log \frac{A_{cc;j}}{D_{cc;j}}, \tag{5.39}$$

for the off-diagonal elements it is given by (5.19). When using $A_{cd;j} = \sum_e B^*_{ec;j} B_{ed;j}$, one obtains

$$\frac{\partial A_{cd;j}}{\partial u_{ab;i}} = \sum_e \frac{\partial B^*_{ec;j}}{\partial u_{ab;i}} B_{ed;j} + B^*_{ec;j} \frac{\partial B_{ed;j}}{\partial u_{ab;i}}. \tag{5.40}$$

As we know that $\partial B_{cd;j} / \partial u_{ab;i}$ is zero unless $a = c$ and $b = d$, the sum over e drops out and one has

$$\frac{\partial A_{cd;j}}{\partial u_{ab;i}} = \delta_{bc} \frac{\partial B^*_{ab;j}}{\partial u_{ab;i}} B_{ad;j} + \delta_{bd} B^*_{ac;j} \frac{\partial B_{ab;j}}{\partial u_{ab;i}}, \tag{5.41}$$

where [using (5.27)]

$$\frac{\partial B_{ab;j}}{\partial u_{ab;i}} = D_{ab;j} V_{ji} \left(e^{\sum_k V_{jk} u_{ab;k}} + e^{-\sum_k V_{jk} u_{ab;k}} \right). \tag{5.42}$$

By plugging these derivatives into (5.37) and setting it to zero, one obtains an expression for the stationarity condition that has to be solved for u.

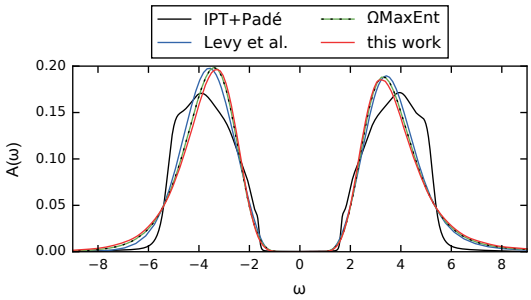

Figure 5.6: Spectral function $A(\omega)$ of the first band of the diagonal two-band model with $U_i/D_i = 3.25$, calculated using Padé approximants for the IPT solution (black) and the MEM for the CTHYB solution. Different MEM codes (Bryan solution from Levy *et al.* [127] in blue, ΩMAXENT [126] in dashed green, and our code in red) were used; a flat default model was employed for all three cases.

5.8 Appendix: Implementation benchmarks

In this appendix, we perform a few tests based on the model introduced in section 5.3 in order to check our implementation of the MEM in general and to demonstrate the effect of noise on the AC.

First, we compare the results for our unrotated diagonal two-band model to those obtained with two freely available MEM codes: a code recently presented by Levy *et al.* [127] and the ΩMAXENT code [126]. The resulting spectral function for the first band is shown in figure 5.6. Within the errors of the method (as discussed, e.g., in Ref. [164]), the three MEM curves are in good agreement. For the second band, the quality of the AC is similar (not shown here). The fact that the MEM solution and the Padé solution do only qualitatively agree is not surprising, as even a small statistical noise of the Monte Carlo data, in contrast to the noiseless IPT solution, notably increases the uncertainty of the AC [164].

In order to assess this influence of statistical noise on the AC, we take the spectral function $A(\omega)$ obtained from IPT and Padé as starting point; then, we calculate the corresponding imaginary-time Green's function $G(\tau)$ by multiplying with the kernel, as in (5.4). In analogy to section 5.3 we rotate the $G(\tau)$ so that it features off-diagonal elements (the rotated IPT and Padé curve is the black curve in figure 5.7). From that $G(\tau)$ (a very small Gaussian random noise with standard deviation 10^{-8} has to be added for the MEM to work) an $A(\omega)$ can be obtained once more using AC, which we perform using our full matrix MEM (blue curve in figure 5.7). As can be clearly seen, for all matrix elements the original curve is well reproduced by the MEM, which is further evidence that our implementation works. However, the curves are smoother than the original data for larger $|\omega|$; this is a well-known tendency of all MEM as the entropy term favors the smoothness of the default model and $G(\tau)$ generally represents the spectral features worse for higher $|\omega|$.

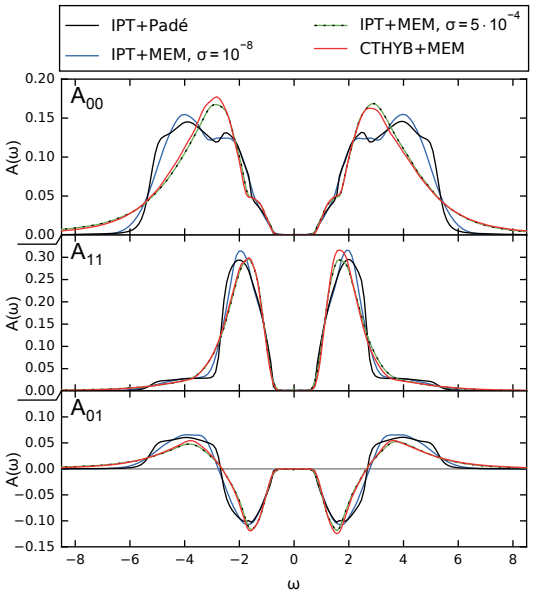

Figure 5.7: Spectral function $A(\omega)$ of the two-band model with $U_i/D_i = 3.25$, calculated using Padé approximants for the IPT solution. Starting from that solution, a $G(\tau)$ was calculated using (5.4); that $G(\tau)$ was then rotated in accordance to section 5.3. The rotated IPT and Padé result is shown as the black curve. Gaussian random noise with a standard deviation of σ was added to that $G(\tau)$, which was then analytically continued using the full matrix MEM (blue curve with $\sigma = 10^{-8}$, dashed green curve for $\sigma = 5 \cdot 10^{-4}$). This is compared to the result from analytically continuing the $G(\tau)$ obtained by solving the same model with CTHYB (red).

We now emulate QMC data by adding bigger random Gaussian noise (with standard deviation 5×10^{-4}) to the $G(\tau)$ from the IPT and Padé $A(\omega)$. The MEM-analytically continued curve from that noisy $G(\tau)$ (dashed green curve in figure 5.7) differs considerably both from the input $A(\omega)$ and from the MEM curve with hardly any noise. One can clearly see how much information is lost already by noise only of the order of 5×10^{-4}. The detailed structure of the Hubbard bands cannot be resolved and it is replaced by just one broad peak for each band (in the diagonal elements). In the A_{00} element, a small shoulder for low $|\omega|$ is observed, reminiscent of a similar feature in the original data.

Finally, we want to compare the results from our artificially noisy Green's function to that of our CTHYB calculation for the same model. The spectral functions (dashed green and red curves in figure 5.7) look very similar, especially the off-diagonal element. As noted before, the CTHYB solution breaks particle-hole symmetry, which can be nicely seen in the different peak heights for positive and negative ω in the diagonal elements (of course, the particular way how this breaking happens will be different from QMC run to QMC run due to the stochastic nature of the method). This can already be seen on the level of $G(\tau)$ (not shown). Thus, we conclude that IPT and Padé gives results compatible to CTHYB and MEM, for this very specific model at hand.

6 $SrIrO_3/SrTiO_3$ heterostructure

Prototypical materials for studying the interplay of electronic correlations and the spin-orbit coupling are either ones with open f-shells or with open $5d$-shells. A classical example for the latter are iridates; the successful explanation of the ground state of Sr_2IrO_4 [165] has sparked the interest in these phenomena in the last decade. Another member of the Ruddlesden-Popper series of iridates [166], the perovskite $SrIrO_3$, can be combined in a heterostructure with $SrTiO_3$. This opens new routes to influence and purposefully modify the properties of the compound.

This chapter consists of original work by the author of this thesis.

6.1 Introduction to the heterostructure

The building blocks of the heterostructure are the perovskite crystals of $SrTiO_3$ and $SrIrO_3$. The former is the most popular substrate in oxide research [167, 168]. It has a lattice constant of 3.901 Å [169], which is relatively similar to the 3.94 Å of $SrIrO_3$ [170]. The latter is not stable in a cubic structure at ambient pressure and room temperature, but can be stabilized as a thin film on suitable substrates [171]. This allows the epitaxial growth of these heterostructures [172].

In heterostructures, it is possible to change the way the compound behaves by adapting one of the following parameters,

- the stacking direction; e.g., along the (001), see figure 6.1, and (111) crystallographic direction. Both have been achieved experimentally [172, 173]. The (111) stacking direction was intensively investigated theoretically, as it might accommodate a topologically non-trivial phase [174, 175].
- the lattice constants and crystal structure. While this is very easy to modify in a theoretical description (within the boundaries on system size coming from the restriction that calculations must yield answers in finite computational time), also experimental routes of changing these parameters, e.g., by varying pressure or temperature, are available.
- a rotation of the IrO_6-octahedra. Again, this is not optional in nature, but theory allows us to study the effects of these lattice modifications.
- the number of $SrTiO_3$ and $SrIrO_3$ layers per unit cell. This parameter has been, for example, studied experimentally in Ref. [172].

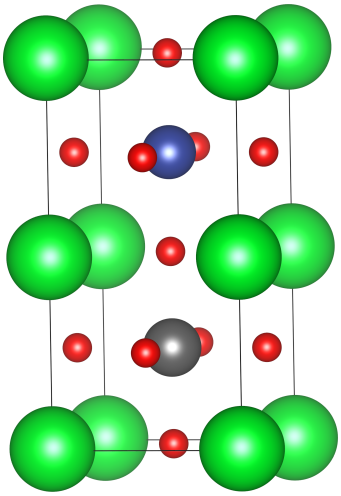

Figure 6.1: Structure of the undistorted (001)-stacked $SrTiO_3$-$SrIrO_3$ heterostructure. Sr atoms are shown in green, O in red, Ti in gray and Ir in blue.

Experimentally, the (001)-stacked heterostructure is found to be metallic when there are many layers of $SrIrO_3$ [172]. Upon reducing the thickness, a metal-insulator transition is observed, with clearly insulating behavior in the resistivity found for one or two layers of $SrIrO_3$. This behavior is linked to a change in the magnetic properties, with a weak in-plane ferromagnetic moment for the thinnest films at temperatures below 100 to 140 K. That moment can be linked to a canted anti-ferromagnetic ordering, which is connected to the rotation of the oxygen cages. Measurements of angle-resolved photoemission spectra yield a gapped electronic structure at the Fermi level accompanied by magnetic ordering for single-layer $SrIrO_3$ [176], confirming its insulating nature. The simultaneous change in the magnetic and electric properties suggests that these two effects are strongly intertwined, with a gap arising when both factors are present [177].

The theoretical description of that compound has focused on first principles calculations based on DFT+U. The enhanced stability of the canted anti-ferromagnetic state compared to a collinear anti-ferromagnetism can be found in this type of calculation [178]. The presence of a gap is only found when both magnetism and Coulomb interactions beyond DFT are taken into account [172, 176, 177]. A three-orbital Hubbard model filled with 5 electrons, which corresponds to the situation found in $SrIrO_3$, with varying spin-orbit coupling strength was investigated on the Bethe lattice; there, a rich phase diagram with metallic, anti-ferromagnetic insulating and excitonic insulating phases is found [100]. While iridates are concluded to be in the anti-ferromagnetic insulating phase, in agreement with the other results, $3d$ or $4d$ materials might exhibit an excitonic phase.

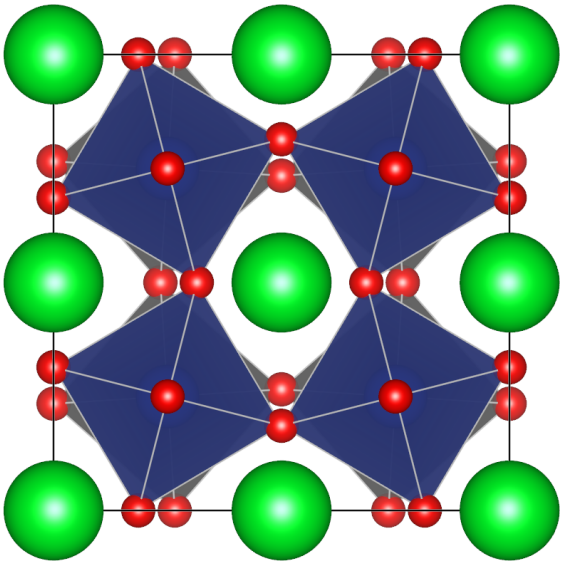

Figure 6.2: Top view of the unit cell of the the $SrTiO_3$-$SrIrO_3$ heterostructure with rotated oxygen cages. The rotation angle of the Ir oxygen cages is 14.4° according to a PBE lattice relaxation. Sr atoms are shown in green, O in red, Ti in gray and Ir in blue. For the transition metal atoms, the polyhedra are drawn in the corresponding color.

6.2 Lattice distortions on the DFT level

As mentioned above, the experimental scenario for creating these heterostructures is epitaxial growth of the $SrIrO_3$ layer(s) on a substrate of $SrTiO_3$; here, we consider just stacking along the (001) crystallographic direction (see figure 6.1). Due to the epitaxial growth, at least the in-plane lattice constant is fixed to the bulk lattice constant of $SrTiO_3$, 3.9 Å (see, e.g., Ref. [172]). This is the cause of lattice distortions with respect to simply stacked perovskites, where the IrO_6 cages rotate around the z-axis to accommodate the Ir atom (see figure 6.2); the fact that the latter requires more space can be seen, e.g., from the experimental values of the lattice constants of the two compounds (see above). In addition to that, also the out-of-plane lattice constant is expected to increase to accommodate the "larger" Ir atom[1].

These effects can be examined by performing a lattice relaxation using DFT. For this, we employ the VASP code [25–29] with the PBE functional [23]. First, we take a supercell where one perovskite unit cell of $SrIrO_3$ is stacked above one unit cell of $SrTiO_3$, but with the same lattice constant. The atom positions are given by symmetry, i.e., the only thing that can change are the lattice constants. The geometry optimization yields an in-plane lattice constant of 3.95 Å and an out-of-plane lattice constant of 7.86 Å (3.86 Å for the Ti layer plus 4.01 Å for the Ir layer). That shows that, when a rotation of the oxygen cages is not possible because of symmetry, there has to be an increase in the in-plane lattice constant and the large out-of-plane lattice constant for

[1] In this context, we define "larger" with respect to the perovskite lattice constant; when looking at covalent radii, the Ir atom (1.41 Å) is smaller than the Ti atom (1.60 Å) [179].

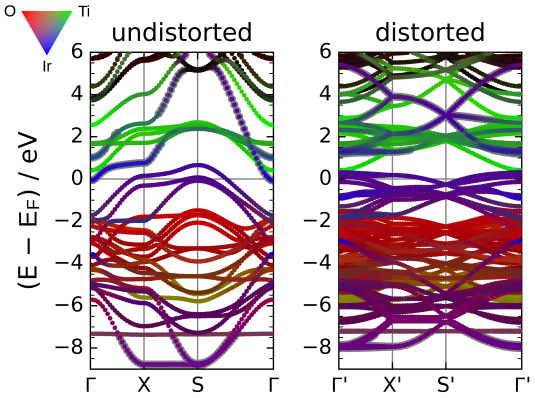

Figure 6.3: Kohn-Sham band structure (calculated in VASP) of the (001)-stacked $SrIrO_3$-$SrTiO_3$ heterostructure, with (right) and without (left) the rotation of the IrO_6 cages. The individual data points of the energies $\varepsilon_{\underline{k},\nu}$ are colored according to the contribution of the different atoms to the wave function $\psi_{\underline{k},\nu}$. Thus, red points are predominantly oxygen states, green points are Ti states and blue points are Ir states. Hybrid states have colors in between, with a color mixture according to the shares of the three different atoms. Black states have mainly Sr character. Ir states that have more e_g character than t_{2g} character are surrounded by a gray circle.

the Ir layer.

When the supercell is increased in size to be 2×2 in the in-plane direction, the oxygen cages are free to turn. Then[2], the in-plane lattice constant reduces to 7.84 Å (which is $2 \cdot 3.92$ Å), which is closer to the $SrTiO_3$ lattice constant. The out-of-plane lattice constant is 7.92 Å (3.81 Å for the Ti layer plus 4.11 Å for the Ir layer), which is yet a further increase. The rotation of the TiO_6 cages comes out as 3.6°, i.e., negligibly small when considering the uncertainty of the method, while the IrO_6 cages are rotated by 14.4°. This does not match well with experiment [172], where the rotation angle is estimated to be 8°, which is especially striking as the lower in-plane lattice constant in experiment should necessitate even larger rotations. Nevertheless, in the spirit of performing ab-initio calculations, a symmetrized[3] version of the optimized structure was used for the following calculations.

The Kohn-Sham band structure of the undistorted system (figure 6.3) exhibits bands with predominant Ir, Ti and O character in the shown energy ranges. At roughly 2 to 6 eV below the Fermi level, oxygen states can be found which hybridize with the transition metal atoms to a certain degree. Above and below the O states, bands with mostly Ir weight are present. The bands around the Fermi level are mostly of Ir *d*-character. The t_{2g} states are partially filled (i.e., the Fermi level is cutting the t_{2g} bands). The e_g states are empty, but start right at the Fermi level. The Ti *d*-shell is unoccupied and at least 1 eV above the Fermi level.

[2] In practice, it is necessary to break the symmetry for the DFT structure optimization.

[3] The symmetries of the crystal are violated by the lattice relaxation on the order of hundredths of Å, which we correct in order to (re)establish the symmetries.

When turning on the distortions, the bands are back-folded into the smaller Brillouin zone that arises due to the use of a supercell. As the (in-plane) lattice constant (per formula unit) is reduced when rotating the oxygen cages, the band width (especially of the Ir states) decreases. Because of the additional hybridization of the d_{xy} and the $d_{x^2-y^2}$ state, the top of the t_{2g} states is slightly pushed down and the bottom of the e_g states is pushed up, opening a gap[4] between these two kinds of states. The Ti bands are hardly affected by the change in structure.

6.3 Basis optimization and reduction

As discussed in the previous chapter, the CTHYB algorithm scales exponentially with the number of orbitals. Furthermore, empirically the sign is worse when taking into account more bands. Therefore, a strategy for reducing the number of orbitals in the correlated subspace is required.

It is possible to directly project only onto a subset of the orbitals around the Fermi level, e.g., the t_{2g} orbitals (see figure 6.3). In addition to that strategy, we here present another way to more systematically reduce the number of orbitals from the full d-shell to a three-band model. This is important whenever the t_{2g} and e_g states are close in energy.

The method itself will be presented using a model inspired by the low-energy physics of the (001)-stacked $SrIrO_3$-$SrTiO_3$ heterostructure.

6.3.1 Model system

The method will be explained using the d-shell of an atom; however, it can be easily generalized to other settings. We start out by constructing projective Wannier functions for the full d-shell, i.e., constructing the orthonormalized projector matrices $P^{\alpha}_{m\nu}(\underline{k})$ from (2.23) in a window $\mathcal{W}_0$; for simplicity we assume the orbital-index m to be a compound index of orbital and spin. It is then possible to calculate the non-interacting $\underline{k}$-integrated spectral function in Wannier space,

$$(A_0)^{\alpha}_{mm'}(\omega) = \frac{i}{2\pi}[(G_{0,loc})^{\alpha}_{mm'}(\omega + i0^+) - (G_{0,loc})^{\alpha *}_{m'm}(\omega + i0^+)], \tag{6.1}$$

where the local, non-interacting Green's function is

$$(G_{0,loc})^{\alpha}_{mm'}(\omega + i0^+) = \sum_{\underline{k},\nu} P^{\alpha}_{m\nu}(\underline{k})(\omega - \varepsilon_{\underline{k},\nu} + \mu + i0^+)^{-1} P^{\alpha *}_{m'\nu}(\underline{k}). \tag{6.2}$$

In the general case, the spectral function has non-zero off-diagonal elements, and there is no single-particle basis that diagonalizes $A_0(\omega)$ at all frequencies. It is Hermitian, i.e., its diagonal elements are real but its off-diagonal elements can be complex-valued.

[4] We want to clarify that, still, the t_{2g} bands are partially filled because the Fermi level is not within the gap that arises.

When constructing the correlated subshell, there are two reasons that justify discarding all "non-correlated" shells. First, for most physical properties of interest, only the low-energy behavior is relevant, i.e., only the states around the chemical potential. Second, the bands around the chemical potential do not hybridize with bands at other energies, therefore there are no fluctuations from the low-energy bands to the other bands[5]. Sometimes, however, one or even both conditions are not fulfilled for a set of sufficiently few bands (that would allow the numerical treatment using, e.g., QMC).

In order to demonstrate the problem, we consider a model Hamiltonian of d-shell atoms on a cubic lattice

$$\begin{aligned} H = &\sum_{\langle ij\rangle}\sum_{m} t\ c^\dagger_{im}c_{jm} + \sum_{\langle ij\rangle}\sum_{\sigma}\left(t'\ c^\dagger_{i,d_{x^2-y^2},\sigma}c_{j,d_{xy},\sigma} + \text{h. c.}\right) \\ &+ \sum_i \sum_{m\in e_g} \mathcal{C}\ c^\dagger_{im}c_{im} + \sum_i \lambda\ (\underline{L}\cdot\underline{S})_{mm'}c^\dagger_{im}c_{im'}, \end{aligned} \tag{6.3}$$

where the sum $\langle ij\rangle$ is carried out over neighboring sites, the index m is a compound index of orbital and spin, and σ is an explicit spin index. The first term is the diagonal hopping term in the nearest-neighbor approximation, the second term is an off-diagonal hopping (a hybridization) between the $d_{x^2-y^2}$ and d_{xy} orbitals, the third term is the crystal-field term and the fourth term is the SOC.

For the parameters t, t', $\mathcal{C}$ and λ, three different cases are studied:

(a) The model with hopping only, i.e., $t=-1$, $t'=0$, $\mathcal{C}=0$, and $\lambda=0$.

(b) The model with crystal-field splitting, i.e., $t=-1$, $t'=0$, $\mathcal{C}=4$, and $\lambda=0$.

(c) The model with spin-orbit coupling, crystal-field splitting and a hybridization[6] between $d_{x^2-y^2}$ and d_{xy}, i.e., $t=-1$, $t'=-2i$, $\mathcal{C}=4$, and $\lambda=0.4$. Note that, compared to "real" systems, t' and λ are rather high.

Figure 6.4 shows the non-interacting spectral function of that model. At first, in case (a), only the hopping term is taken into account with a diagonal hopping, which leads to the five d-orbitals being degenerate. The inclusion of a crystal-field splitting [case (b)], as found, e.g., in transition metal oxides where the transition metal atom feels an octahedral field from the neighboring oxygens, raises the energy of the e_g orbitals. Including SOC on top of that (not shown) does not qualitatively change that picture, where again the diagonal elements of the spectral function are the same for all t_{2g} states and the same for all e_g states (the energy-splitting due to the SOC

[5] There might still be fluctuations mediated by the interaction; if they become important, it is still not possible to leave out bands that do not hybridize with the low-energy manifold.

[6] When using the definition of cubic harmonics in (3.33), the resulting wave functions of the cubic d-orbitals in real space, $d_\bullet(\underline{r}) = \langle r|d_\bullet\rangle$, are not purely real [as discussed in the context of (3.33)]. Rather, d_{z^2}, d_{x^2} and d_{xz} are real and d_{xy} and d_{yz} are imaginary. Therefore a "normal" hopping element between one of the real and one of the imaginary orbitals has a factor i. Spin-orbit and magnetic-field induced hopping elements, which are usually (i.e., in bases with real basis wave functions) associated with imaginary or complex hoppings, would be real when coupling a real to an imaginary orbital.

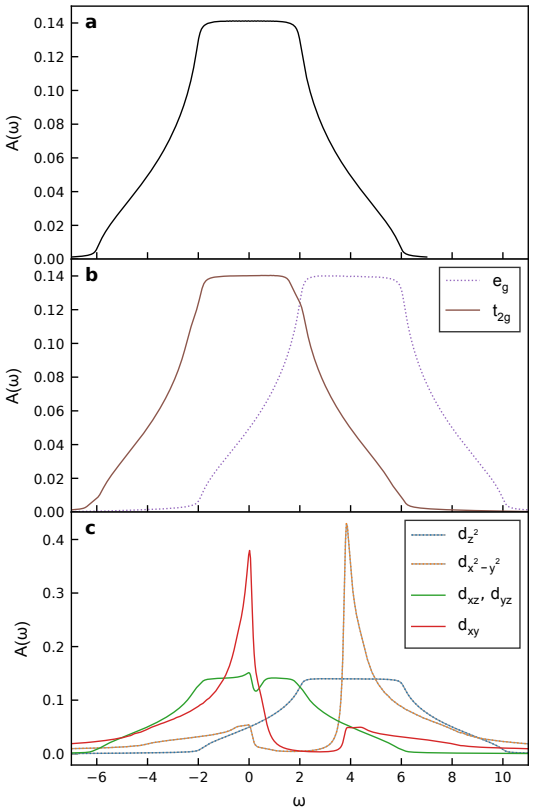

Figure 6.4: Orbital-resolved (non-interacting) spectral function $A(\omega)$ (only the diagonal elements are plotted) of the model (6.3). The subfigures (a)-(c) correspond to the parameter sets (a)-(c) of the model (see text). Due to the hybridization, additional t_{2g} weight at high energies and additional e_g weight at low energies appears.

affects the eigenenergies, but not the diagonal elements in the cubic basis). However, as soon as the SOC is introduced, the spectral function features off-diagonal elements (not shown), even between different spins. Finally, a hybridization between the $d_{x^2-y^2}$ and the d_{xy} orbital (i.e., an off-diagonal hopping term between the two) is introduced [case (c)]. In a real crystal, this could be due to, e.g., distortions of the oxygen cages in a perovskite transition metal oxide. This gives rise to e_g weight in an energy range where before only t_{2g} weight was present and vice versa. At the chemical potential at $\omega = 0$, all orbitals have some spectral weight, but the e_g weight is overall much smaller than the t_{2g} weight.

When looking at the spectral-function matrix in figure 6.5, sizeable off-diagonal elements can be found. The most prominent off-diagonal element is between the same-spin $d_{x^2-y^2}$ and d_{xy} orbital, which can be traced back to the hybridization term between the two. There are also significant off-diagonals of the $d_{x^2-y^2}$ and d_{xy} orbitals with the different-spin d_{xz} and d_{yz} orbitals due to the SOC.

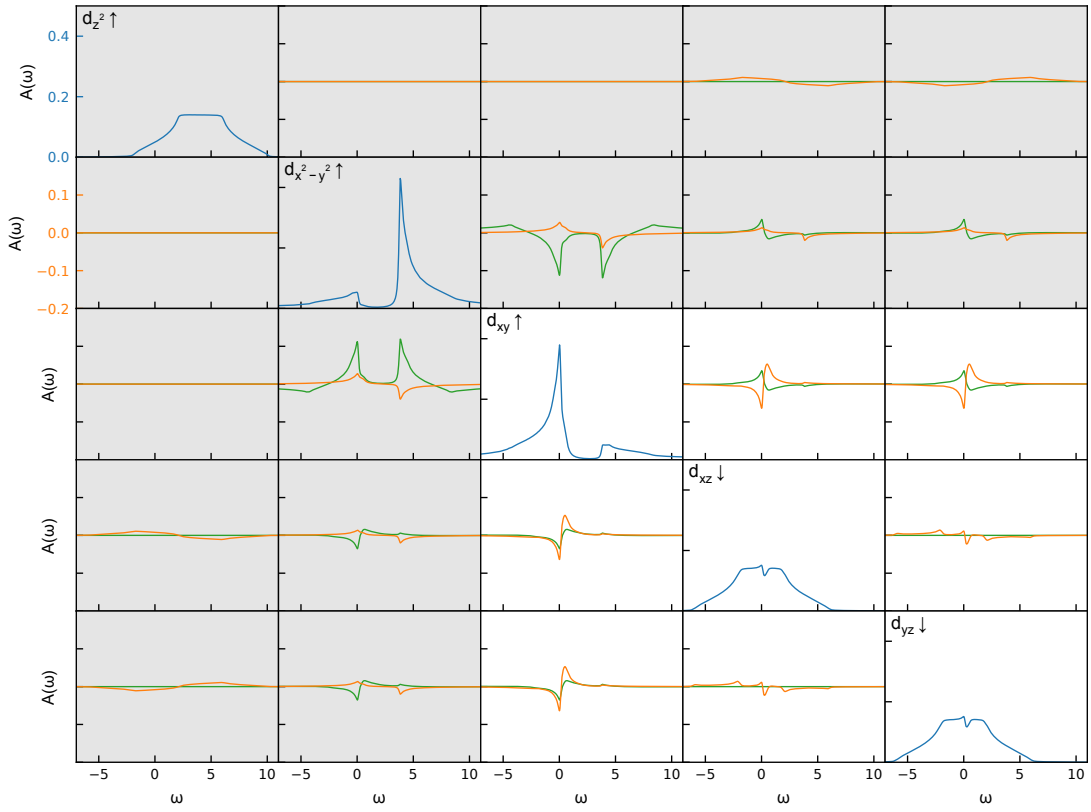

Figure 6.5: Orbital-resolved (non-interacting) spectral function $A(\omega)$ of the model (6.3) with parameters as in figure 6.4 (c). Only half the orbitals are shown, because the spectral-function matrix has a block-diagonal structure with two blocks. The second block, which is not shown, is the same as the first block up to a complex conjugation (where we need to take into account that some basis functions are imaginary). All the diagonal elements are shown on the same scale as indicated by the blue axis on the top left, and all the off-diagonal elements are shown on a different scale shown in orange. The real part of the off-diagonal elements is plotted in orange, the imaginary part in green. The e_g orbitals, which feature less spectral weight around the chemical potential, and their off-diagonal elements are shown with a gray background.

This means that in the case considered here, both conditions for discarding the e_g states to treat only a three-band t_{2g} model are violated.

6.3.2 Basis optimization procedure

The goal of this procedure is to decouple the states around the chemical potential from the other states; therefore we search a basis where the off-diagonal elements between the states around μ and the other states are minimal (these would be the off-diagonal elements marked in gray in figure 6.5). That basis is characterized by the unitary matrix T that transforms from the basis of cubic harmonics to the new basis.

Using the observation that the spectral function usually has two related blocks (either the up and down spin or the two blocks of SOC, where the first block consists of $\{d^{\uparrow}_{z^2}, d^{\uparrow}_{x^2-y^2}, d^{\uparrow}_{xy}, d^{\downarrow}_{xz}, d^{\downarrow}_{yz}\}$ and the second block of the same orbitals with flipped spin), in order to keep the parameter space smaller, the matrix T is constructed as a block matrix featuring two submatrices. The second submatrix is either chosen to be identical to the first submatrix or its complex conjugate (the latter is a sensible choice when the off-diagonal elements are due to spin-orbit coupling). The actual choice of blocks depends on the problem at hand.

In order to classify the M orbitals into a set $\mathcal{B}_1$ of M' orbitals that shall be kept and a set $\mathcal{B}_2$ of $M - M'$ orbitals that shall be removed, we define an energy window $\mathcal{W}_1$ around the Fermi level where the states that shall be kept are dominant, and a window $\mathcal{W}_2$ where the states that will be discarded are prominent. In the model system presented above, $\mathcal{W}_1$ could be $[-7, 2]$ and $\mathcal{W}_2$ could be $[2, 11]$. We consider the integral

$$I^x_m = \int_{\mathcal{W}_x} d\omega \, (TA_0T^\dagger)_{mm}(\omega); \tag{6.4}$$

the M' states with the highest values of I^1_m/I^2_m in the current basis are kept.

A reasonable choice for the cost function of a given transformation matrix T is

$$C(T) = \sum_{m\in\mathcal{B}_1} \sum_{m'\in\mathcal{B}_2} \int_{\mathcal{W}_1\cup\mathcal{W}_2} d\omega \, |(TA_0T^\dagger)_{mm'}(\omega)|. \tag{6.5}$$

The task of the program searching for the best unitary transformation T is to find the minimum of $C(T)$ using a suitable algorithm. We employed Powell's conjugate direction method [180] as implemented in scipy [181, 182].

For an optimization algorithm, the cost function has to be optimized as a function of certain parameters; it is, therefore, necessary to parametrize the unitary matrix T. We take as (real) parameters the real and imaginary parts of the elements of a Hermitian matrix H and construct the unitary matrix as $T = \exp iH$, where the matrix exponential is used.

Let Q be the operator that cuts out the states that are kept from the matrix T. Then, within

the projection formalism used to construct the correlated subspace from the ab-initio calculation (see section 2.3.1), this extra rotation can be understood as an additional non-unitary (e.g., 6×10) transformation matrix Q acting on the projectors P. This means that the projection from the Bloch basis to the reduced subspace is given by projectors $P' = QP$, which amounts to a redefinition of the projectors in the new basis. Similar to P, we have $QQ^\dagger = 1$ but $Q^\dagger Q \neq 1$. The same property also holds for P'.

This approach can be regarded as a systematic way to consistently construct a three-band low-energy model from the full d-shell. It is preferable to outright neglecting, e.g., e_g-like bands because it allows to better separate the considered and the neglected orbitals.

6.3.3 Example and visualization

Now, we want to examine the effect of the basis optimization using the model (6.3), case (c), introduced in section 6.3.1. We reduce the basis of 2×5 orbitals to 2×3 orbitals using the windows $\mathcal{W}_1 = [-7, 2]$ and $\mathcal{W}_2 = [2, 11]$. It turns out that it does not matter whether the matrix T is constructed as block-diagonal in spin-space or in the spin-orbit operator blocks because the relevant off-diagonal elements between the different-spin states in the SOC blocks come out as zero in the optimization. As the second block of the spectral function is the complex conjugate (taking into account that some basis functions are imaginary) of the first block, also for the transformation matrix the entry of the second block is chosen as the complex conjugate of the first block (again taking into account that some basis functions are imaginary).

The cost function landscape is very shallow, i.e., there are many different bases with the same associated cost; therefore, starting from different initial bases, different end results with different costs are found. Empiric tests show that starting from the identity transformation matrix leads to the lowest final cost[7]. Even if the optimization algorithm is not guaranteed to find the global optimum, starting from the identity matrix means searching for a local optimum in the vicinity of the original basis, which is sensible.

The optimized basis is given by

$$\begin{pmatrix} |\psi_1^\uparrow\rangle \\ |\psi_2^\uparrow\rangle \\ |\psi_3^\uparrow\rangle \\ |\psi_4^\downarrow\rangle \\ |\psi_5^\downarrow\rangle \end{pmatrix} = \begin{pmatrix} e^{-0.22\pi i} & 0 & 0 & 0 & 0 \\ 0 & 0.96 \cdot e^{\ 0.25\pi i} & 0.29 \cdot e^{\ 0.84\pi i} & 0 & 0 \\ 0 & 0.29 \cdot e^{-0.36\pi i} & 0.96 \cdot e^{-0.76\pi i} & 0 & 0 \\ 0 & 0 & 0 & 0.71 \cdot e^{-0.21\pi i} & 0.71 \cdot e^{0.79\pi i} \\ 0 & 0 & 0 & 0.71 \cdot e^{\ 0.95\pi i} & 0.71 \cdot e^{0.95\pi i} \end{pmatrix}^* \begin{pmatrix} |d_{z^2}^\uparrow\rangle \\ |d_{x^2-y^2}^\uparrow\rangle \\ |d_{xy}^\uparrow\rangle \\ |d_{xz}^\downarrow\rangle \\ |d_{yz}^\downarrow\rangle \end{pmatrix}, \tag{6.6}$$

where in accordance to (2.47), $|\psi_m\rangle = \sum_{m'} T^*_{mm'} |d_{m'}\rangle$. For the other (spin-flipped) block, the transformation matrix is conjugated and the sign of the columns and lines featuring the imaginary basis functions is inverted. The first three orbitals are mostly phase-shifted versions of the

[7] Also, starting from the matrix that diagonalizes the spectral function at any frequency leads to the same final cost.

cubic-harmonic wave functions (in fact, the transformation matrix shows that the $d_{x^2-y^2}$ and the d_{xy} orbitals are getting mixed to a certain degree). The last two are a linear combination of two d_{xz} and d_{yz}, where each of the coefficients has the absolute value $1/\sqrt{2}$ (there is an additional phase shift). Not quite surprisingly, the resulting orbitals look like a phase-shifted version of the $Y_2^{\pm 1}$-orbitals. The reason for the existence of the strange phases and transformations limited to the pseudo-t_{2g} subspace are that, using just a transformation in the orbital space, also off-diagonal elements between spin channels are minimized.

In figure 6.6, the transformed spectral function in the optimized basis is shown.

In order to find out whether the resulting orbitals are physically meaningful, we apply the transformation matrix to atomic hydrogen-like d-orbitals (see figure 6.7). The orbitals that will be neglected are ψ_1 and ψ_2. The former is a phase-shifted version of the d_{z^2} orbital. The orbitals ψ_2 and ψ_3 are linear combinations of the d_{xy} and $d_{x^2-y^2}$ orbitals, which mix in the first place due to the lattice distortions. Orbitals ψ_4 and ψ_5 are linear combinations of d_{xz} and d_{yz} that yield a phase-shifted version of the $Y_2^{\pm 1}$ orbitals. While it might be surprising that a transformation within the t_{2g}-like states is necessary to minimize the off-diagonals, this becomes clear once one realizes that using just a transformation in the orbital space, also off-diagonal elements between pseudo-spin channels are minimized. All in all, the rotated orbitals still look sensible.

While the off-diagonal elements stemming only from the spin-orbit coupling (these are the ones mixing different spin channels) can be reduced by means of that basis optimization, the hybridization between the $d_{x^2-y^2}$ and the d_{xy} orbital cannot be eliminated. The spin-orbit coupling is a local term (this is exact in this model and approximately true in real materials); diagonalizing the local non-interacting Hamiltonian eliminates its off-diagonal elements, but introduces new off-diagonal elements if the hybridization function is not diagonal in that eigenbasis[8]. By performing our optimization procedure, it is possible to find a basis where the off-diagonal elements between ψ_1 and ψ_5 as well as between ψ_2 and ψ_4 vanish (this can also be seen in Figure 6.8). This means that, in total, the pseudo-e_g and pseudo-t_{2g} subspaces are further decoupled. Nevertheless, some off-diagonal elements remain that we cannot get rid of. Similarly, directly adding a large hybridization (e.g., between $d_{x^2-y^2}$ and d_{xy}) produces large frequency-dependent off-diagonal terms in the hybridization function. A basis transformation will reduce their size at some frequency and (in general) increase it at other frequencies; therefore, it is also not possible to transform these elements away completely.

Note that this is not a peculiarity of this basis optimization method, but a general statement. Also other alternatives, e.g., directly projecting the KS band structure on the t_{2g} subshell alone, suffer from that problem. The only possible remedy is the use of an impurity solver that can handle the full d-shell with off-diagonal elements, which to date is only possible for approximate solvers or with substantially (if not prohibitively) increased computational demand.

[8] In particular, if the hybridization function of all the orbitals is degenerate and diagonal, it is diagonal in any basis.

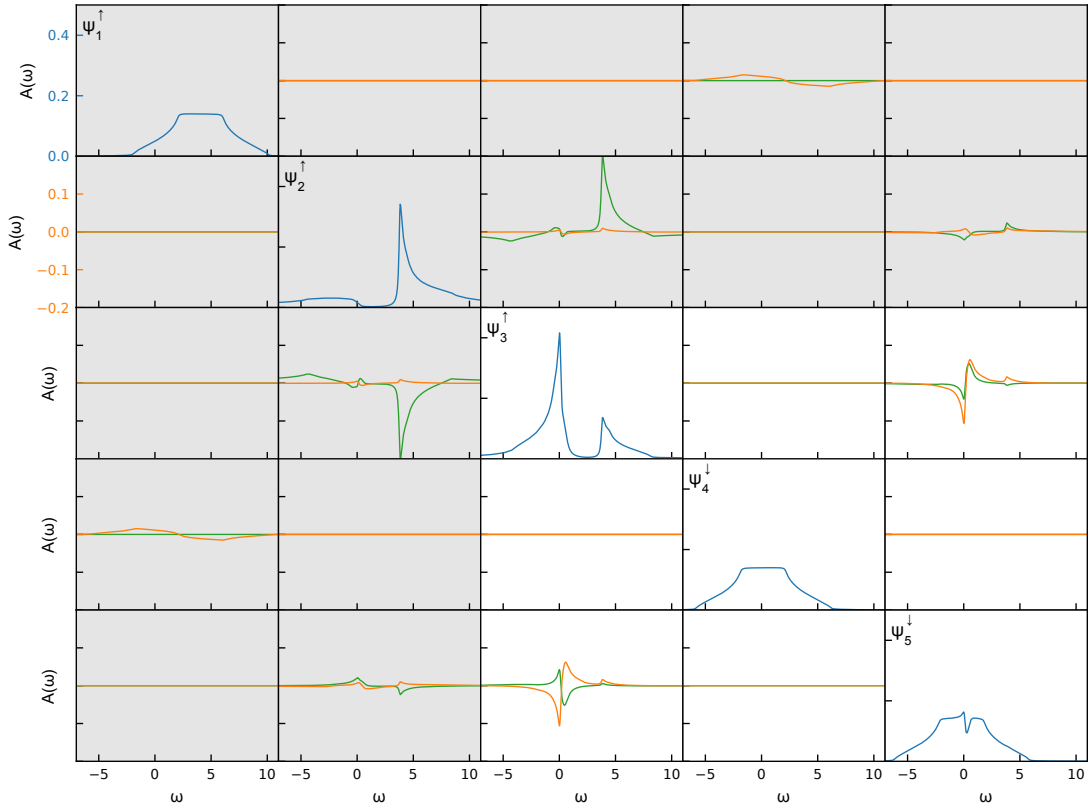

Figure 6.6: Orbital-resolved (non-interacting) spectral function $A(\omega)$ of the model (6.3) with parameters as in figure 6.4 (c), transformed using the basis rotation matrix T from (6.6). Only half the orbitals are shown, because the spectral-function matrix has a block-diagonal structure with two blocks. The second block, which is not shown, is the same as the first block up to a complex conjugation (where we need to take into account that some basis functions are imaginary). All the diagonal elements are shown on the same scale as indicated by the blue axis on the top left, and all the off-diagonal elements are shown on a different scale shown in orange. The real part of the off-diagonal elements is plotted in orange, the imaginary part in green. The orbitals which feature less spectral weight around the chemical potential and their off-diagonal elements are shown with a gray background.

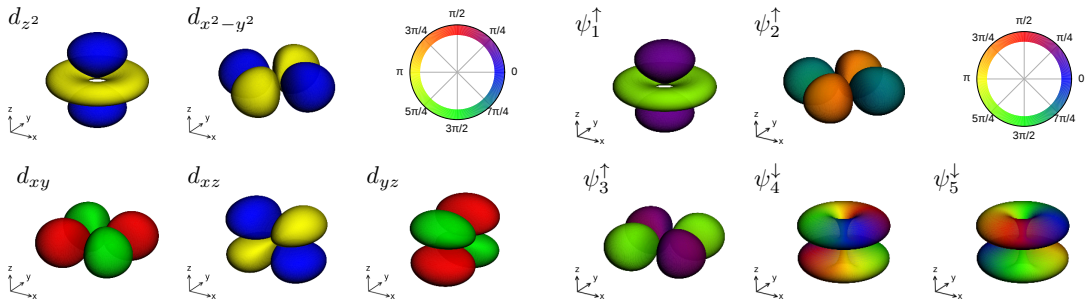

Figure 6.7: Real-space plot of the hydrogen wave functions (for $n = 3$). Isosurface for the electron density, colored according to the phase of the wave function (see legend in the upper right corner). Left: in the cubic harmonic basis. Right: in the optimized basis from (6.6).

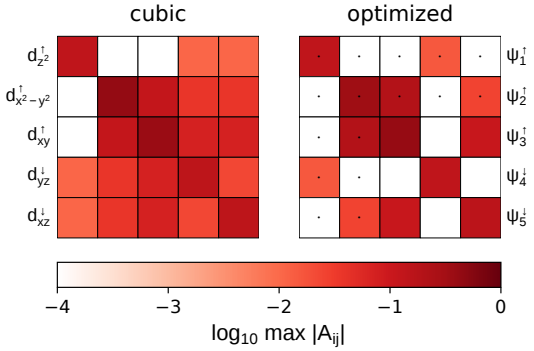

Figure 6.8: Maximum absolute value of the matrix elements of the non-interacting spectral function $A(\omega)$ of the model (6.3) with parameters of case (c). On the left, the matrix in the cubic harmonic basis is shown, on the right it is transformed using the basis rotation matrix T from (6.6). Only half the orbitals are shown, because the spectral-function matrix has a block-diagonal structure with two blocks. The second block, which is not shown, is the same as the first block up to a complex conjugation (where we need to take into account that some basis functions are imaginary). The orbitals which feature less spectral weight around the chemical potential and their off-diagonal elements are marked with a dot.

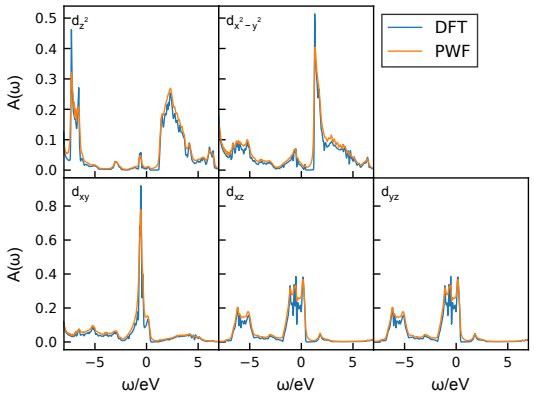

Figure 6.9: Comparison of the diagonal elements of the non-interacting spectral function of the (001)-stacked $SrIrO_3$-$SrTiO_3$ heterostructure with distortions, once calculated directly from DFT (blue curve) and once from the projected non-interacting Green's function (orange curve).

6.3.4 Application to the heterostructure

We construct PWF in a large energy window from $-8.5\,\mathrm{eV}$ to $7\,\mathrm{eV}$ around the Fermi level. The projected DFT density of states is well reproduced by the spectral function calculated from the PWF (see figure 6.9). The slight deviations stem from the different integration schemes for performing the Brillouin zone integration, which is done using the tetrahedron method [183] in Wien2k and using broadened Lorentzian peaks in TRIQS/DFTTools.

When the basis is optimized, one obtains the transformation matrix

$$\begin{pmatrix} |\psi_1^\uparrow\rangle \\ |\psi_2^\uparrow\rangle \\ |\psi_3^\uparrow\rangle \\ |\psi_4^\downarrow\rangle \\ |\psi_5^\downarrow\rangle \end{pmatrix} = \begin{pmatrix} e^{\,0.29\pi i} & 0 & 0 & 0 & 0 \\ 0 & 0.97\cdot e^{-0.33\pi i} & 0.23\cdot e^{-0.83\pi i} & 0 & 0 \\ 0 & 0.23\cdot e^{-0.83\pi i} & 0.97\cdot e^{-0.33\pi i} & 0 & 0 \\ 0 & 0 & 0 & 0.71\cdot e^{\,0.95\pi i} & 0.71\cdot e^{-0.05\pi i} \\ 0 & 0 & 0 & 0.71\cdot e^{-0.09\pi i} & 0.71\cdot e^{-0.09\pi i} \end{pmatrix}^* \begin{pmatrix} |d_{z^2}^\uparrow\rangle \\ |d_{x^2-y^2}^\uparrow\rangle \\ |d_{xy}^\uparrow\rangle \\ |d_{xz}^\downarrow\rangle \\ |d_{yz}^\downarrow\rangle \end{pmatrix}. \tag{6.7}$$

This matrix is very close to the one optimizing the basis for the example in (6.6), which shows that the basic assumptions made there (a local spin-orbit term and an off-diagonal hybridization between $d_{x^2-y^2}$ and d_{xy}) are what models the physics here. It is, thus, not surprising that the change in maximum absolute value of the off-diagonal elements (figure 6.10) is very similar to the corresponding plot of the model, figure 6.8.

Considering the remaining off-diagonal elements, the same considerations that were discussed above hold also here.

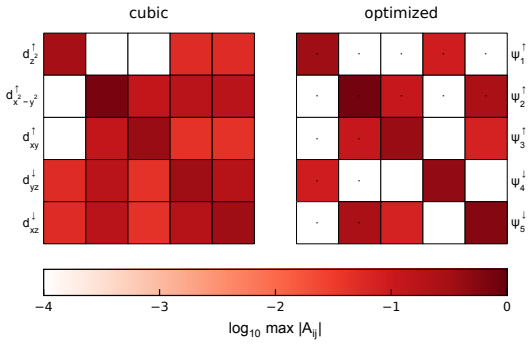

Figure 6.10: Maximum absolute value of the matrix elements of the non-interacting spectral function $A(\omega)$ of the (001)-stacked $SrIrO_3$-$SrTiO_3$ heterostructure with distortions. On the left, the matrix in the cubic harmonic basis is shown, on the right it is transformed using the basis rotation matrix T from (6.7). Only half the orbitals are shown, because the spectral-function matrix has a block-diagonal structure with two blocks. The second block, which is not shown, is the same as the first block up to a complex conjugation (where we need to take into account that some basis functions are imaginary). The orbitals which feature less spectral weight around the chemical potential and their off-diagonal elements are marked with a dot.

6.4 Correlations in DMFT

In order to treat correlations beyond DFT, a local interaction Hamiltonian is added. The interaction parameters are set to $U = 4.5\,\mathrm{eV}$ and $J = 0.8\,\mathrm{eV}$, which can be found in the literature for Ir large-window projectors in undistorted Sr_2IrO_4 [184], calculated based on self-consistent GW [61]. The similarity of the members of the Ruddlesden-Popper series suggests that the interaction parameters are also applicable to the present compound, especially when using large projection windows.

The pseudo-e_g states $\psi_1^{\uparrow}$ and $\psi_2^{\uparrow}$ (and the corresponding orbitals from the second block) are neglected in the optimized basis (6.7). The same basis transformation and reduction is also applied to the Slater interaction Hamiltonian. Using the optimized, reduced basis, the problem is treated in DMFT. Unfortunately, one runs into the the fermionic sign in the CTHYB solver (see chapter 4). As discussed in section 4.4, the sign can be improved by performing a basis transformation[9] of the creation and annihilation operators; however, in most bases, the sign is still prohibitively small. In particular, diagonalizing the local non-interacting Hamiltonian does not constitute a feasible strategy here, yielding average signs on the order of $< 10^{-3}$ after the first iteration. A working strategy[10] is to diagonalize the lowest order tail expansion of the hybridization function $\Delta(i\omega_n)$, i.e., the matrix-valued expansion coefficient of $1/\omega_n$, in every

[9] We want to clarify that this is an additional basis transformation in the reduced space of orbitals that is independent of the basis optimization. A change of basis without neglecting anything is not an approximation as it does not change the physics of the problem.

[10] Still, the resulting sign is between 0.06 and 0.12, which is far from ideal, but can yield sensible results with a highly increased computational effort.

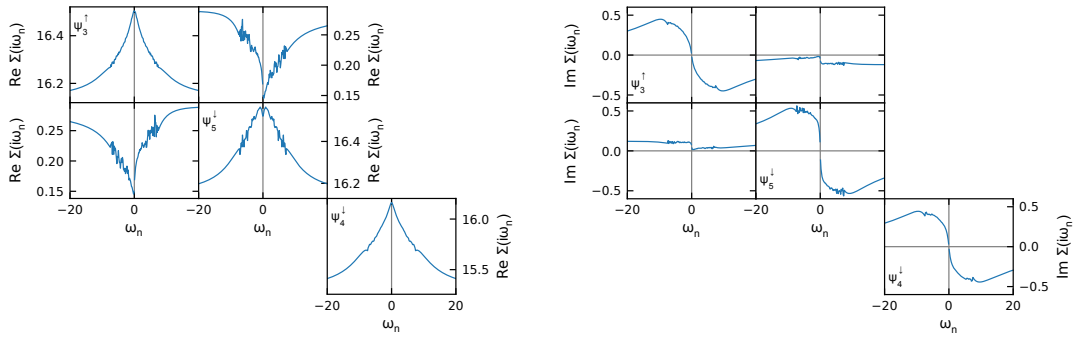

Figure 6.11: Real part (left) and imaginary part (right) of $\Sigma(i\omega_n)$ of the (001)-stacked $SrIrO_3$-$SrTiO_3$ heterostructure with distortions in the optimized basis. As before, just one of the two subblocks is shown. That subblock can be further decomposed into one 2×2 block (containing $\psi_3^\uparrow$ and $\psi_5^\downarrow$) and one 1×1 block (the $\psi_4^\downarrow$ orbital).

iteration. Other strategies, e.g., diagonalizing $\Delta(\tau = 0)$ might also be worth exploring.

The converged DMFT Matsubara self-energy is shown in figure 6.11. As seen from figure 6.10, each of the two related subblocks can be split further into two blocks. The diagonal elements have a symmetric real part and an anti-symmetric imaginary part, which is a consequence of (4.11). For off-diagonal elements, this is not the case, but (4.11) still holds.

Interestingly, the different orbitals show a different sampling quality in the Monte Carlo procedure. Off-diagonal elements tend to be worse sampled than diagonal elements, a trend that can be seen also in this calculation. The diagonal element of ψ_5 has the worst quality of all the diagonal elements; incidentally, this is also the most correlated orbital (see below). To mitigate the noise, for that $\Sigma(i\omega_n)$, the tail was fitted starting at $\omega_{n=47} = 7.46\,\mathrm{eV}$ and $\omega_{n=-48} = -7.46\,\mathrm{eV}$ (for $\beta = 40\,\mathrm{eV}^{-1}$).

From the derivative of $\Sigma(i\omega_n)$ at $\omega_n \to 0$, the quasi-particle weight Z can be estimated [82],

$$Z = \left(1 - \left.\frac{\partial \operatorname{Im} \Sigma(i\omega_n)}{\partial \omega_n}\right|_{\omega_n \to 0}\right)^{-1}. \tag{6.8}$$

At high temperatures (room temperature, which corresponds to $\beta = 40\,\mathrm{eV}^{-1}$, definitely counts as high in that aspect), it is not always possible to get trustworthy values of Z. The estimated values, stemming from a polynomial fit of 4^{th} degree through the first 6 Matsubara points, are 0.75 for ψ_3, 0.69 for ψ_4, and 0.43 for ψ_5. As $Z = 1$ is the uncorrelated state and $Z = 0$ marks the Mott transition, this shows that the paramagnetic heterostructure is quite far from a Mott transition and can be classified as a moderately correlated metal (for comparison, the prototypical correlated metal $SrVO_3$ has $Z \approx 0.5$ [185]).

This can also be seen from the total spectral function in figure 6.12, which clearly is the spectral function of a metal. As suggested by the quasi-particle weights, the band width of the peak at

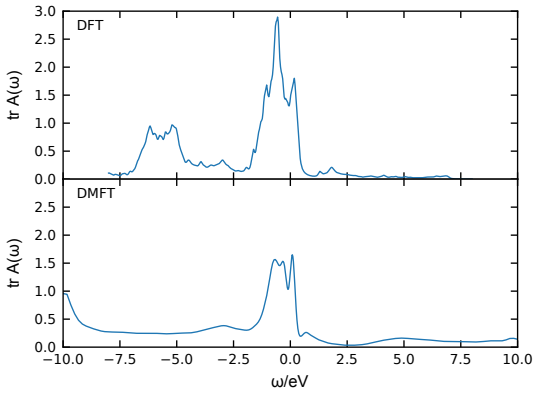

Figure 6.12: Total spectral function after basis reduction of the (001)-stacked $SrIrO_3$-$SrTiO_3$ heterostructure, both from DFT after the Wannier projection (top) and DFT+DMFT (bottom). The latter was obtained by element-wise analytic continuation using Maximum Entropy (see chapter 5) of the diagonal elements of the impurity Green's function using the preblur technique.

the chemical potential (at $\omega = 0$) is reduced in DMFT compared to DFT. There seems to be a formation of satellite peaks to the left and right of the main peak, but this could be an artefact of the analytic continuation[11]. Also, the shift of the states between -7.5 and $-5\,\mathrm{eV}$ towards lower energies should not necessarily be taken at face value, as the difference of the Hartree-Fock part of Σ and the double-counting suggests a maximum shift (i.e., between KS states with 100% target character for the correlated subspace and totally uncorrelated states) of roughly $-1\,\mathrm{eV}$.

In conclusion, the metal-insulator transition observed in experiment (see above) only arises when the canted anti-ferromagnetic order forms, as our calculations show that the paramagnetic phase is far from being insulating. This is in agreement with the findings of the studies published so far [172, 176, 177].

[11] The analytic continuation tends to work best for frequencies around $\omega = 0$, with increasingly washed-out features for higher frequencies. That problem is more serious the noisier the data gets. Due to the comparatively low fermionic sign, the statistics of our Monte Carlo results are not good, which increases the uncertainty of the spectral function.

7 Mott transition in Sr_2MgOsO_6

Among similar materials, Sr_2MgOsO_6 has an unusually high Néel temperature [186]. The known link between Mott physics and a high anti-ferromagnetic ordering temperature [44, 187] motivates us to investigate whether this material is actually close to a Mott transition. Furthermore, this compound allows us to test if our methodology yields results compatible to those published in the literature [188].

This chapter consists of original work by the author of this thesis.

7.1 Structure and description in DFT

The osmate compound Sr_2MgOsO_6 is a double perovskite with slight deviations from the ideal crystal structure (see figure 7.1) in order to accommodate the two different ions Mg and Os [186]. Osmium, which has atomic number 76, is a neighbor of iridium in the periodic table and much like the latter, it features a substantial spin-orbit coupling and, in many compounds, open d-shells. The in-plane lattice constant of the crystal is 5.56 Å and the out-of-plane lattice constant is 7.92 Å, which is a bit larger than twice the in-plane lattice constant divided by $\sqrt{2}$. All atoms, apart from the oxygens, sit at high-symmetry positions. The angle between the Os, Mg and O atoms is 4.3°, with the Mg–O distance being 2.07 Å and the Os–O distance 1.87 Å.

On the level of DFT (performed with Wien2k), the material comes out as metallic (see DOS plot in figure 7.2). This is at odds with experimental results [186] that clearly show an insulating behavior of the temperature-dependence of the resistivity. While there is a substantial hybridization of the Os d-shell with the oxygen states, there is hardly any hybridization between Os and Mg states (not shown). The t_{2g} states[1] clearly constitute the low-energy manifold in this system. That low energy manifold, which only slightly hybridizes with e_g states as seen by the very small e_g weight around $\omega = 0\,\text{eV}$, is well separated in energy (by band gaps) from all the other states in the system. Therefore, the basis optimization scheme from section 6.3 does not need to be employed here, but rather the description of the low-energy physics by constructing Wannier orbitals just on the t_{2g} states in an energy window of, say, $-1\,\text{eV}$ to $2\,\text{eV}$ around the Fermi level suggests itself. That route has been taken by a recent study of this system, both in DFT+U and DFT+DMFT [188] (see our comparison[2] with that paper in the following section).

[1] Again, due to lattice distortions and SOC, there is no t_{2g} irreducible representation of the d-shell, but we use

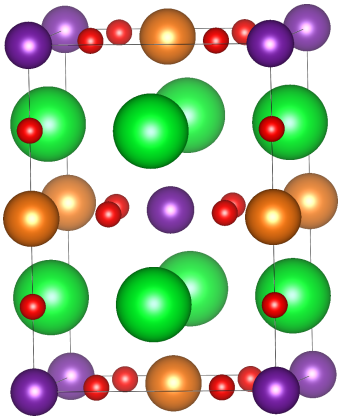

Figure 7.1: Crystal structure of the double perovskite Sr_2MgOsO_6. The Sr atoms are shown in green, the Mg atoms in orange, the Os atoms in purple and the O atoms in red.

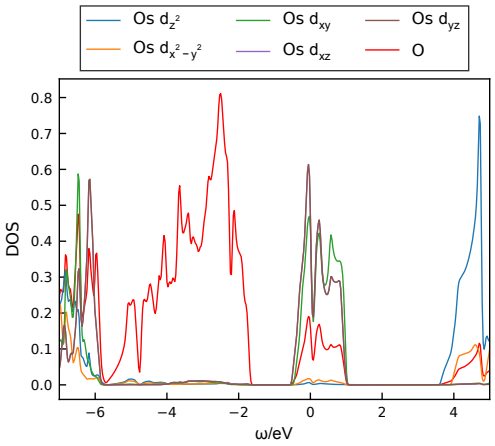

Figure 7.2: Kohn-Sham projected density of states of the paramagnetic double perovskite Sr_2MgOsO_6 (including SOC). The average projected DOS per Os and per O atom is shown. The Os d_{xz} and d_{yz} DOS are degenerate without SOC and practically degenerate with SOC.

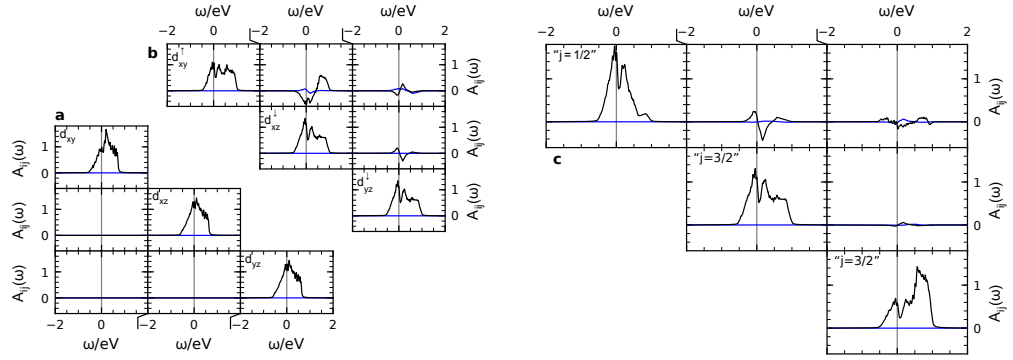

Figure 7.3: Non-interacting paramagnetic spectral function, calculated using PWF in the energy window $-1\,\mathrm{eV}$ to $2\,\mathrm{eV}$, of the double perovskite Sr_2MgOsO_6, both (b), (c) with and (a) without the inclusion of the SOC. (a) Without SOC, the spectral function is diagonal and spin-degenerate. (b) With SOC, there are off-diagonal elements; their real part is plotted in black and the imaginary part in blue. The SOC links the d_{xy} orbital to the opposite-spin d_{xz} and d_{yz} orbitals. Only half of the off-diagonal elements are shown, because $A(\omega)$ is Hermitian. (c) With SOC in the natural basis for that case, i.e., the numerical j-basis, which diagonalizes the local non-interacting Hamiltonian.

Figure 7.3 shows the effect of the SOC on that low-energy system. Most obviously, the non-interacting spectral function now features complex off-diagonal elements, as discussed in chapter 3. Moreover, the characteristic band-splitting due to the SOC occurs, yielding more peaks. As a consequence, also the total band width of the low-energy manifold increases.

In DFT, which is a zero-temperature theory, an antiferromagnetic ground state is energetically favorable compared to the paramagnetic calculation. Indeed, experiments [186] show an antiferromagnetic ordering below $T_N = 110\,\mathrm{K}$. Our DMFT calculations will be performed at room temperature ($\beta = 40\,\mathrm{eV}^{-1}$), where the paramagnetic state prevails.

7.2 Approximate DMFT with diagonal hybridization and interaction

In this section, we will replicate some of the calculations of Ref. [188]. There, the off-diagonal elements of the hybridization function are neglected in the numerical j-basis that diagonalizes the local non-interacting Hamiltonian. The interaction Hamiltonian takes into account only the density-density terms of the Kanamori Hamiltonian (2.43) with $U_K = 2.5\,\mathrm{eV}$ and $J_K/U_K = 0.15$. In contrast to our calculations, maximally localized Wannier functions (instead of projective

it as a name for the d_{xy}, d_{xz} and d_{yz} orbitals. We also call the $d_{x^2-y^2}$ and d_{z^2} orbitals the e_g orbitals.

[2] Being able to better compare with that study is a further reason for constructing the PWF for the t_{2g} states only. It is always hard to compare studies with different energy windows; due to the different screening, vastly different values of U would have to be used.

Wannier functions) and an exact diagonalization (ED) solver (instead of the CTHYB solver) are used. The ED solver has the advantage that it operates on the real-frequency axis, thereby eliminating the need for an analytic continuation, but needs to represent the infinite bath using a finite (and often very limited) number of bath sites. In Ref. [188], the DMFT calculation was performed at zero temperature (but, nevertheless, in a paramagnetic phase), which is not possible using the CTHYB solver (we choose room temperature instead). Redoing these calculations allows us to check whether we can produce results in accordance to those found in the literature.

As we see in the DFT calculations that the low-energy manifold is well-separated from the other states in the system, we construct PWF in an energy window from -1 to 2 eV for the d_{xy}, d_{xz}, and d_{yz} states[3]. The resulting spectral function was already discussed in the previous section in figure 7.3. In the cubic basis without SOC, the d_{xy} orbital is filled by 0.25 per spin, while the d_{xz} and d_{yz} orbitals are filled by 0.37 per spin. With SOC, in the numerical j-basis, the "$j = 1/2$"-orbital[4] is filled by 0.18, while the "$j = 3/2$"-orbitals are filled by 0.35 and 0.43, respectively (each of these comes twice, once per SOC-block). We see that the orbitals are a little bit more polarized in the numerical j-basis, with the "$j = 3/2$"-orbitals a little bit closer to half-filling.

This general trend was also observed and discussed in Ref. [188], although the actual numbers given for the fillings of the orbitals differ a bit, presumably due to the different approach for the construction of Wannier orbitals. There, the filling without SOC is given as 0.33 per spin channel, and no distinction is made between the d_{xy} and the d_{xz} and d_{yz} orbitals, in spite of the energy shift between these two kinds of orbitals. With SOC, the fillings are 0.45 for "$j = 3/2$" and 0.1 for "$j = 1/2$", which is even more polarized than in our calculation. We note that there, the two different "$j = 3/2$" orbitals seem to come out as degenerate on the DFT level in Ref. [188], which indicates that the local non-interacting Hamiltonian changes significantly between the MLWF and the PWF method, which in turn gives quite different numerical j-bases. On the DMFT level, that degeneracy is no longer observed in Ref. [188].

Without SOC, the hybridization is diagonal in the cubic basis, and the d_{xz} and d_{yz} orbital are degenerate. Using just density-density interaction terms, the material is very close to a metal-insulator transition, but already on the insulating side for the chosen values of the interaction parameters (see spectral function in the top graph of figure 7.4). The filling of the orbitals changes compared to DFT, with the d_{xy} reduced to 0.09 electrons per spin and the d_{xz} and d_{yz} orbitals increased to 0.45. Thus, the correlations push the latter orbitals closer to half-filling and the d_{xy} orbital closer to being empty.

When including the SOC and performing the calculation in the numerical j-basis, a larger Mott gap is observed (see figure 7.4, middle). Here, the $j = 1/2$ orbital is practically completely emptied

[3] The program `dmftproj` that comes with TRIQS/DFTTools does not allow the construction of PWF for a subset of a shell, unless it is an irreducible representation. Therefore we skip the orthonormalization in `dmftproj` and orthonormalize the PWF using a python program implementing the procedure described in section 2.3.1.

[4] We use quotes to indicate that j is not a good quantum number in the presence of crystal field; also, the expectation value of the J^2 operator in the numerical j-basis is *not* 1/2 or 3/2 for the two orbitals.

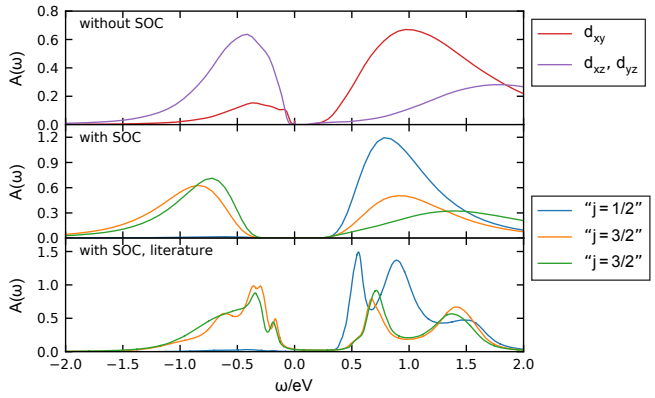

Figure 7.4: DMFT spectral function of the double perovskite Sr_2MgOsO_6, where the interaction consists of density-density terms alone. Without SOC (top), the calculation was performed in the cubic basis (where the hybridization and the local non-interacting Hamiltonian are diagonal). With SOC (middle), the off-diagonal elements of the hybridization are approximated to zero in the numerical j-basis. These two results were analytically continued using the maximum entropy method (see chapter 5; as the spectral function is diagonal here, no special treatment of the off-diagonal elements is necessary). For comparison (bottom), the result from Ref. [188] (also with SOC) is shown.

out (with a filling of 0.02, which is inside the error bar for being zero) and the $j = 3/2$ orbitals at half-filling (0.49 and 0.50, respectively). We, thus, see that the fact that the SO-coupled system is closer to having half-filled $j = 3/2$ states (i.e., 2 electrons in these 4 bands) in DFT leads to more strongly correlated behavior. It is possible to describe this in a cartoon picture in analogy to the already classical explanation for the physics of Sr_2IrO_4 [165]. The crystal field splits the Os $5d$ shell into t_{2g} and e_g bands; the t_{2g} bands are then split by the SOC into $j_{eff} = 1/2$ and $j_{eff} = 3/2$. Sr_2IrO_4, with its filling of 5 electrons in 6 bands, features a half-filled $j_{eff} = 1/2$ state and completely full $j_{eff} = 3/2$ states. Conversely, in Sr_2MgOsO_6, there are 2 electrons in the 6 bands, which leads to half-filled "$j = 3/2$" states and a completely empty "$j = 1/2$" state. As expected, half-filling promotes the Mott state.

The comparison of our PWF+CTHYB results (figure 7.4, middle) to the MLWF+ED results (figure 7.4, bottom) shows good qualitative agreement. The detailed shape of our analytically continued spectral function, which features broad and smeared-out peaks especially far away from $\omega = 0$, can never be expected to match the ED result, which tends to include spurious peaks due to the finite number of bath sites used. Nevertheless, the empty bands agree quite well; when transforming the spectral functions from Ref. [188] to $G(\tau)$ (not shown here), it agrees with our CTHYB results within the error bar for $\tau < \beta/2$, which (mostly) describes the empty states. The filled bands appear to be shifted in energy, which is also observed as a mismatch in $G(\tau)$ for $\tau > \beta/2$. While the reason for this mismatch remains unknown, the difference in the basis where the approximation is carried out as well as the difference between ED and CTHYB is the most

probable cause.

7.3 DMFT considering off-diagonal elements

The DMFT framework for complex, matrix-valued hybridization functions, as well as complex local and interaction Hamiltonians developed in the course of this thesis allows us to go beyond the approximation to use a diagonal hybridization function and only density-density terms of the Kanamori Hamiltonian. When performing that "full" DMFT calculation, we find a reduced effect of the electron-electron interaction (see figure 7.5). Without SOC, there are still remnants of a quasi-particle peak at $\omega = 0$; we observe a state that can be classified as *bad metal*. This can be quantified by means of the quasi-particle weight Z from (6.8), which can be estimated[5] to be 0.78 for the d_{xy} and 0.13 for the d_{xz} and d_{yz} orbitals. With SOC, a Mott gap is present, but smaller than in the approximated calculation. The values of Z without SOC and the fact that turning on the SOC leads to the crossing of the phase boundary between metal and insulator demonstrates the closeness of the system to the Mott transition, which is generally associated with a high Néel temperature [44, 187] (this is also pointed out in Ref. [188]).

Interestingly, the fillings of the orbitals come out basically identical (with the maximum deviation being 0.01) to the approximated case.

The matrix-valued plot of the spectral function in figure 7.6 shows very small off-diagonal elements. They are even reduced compared to the DFT result (see figure 7.3c), but that could be an artefact of the analytic continuation (which tends to be less reliable for small signal with large noise).

In the following, we perform a more detailed investigation of the difference between the full calculation and the approximate case. Instead of setting the off-diagonals of Δ to zero and using density-density terms only, we apply these two approximations separately (see figure 7.7). The off-diagonal elements of the hybridization play practically no role (in the numerical j-basis) for the diagonal elements of the spectral function, which are nearly identical to the full calculation. This could be expected already from figure 7.3, where one sees that the off-diagonal elements of the spectral function are relatively small compared to the diagonal elements. Note that if we compare to the full calculation in a different basis, e.g., the cubic basis, the results are not as similar because the off-diagonal elements come into play in the transformation. Of course, the trace of the spectral function, being basis independent, is practically identical.

Given this result, it does not come as a surprise that the ingredient being responsible for the difference between the approximate scheme from section 7.2 and the full calculation from figure 7.5 is the change in the local Hamiltonian. As the approximation of taking everything diagonal was performed in the numerical j-basis, where the local non-interacting Hamiltonian is diagonal, the

[5] At room temperature ($\beta = 40\,\mathrm{eV}^{-1}$), where our calculation was carried out, the energy scale given by the temperature is higher than the coherence scale. This makes the calculation of Z from this calculation unreliable (see, e.g., the Supplemental Material of Ref. [44]). The estimates given come from a fit of the imaginary part of the self-energy (polynomial of 4^{th} degree through the first 6 points).

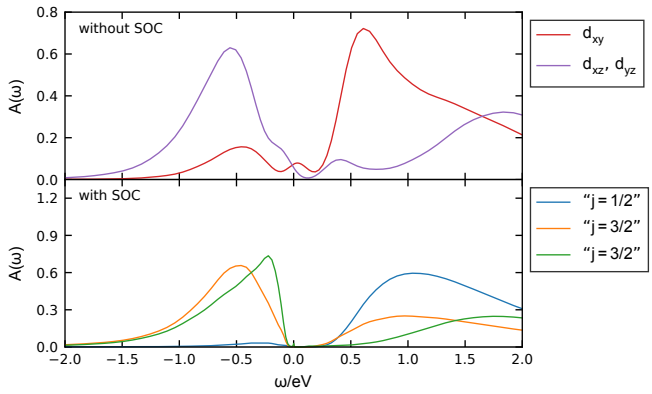

Figure 7.5: DMFT spectral function of the double perovskite Sr_2MgOsO_6, calculated with full Kanamori interaction. Without SOC (top), the calculation was performed in the cubic basis (where the hybridization and the local non-interacting Hamiltonian are diagonal). With SOC (bottom), the whole impurity problem was transformed in the numerical j-basis, which does not constitute an approximation. However, here just the diagonal elements are plotted (for a full-matrix plot see figure 7.6). The spectral function was obtained by analytic continuation of the impurity Green's function $G_{imp}(\tau)$ using the element-wise maximum entropy method (see chapter 5).

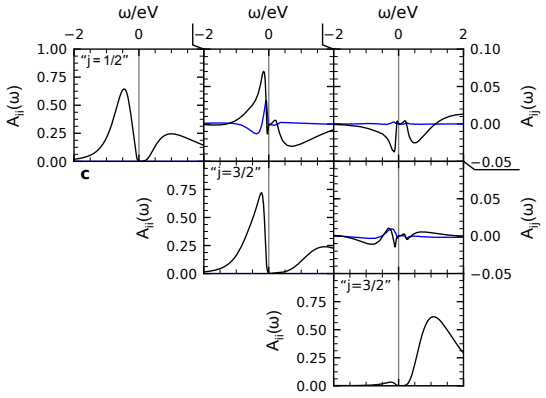

Figure 7.6: Matrix-valued DMFT spectral function of the double perovskite Sr_2MgOsO_6, calculated with full Kanamori interaction and SOC in the numerical j-basis. The diagonal and off-diagonal elements are plotted on different scales, with the former labeled on the left and the latter on the right. For the off-diagonal elements, the imaginary part is plotted in blue, the real part in black. The spectral function was obtained by analytic continuation of the impurity Green's function $G_{imp}(\tau)$ using the maximum entropy method (see chapter 5) in the full matrix formulation.

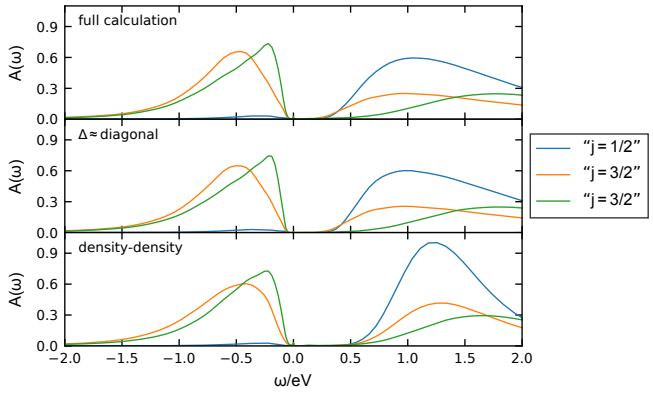

Figure 7.7: DMFT spectral function of the double perovskite Sr_2MgOsO_6 including the SOC in the numerical j-basis. In every case, just the diagonal elements are plotted. Once (top), the off-diagonal elements of the hybridization and the interaction terms beyond density-density interaction are taken into account (this is the same as in figure 7.5, bottom). Then, the hybridization is approximated to be diagonal (middle) while keeping the full Kanamori interaction. Finally, the whole hybridization is taken into account (bottom) but the interaction is approximated to density-density terms.

only part of the local Hamiltonian that is different is just the interaction part. Approximating the interaction but taking into account the full matrix-valued Δ, as in figure 7.7 (bottom), yields a result that strongly deviates from the full calculation (figure 7.7, top), but quite similar to the spectral function in figure 7.4 (middle). We can, therefore, identify the spin-flip and pair-hopping terms as the factors that are mostly responsible for the reduced correlation strength of the full calculation compared to the approximation of section 7.2. This effect is well-known and has been discussed in the literature [189, 190]. In other words, in order to avoid over-correlated results, the full Kanamori Hamiltonian has to be taken into account.

Finally, we want to comment on the computational effort of the different variants of the calculations. The average fermionic sign is 1.0 in the approximate case of section 7.2 and when a density-density interaction is used with a non-diagonal hybridization. When Δ is assumed to be diagonal and the Kanamori interaction is used, the average sign is 0.97, which is still very high. For the full calculation, an average sign of 0.78 is observed. Also the run-time is different (we do not take into account that, because of the different average sign, the run-times are not necessarily comparable as the resulting quality of the data is not the same). Comparing with the full calculation (which we define to take a time of 100%), using a diagonal Δ with the Kanamori interaction takes even longer, namely 109% (but the latter yields a higher-quality result). A drastic reduction of computational effort can be achieved by considering just density-density terms in the interaction (but, as discussed above, this gives inaccurate results), with the run-time being 38% with the full Δ and 24% with the approximate Δ (however, the latter is the only case where the real-valued version of the code can be and was employed, leading to a speed-up compared to complex arithmetics).

We note that in this osmate, a reasonable average sign was achieved in the basis that diagonalizes the local non-interacting Hamiltonian, which was not the case for the heterostructure in chapter 6. There, Δ had to be diagonalized (in leading order for $\omega_n \to \infty$) to get any meaningful results. In this osmate, the off-diagonal elements of the hybridization function are quite small in the numerical j-basis (which can be inferred from the spectral functions in figure 7.3c and 7.6); therefore, Δ is not the dominant part here. This indicates that these two systems are in different regimes concerning the sign problem, in the sense of the discussion in section 4.4.

Bibliography

1. Z. I. Alferov. "The semiconductor revolution in the 20th century". *Russ. Chem. Rev.* **82,** 587 (2013). → p. 21.
2. B. Keimer, S. A. Kivelson, M. R. Norman, S. Uchida, and J. Zaanen. "From quantum matter to high-temperature superconductivity in copper oxides". *Nature* **518,** 179 (2015). → p. 21.
3. M. Z. Hasan and C. L. Kane. "Colloquium: Topological insulators". *Rev. Mod. Phys.* **82,** 3045 (2010). → pp. 21, 22.
4. H. Allcock. *Introduction to Materials Chemistry.* (John Wiley & Sons, Hoboken, New Jersey, 2011). → p. 21.
5. D. Pesin and L. Balents. "Mott physics and band topology in materials with strong spin–orbit interaction". *Nature Physics* **6,** 376 (2010). → p. 21.
6. S. Curtarolo, G. L. W. Hart, M. B. Nardelli, N. Mingo, S. Sanvito, and O. Levy. "The high-throughput highway to computational materials design". *Nat. Mater.* **12,** 191 (2013). → p. 21.
7. A. Overhauser. *Anomalous Effects in Simple Metals.* (Wiley-VCH, Weinheim, 2010). → p. 22.
8. W. Metzner and D. Vollhardt. "Correlated Lattice Fermions in d=∞ Dimensions". *Phys. Rev. Lett.* **62,** 324 (1989). → pp. 22, 77.
9. A. Georges and G. Kotliar. "Hubbard model in infinite dimensions". *Phys. Rev. B* **45,** 6479 (1992). → pp. 22, 61, 77.
10. A. Georges, G. Kotliar, W. Krauth, and M. J. Rozenberg. "Dynamical mean-field theory of strongly correlated fermion systems and the limit of infinite dimensions". *Rev. Mod. Phys.* **68,** 13 (1996). → pp. 22, 28, 61, 62, 77, 86, 88.
11. G. Kotliar, S. Y. Savrasov, K. Haule, V. S. Oudovenko, O. Parcollet, and C. A. Marianetti. "Electronic structure calculations with dynamical mean-field theory". *Rev. Mod. Phys.* **78,** 865 (2006). → p. 22.
12. M. Aichhorn, G. J. Kraberger, G. Kresse, M. Marsman, O. Peil, M. Schüler, and T. O. Wehling. "Charge self-consistent DFT++ description of correlated electron systems in the Vienna Ab Initio Simulation Package". (authors in alphabetical order) (in preparation). → pp. 22, 43–45.
13. C. Martins, M. Aichhorn, L. Vaugier, and S. Biermann. "Reduced Effective Spin-Orbital Degeneracy and Spin-Orbital Ordering in Paramagnetic Transition-Metal Oxides: Sr_2IrO_4 versus Sr_2RhO_4". *Phys. Rev. Lett.* **107,** 266404 (2011). → p. 22.

14. R. Arita, J. Kuneš, A. V. Kozhevnikov, A. G. Eguiluz, and M. Imada. "Ab initio Studies on the Interplay between Spin-Orbit Interaction and Coulomb Correlation in Sr_2IrO_4 and Ba_2IrO_4". *Phys. Rev. Lett.* **108,** 086403 (2012). → p. 22.
15. J. Ferber, K. Foyevtsova, R. Valentí, and H. O. Jeschke. "LDA+DMFT study of the effects of correlation in LiFeAs". *Phys. Rev. B* **85,** 094505 (2012). → p. 22.
16. B. Amadon. "First-principles DFT+DMFT calculations of structural properties of actinides: Role of Hund's exchange, spin-orbit coupling, and crystal structure". *Phys. Rev. B* **94,** 115148 (2016). → p. 22.
17. Z. P. Yin, K. Haule, and G. Kotliar. "Fractional power-law behavior and its origin in iron-chalcogenide and ruthenate superconductors: Insights from first-principles calculations". *Phys. Rev. B* **86,** 195141 (2012). → p. 22.
18. H. Shinaoka, S. Hoshino, M. Troyer, and P. Werner. "Phase Diagram of Pyrochlore Iridates: All-in–All-out Magnetic Ordering and Non-Fermi-Liquid Properties". *Phys. Rev. Lett.* **115,** 156401 (2015). → p. 22.
19. W. Kohn. "Nobel Lecture: Electronic structure of matter – wave functions and density functionals". *Rev. Mod. Phys.* **71,** 1253 (1999). → p. 25.
20. R. Martin. *Electronic Structure: Basic Theory and Practical Methods.* (Cambridge University Press, 2004). → p. 25.
21. P. Hohenberg and W. Kohn. "Inhomogeneous Electron Gas". *Phys. Rev.* **136,** B864 (1964). → p. 25.
22. W. Kohn and L. J. Sham. "Self-Consistent Equations Including Exchange and Correlation Effects". *Phys. Rev.* **140,** A1133 (1965). → p. 26.
23. J. P. Perdew, K. Burke, and M. Ernzerhof. "Generalized Gradient Approximation Made Simple". *Phys. Rev. Lett.* **77,** 3865 (1996). → pp. 26, 94, 105.
24. P. Blaha, K. Schwarz, G. K. H. Madsen, D. Kvasnicka, and J. Luitz. *WIEN2K, An Augmented Plane Wave + Local Orbitals Program for Calculating Crystal Properties.* (Karlheinz Schwarz, Techn. Universität Wien, Austria, Wien, Austria, 2001). → pp. 26, 42, 94.
25. G. Kresse and J. Hafner. "Ab initio molecular dynamics for liquid metals". *Phys. Rev. B* **47,** 558 (1993). → pp. 26, 43, 105.
26. G. Kresse and J. Hafner. "Ab initio molecular-dynamics simulation of the liquid-metal–amorphous-semiconductor transition in germanium". *Phys. Rev. B* **49,** 14251 (1994). → pp. 26, 43, 105.
27. G. Kresse and J. Furthmüller. "Efficiency of ab-initio total energy calculations for metals and semiconductors using a plane-wave basis set". *Comp. Mat. Sci.* **6,** 15 (1996). → pp. 26, 43, 105.
28. G. Kresse and J. Furthmüller. "Efficient iterative schemes for ab initio total-energy calculations using a plane-wave basis set". *Phys. Rev. B* **54,** 11169 (1996). → pp. 26, 43, 105.
29. G. Kresse and D. Joubert. "From ultrasoft pseudopotentials to the projector augmented-wave method". *Phys. Rev. B* **59,** 1758 (1999). → pp. 26, 43, 44, 105.

30. A. Görling. "Density-functional theory for excited states". *Phys. Rev. A* **54,** 3912 (1996). → p. 27.
31. A. Georges and W. Krauth. "Physical properties of the half-filled Hubbard model in infinite dimensions". *Phys. Rev. B* **48,** 7167 (1993). → p. 30.
32. M. Potthoff. "Self-energy-functional approach: Analytical results and the Mott-Hubbard transition". *Eur. Phys. J. B* **36,** 335 (2003). → p. 30.
33. O. Parcollet, M. Ferrero, T. Ayral, H. Hafermann, I. Krivenko, L. Messio, and P. Seth. "TRIQS: A toolbox for research on interacting quantum systems". *Comput. Phys. Commun.* **196,** 398 (2015). → pp. 30, 42, 88, 94.
34. M. Aichhorn, L. Pourovskii, P. Seth, V. Vildosola, M. Zingl, O. E. Peil, X. Deng, J. Mravlje, G. J. Kraberger, C. Martins, M. Ferrero, and O. Parcollet. "TRIQS/DFTTools: A TRIQS application for ab initio calculations of correlated materials". *Comput. Phys. Commun.* **204,** 200 (2016). → pp. 30, 42, 94.
35. G. H. Wannier. "The Structure of Electronic Excitation Levels in Insulating Crystals". *Phys. Rev.* **52,** 191 (1937). → p. 31.
36. N. Marzari, A. A. Mostofi, J. R. Yates, I. Souza, and D. Vanderbilt. "Maximally localized Wannier functions: Theory and applications". *Rev. Mod. Phys.* **84,** 1419 (2012). → p. 31.
37. A. A. Mostofi, J. R. Yates, G. Pizzi, Y.-S. Lee, I. Souza, D. Vanderbilt, and N. Marzari. "An updated version of wannier90: A tool for obtaining maximally-localised Wannier functions". *Comput. Phys. Commun.* **185,** 2309 (2014). → pp. 31, 43.
38. R. Zwanzig. "Memory Effects in Irreversible Thermodynamics". *Phys. Rev.* **124,** 983 (1961). → p. 31.
39. H. Mori. "Transport, Collective Motion, and Brownian Motion". *Prog. Theor. Phys.* **33,** 423 (1965). → p. 31.
40. F. Lechermann, A. Georges, A. Poteryaev, S. Biermann, M. Posternak, A. Yamasaki, and O. K. Andersen. "Dynamical mean-field theory using Wannier functions: A flexible route to electronic structure calculations of strongly correlated materials". *Phys. Rev. B* **74,** 125120 (2006). → p. 31.
41. B. Amadon, F. Lechermann, A. Georges, F. Jollet, T. O. Wehling, and A. I. Lichtenstein. "Plane-wave based electronic structure calculations for correlated materials using dynamical mean-field theory and projected local orbitals". *Phys. Rev. B* **77,** 205112 (2008). → p. 31.
42. M. Aichhorn, L. Pourovskii, V. Vildosola, M. Ferrero, O. Parcollet, T. Miyake, A. Georges, and S. Biermann. "Dynamical mean-field theory within an augmented plane-wave framework: Assessing electronic correlations in the iron pnictide LaFeAsO". *Phys. Rev. B* **80,** 085101 (2009). → pp. 31, 34, 94.
43. P. Löwdin. "On the Non-Orthogonality Problem Connected with the Use of Atomic Wave Functions in the Theory of Molecules and Crystals". *J. Chem. Phys.* **18,** 365 (1950). → p. 32.
44. L. de'Medici, J. Mravlje, and A. Georges. "Janus-Faced Influence of Hund's Rule Coupling in Strongly Correlated Materials". *Phys. Rev. Lett.* **107,** 256401 (2011). → pp. 32, 121, 126.

45. V. I. Anisimov, F. Aryasetiawan, and A. I. Lichtenstein. "First-principles calculations of the electronic structure and spectra of strongly correlated systems: the LDA + U method". *J. Phys.: Condens. Matter* **9,** 767 (1997). → pp. 34, 35, 42.
46. A. I. Lichtenstein, M. I. Katsnelson, and G. Kotliar. "Finite-Temperature Magnetism of Transition Metals: An ab initio Dynamical Mean-Field Theory". *Phys. Rev. Lett.* **87,** 067205 (2001). → p. 34.
47. K. Held. "Electronic structure calculations using dynamical mean field theory". *Adv. Phys.* **56,** 829 (2007). → pp. 34, 46.
48. E. R. Ylvisaker, W. E. Pickett, and K. Koepernik. "Anisotropy and magnetism in the LSDA + U method". *Phys. Rev. B* **79,** 035103 (2009). → p. 34.
49. K. Haule. "Exact Double Counting in Combining the Dynamical Mean Field Theory and the Density Functional Theory". *Phys. Rev. Lett.* **115,** 196403 (2015). → p. 34.
50. F. Aryasetiawan, T. Miyake, and R. Sakuma. *The Constrained RPA Method for Calculating the Hubbard U from First-Principles.* in E. Pavarini, E. Koch, D. Vollhardt, and A. Lichtenstein. *The LDA+DMFT approach to strongly correlated materials* (Forschungszentrum Jülich, Jülich, 2011). → p. 35.
51. L. Vaugier, H. Jiang, and S. Biermann. "Hubbard U and Hund exchange J in transition metal oxides: Screening versus localization trends from constrained random phase approximation". *Phys. Rev. B* **86,** 165105 (2012). → p. 35.
52. L. Hedin. "New Method for Calculating the One-Particle Green's Function with Application to the Electron-Gas Problem". *Phys. Rev.* **139,** A796 (1965). → p. 36.
53. F. Aryasetiawan and O. Gunnarsson. "The *GW* method". *Rep. Prog. Phys.* **61,** 237 (1998). → p. 36.
54. D. Bohm and D. Pines. "A Collective Description of Electron Interactions. I. Magnetic Interactions". *Phys. Rev.* **82,** 625 (1951).
    D. Pines and D. Bohm. "A Collective Description of Electron Interactions: II. Collective vs Individual Particle Aspects of the Interactions". *Phys. Rev.* **85,** 338 (1952).
    D. Bohm and D. Pines. "A Collective Description of Electron Interactions: III. Coulomb Interactions in a Degenerate Electron Gas". *Phys. Rev.* **92,** 609 (1953). → p. 36.
55. M. S. Hybertsen and S. G. Louie. "Electron correlation in semiconductors and insulators: Band gaps and quasiparticle energies". *Phys. Rev. B* **34,** 5390 (1986). → p. 36.
56. R. W. Godby, M. Schlüter, and L. J. Sham. "Self-energy operators and exchange-correlation potentials in semiconductors". *Phys. Rev. B* **37,** 10159 (1988). → p. 36.
57. M. Springer and F. Aryasetiawan. "Frequency-dependent screened interaction in Ni within the random-phase approximation". *Phys. Rev. B* **57,** 4364 (1998). → p. 36.
58. F. Aryasetiawan, M. Imada, A. Georges, G. Kotliar, S. Biermann, and A. I. Lichtenstein. "Frequency-dependent local interactions and low-energy effective models from electronic structure calculations". *Phys. Rev. B* **70,** 195104 (2004). → p. 36.
59. F. Aryasetiawan, K. Karlsson, O. Jepsen, and U. Schönberger. "Calculations of Hubbard U from first-principles". *Phys. Rev. B* **74,** 125106 (2006). → p. 36.

60. V. I. Anisimov and O. Gunnarsson. "Density-functional calculation of effective Coulomb interactions in metals". *Phys. Rev. B* **43,** 7570 (1991). → p. 36.
61. A. Kutepov, K. Haule, S. Y. Savrasov, and G. Kotliar. "Self-consistent *GW* determination of the interaction strength: Application to the iron arsenide superconductors". *Phys. Rev. B* **82,** 045105 (2010). → pp. 36, 117.
62. T. Ribic, E. Assmann, A. Tóth, and K. Held. "Cubic interaction parameters for t_{2g} Wannier orbitals". *Phys. Rev. B* **90,** 165105 (2014). → pp. 37, 38.
63. J. Kanamori. "Electron Correlation and Ferromagnetism of Transition Metals". *Prog. Theor. Phys.* **30,** 275 (1963). → p. 38.
64. H. Shinaoka, Y. Nomura, S. Biermann, M. Troyer, and P. Werner. "Negative sign problem in continuous-time quantum Monte Carlo: Optimal choice of single-particle basis for impurity problems". *Phys. Rev. B* **92,** 195126 (2015). → pp. 39, 65.
65. M. Aichhorn, L. Pourovskii, and A. Georges. "Importance of electronic correlations for structural and magnetic properties of the iron pnictide superconductor LaFeAsO". *Phys. Rev. B* **84,** 054529 (2011). → pp. 41, 94.
66. K. Haule and T. Birol. "Free Energy from Stationary Implementation of the DFT + DMFT Functional". *Phys. Rev. Lett.* **115,** 256402 (2015). → p. 42.
67. V. Galitskii and A. Migdal. "Application of quantum field theory methods to the many body problem". *Sov. Phys. JETP* **7,** 96 (1958). → p. 42.
68. J. Ferber, K. Foyevtsova, H. O. Jeschke, and R. Valentí. "Unveiling the microscopic nature of correlated organic conductors: The case of κ-$(ET)_2Cu[N(CN)_2]Br_xCl_{1-x}$". *Phys. Rev. B* **89,** 205106 (2014). → p. 43.
69. P. E. Blöchl. "Projector augmented-wave method". *Phys. Rev. B* **50,** 17953 (1994). → p. 44.
70. O. Peil. Private communication. 2016. → p. 44.
71. S. Bhandary, E. Assmann, M. Aichhorn, and K. Held. "Charge self-consistency in density functional theory combined with dynamical mean field theory: k-space reoccupation and orbital order". *Phys. Rev. B* **94,** 155131 (2016). → pp. 45, 46.
72. P. Seth, I. Krivenko, M. Ferrero, and O. Parcollet. "TRIQS/CTHYB: A continuous-time quantum Monte Carlo hybridisation expansion solver for quantum impurity problems". *Comput. Phys. Commun.* **200,** 274 (2016). → pp. 46, 64, 88, 94.
73. J. Bjorken and S. Drell. *Relativistic quantum mechanics* (McGraw-Hill, New York, NY, 1964). → p. 49.
74. W. P. Huhn and V. Blum. "One-hundred-three compound band-structure benchmark of post-self-consistent spin-orbit coupling treatments in density functional theory". *Phys. Rev. Materials* **1,** 033803 (2017). → p. 49.
75. P. Novák. *Calculation of spin-orbit coupling*. Institute of Physics (Cukrovarnick 10, 162 53 Praha 6, Czech Republic). → p. 52.
76. C. Martins, M. Aichhorn, and S. Biermann. "Coulomb correlations in 4d and 5d oxides from first principles—or how spin-orbit materials choose their effective orbital degeneracies". *J. Phys.: Condens. Matter* **29,** 263001 (2017). → p. 52.

77. K. Yosida and K. Yamada. “Perturbation expansion for the Anderson Hamiltonian”. *Prog. Theor. Phys. Suppl.* **46,** 244 (1970). → pp. 61, 88.
78. K. Yamada. “Perturbation expansion for the Anderson Hamiltonian. II”. *Prog. Theor. Phys.* **53,** 970 (1975). → pp. 61, 88.
79. K. Yosida and K. Yamada. “Perturbation expansion for the Anderson Hamiltonian. III”. *Prog. Theor. Phys.* **53,** 1286 (1975). → pp. 61, 88.
80. M. J. Rozenberg, G. Kotliar, and X. Y. Zhang. “Mott-Hubbard transition in infinite dimensions. II”. *Phys. Rev. B* **49,** 10181 (1994). → pp. 61, 88.
81. N. Dasari, W. R. Mondal, P. Zhang, J. Moreno, M. Jarrell, and N. S. Vidhyadhiraja. “A multi-orbital iterated perturbation theory for model Hamiltonians and real material-specific calculations of correlated systems”. *Eur. Phys. J. B* **89,** 202 (2016). → p. 61.
82. L.-F. Arsenault, P. Sémon, and A.-M. S. Tremblay. “Benchmark of a modified iterated perturbation theory approach on the fcc lattice at strong coupling”. *Phys. Rev. B* **86,** 085133 (2012). → pp. 61, 118.
83. J. E. Hirsch and R. M. Fye. “Monte Carlo method for magnetic impurities in metals”. *Phys. Rev. Lett.* **56,** 2521 (1986). → pp. 61, 76.
84. M. Jarrell. “Hubbard model in infinite dimensions: A quantum Monte Carlo study”. *Phys. Rev. Lett.* **69,** 168 (1992). → p. 61.
85. M. J. Rozenberg, X. Y. Zhang, and G. Kotliar. “Mott-Hubbard transition in infinite dimensions”. *Phys. Rev. Lett.* **69,** 1236 (1992). → p. 61.
86. A. Georges and W. Krauth. “Numerical solution of the d=∞ Hubbard model: Evidence for a Mott transition”. *Phys. Rev. Lett.* **69,** 1240 (1992). → p. 61.
87. E. Gull, A. J. Millis, A. I. Lichtenstein, A. N. Rubtsov, M. Troyer, and P. Werner. “Continuous-time Monte Carlo methods for quantum impurity models”. *Rev. Mod. Phys.* **83,** 349 (2011). → pp. 61, 62, 76.
88. P. Werner, A. Comanac, L. de’Medici, M. Troyer, and A. J. Millis. “Continuous-Time Solver for Quantum Impurity Models”. *Phys. Rev. Lett.* **97,** 076405 (2006). → p. 61.
89. A. N. Rubtsov and A. I. Lichtenstein. “Continuous time quantum Monte Carlo method for fermions: beyond auxiliary field framework”. *JETP Lett.* **80** (2004). → p. 61.
90. M. Caffarel and W. Krauth. “Exact diagonalization approach to correlated fermions in infinite dimensions: Mott transition and superconductivity”. *Phys. Rev. Lett.* **72,** 1545 (1994). → p. 62.
91. G. Kotliar and A. E. Ruckenstein. “New Functional Integral Approach to Strongly Correlated Fermi Systems: The Gutzwiller Approximation as a Saddle Point”. *Phys. Rev. Lett.* **57,** 1362 (1986). → p. 62.
92. T. Pruschke and N. Grewe. “The Anderson model with finite Coulomb repulsion”. *Z. Phys. B* **74,** 439 (1989). → p. 62.
93. O. Sakai and Y. Kuramoto. “Application of the numerical renormalization group method to the hubbard model in infinite dimensions”. *Solid State Comm.* **89,** 307 (1994). → p. 62.

94. M. Zingl, M. Nuss, D. Bauernfeind, and M. Aichhorn. "A real-frequency solver for the Anderson impurity model based on bath optimization and cluster perturbation theory". *Physica B.* (2017). → p. 62.
95. D. J. García, K. Hallberg, and M. J. Rozenberg. "Dynamical Mean Field Theory with the Density Matrix Renormalization Group". *Phys. Rev. Lett.* **93,** 246403 (2004). → p. 62.
96. F. A. Wolf, A. Go, I. P. McCulloch, A. J. Millis, and U. Schollwöck. "Imaginary-Time Matrix Product State Impurity Solver for Dynamical Mean-Field Theory". *Phys. Rev. X* **5,** 041032 (2015). → p. 62.
97. D. Bauernfeind, M. Zingl, R. Triebl, M. Aichhorn, and H. G. Evertz. "Fork Tensor-Product States: Efficient Multiorbital Real-Time DMFT Solver". *Phys. Rev. X* **7,** 031013 (2017). → p. 62.
98. E. Gull. *Continuous-Time Quantum Monte Carlo Algorithms for Fermions.* PhD thesis (ETH Zürich, 2008). → p. 62.
99. A. Flesch, E. Gorelov, E. Koch, and E. Pavarini. "Multiplet effects in orbital and spin ordering phenomena: A hybridization-expansion quantum impurity solver study". *Phys. Rev. B* **87,** 195141 (2013). → pp. 65, 66.
100. T. Sato, T. Shirakawa, and S. Yunoki. "Spin-orbit-induced exotic insulators in a three-orbital Hubbard model with $(t_{2g})^5$ electrons". *Phys. Rev. B* **91,** 125122 (2015). → pp. 65, 66, 104.
101. P. Sémon and A.-M. S. Tremblay. "Importance of subleading corrections for the Mott critical point". *Phys. Rev. B* **85,** 201101 (2012). → p. 65.
102. L. Boehnke, H. Hafermann, M. Ferrero, F. Lechermann, and O. Parcollet. "Orthogonal polynomial representation of imaginary-time Green's functions". *Phys. Rev. B* **84,** 075145 (2011). → p. 68.
103. H. Shinaoka, J. Otsuki, M. Ohzeki, and K. Yoshimi. "Compressing Green's function using intermediate representation between imaginary-time and real-frequency domains". *Phys. Rev. B* **96,** 035147 (2017). → p. 68.
104. A.-M. Tremblay. *The Many-Body problem, from perturbation theory to dynamical-mean field theory (lecture notes).* 2017. URL: `https://www.physique.usherbrooke.ca/tremblay/cours/phy-892/N-corps.pdf`. → p. 69.
105. X. Wang, E. Gull, L. de'Medici, M. Capone, and A. J. Millis. "Antiferromagnetism and the gap of a Mott insulator: Results from analytic continuation of the self-energy". *Phys. Rev. B* **80,** 045101 (2009). → pp. 71, 87.
106. G. J. Kraberger, R. Triebl, M. Zingl, and M. Aichhorn. "Maximum entropy formalism for the analytic continuation of matrix-valued Green's functions". *Phys. Rev. B* **96,** 155128 (2017). → p. 75.
107. W. M. C. Foulkes, L. Mitas, R. J. Needs, and G. Rajagopal. "Quantum Monte Carlo simulations of solids". *Rev. Mod. Phys.* **73,** 33 (2001). → p. 76.
108. J. Harl and G. Kresse. "Accurate Bulk Properties from Approximate Many-Body Techniques". *Phys. Rev. Lett.* **103,** 056401 (2009). → p. 76.

109. M. Kaltak, J. Klimeš, and G. Kresse. "Cubic scaling algorithm for the random phase approximation: Self-interstitials and vacancies in Si". *Phys. Rev. B* **90,** 054115 (2014). → p. 76.
110. P. Liu, M. Kaltak, J. Klimeš, and G. Kresse. "Cubic scaling GW : Towards fast quasiparticle calculations". *Phys. Rev. B* **94,** 165109 (2016). → p. 76.
111. A. V. Ferris-Prabhu and D. H. Withers. "Numerical analytic continuation using Padé approximants". *J. Comput. Phys.* **13,** 94 (1973). → pp. 76, 88.
112. J. M. Tomczak, M. Casula, T. Miyake, F. Aryasetiawan, and S. Biermann. "Combined GW and dynamical mean-field theory: Dynamical screening effects in transition metal oxides". *Europhys. Lett.* **100,** 67001 (2012). → p. 76.
113. K. S. D. Beach, R. J. Gooding, and F. Marsiglio. "Reliable Padé analytical continuation method based on a high-accuracy symbolic computation algorithm". *Phys. Rev. B* **61,** 5147 (2000). → pp. 76, 79, 88.
114. R. N. Silver, D. S. Sivia, and J. E. Gubernatis. "Maximum-entropy method for analytic continuation of quantum Monte Carlo data". *Phys. Rev. B* **41,** 2380 (1990). → pp. 77, 88.
115. J. E. Gubernatis, M. Jarrell, R. N. Silver, and D. S. Sivia. "Quantum Monte Carlo simulations and maximum entropy: Dynamics from imaginary-time data". *Phys. Rev. B* **44,** 6011 (1991). → pp. 77, 78.
116. S. F. Gull and J. Skilling. "Maximum entropy method in image processing". *IEE Proc.-F* **131,** 646 (1984). → pp. 77, 80.
117. F. Bao, Y. Tang, M. Summers, G. Zhang, C. Webster, V. Scarola, and T. A. Maier. "Fast and efficient stochastic optimization for analytic continuation". *Phys. Rev. B* **94,** 125149 (2016). → p. 77.
118. A. W. Sandvik. "Stochastic method for analytic continuation of quantum Monte Carlo data". *Phys. Rev. B* **57,** 10287 (1998). → p. 77.
119. K. S. D. Beach. "Identifying the maximum entropy method as a special limit of stochastic analytic continuation". arXiv: `cond-mat/0403055`. → p. 77.
120. A. S. Mishchenko, N. V. Prokof'ev, A. Sakamoto, and B. V. Svistunov. "Diagrammatic quantum Monte Carlo study of the Fröhlich polaron". *Phys. Rev. B* **62,** 6317 (2000). → p. 77.
121. S. Fuchs, T. Pruschke, and M. Jarrell. "Analytic continuation of quantum Monte Carlo data by stochastic analytical inference". *Phys. Rev. E* **81,** 056701 (2010). → p. 77.
122. A. W. Sandvik. "Constrained sampling method for analytic continuation". *Phys. Rev. E* **94,** 063308 (2016). → p. 77.
123. C. E. Creffield, E. G. Klepfish, E. R. Pike, and S. Sarkar. "Spectral Weight Function for the Half-Filled Hubbard Model: A Singular Value Decomposition Approach". *Phys. Rev. Lett.* **75,** 517 (1995). → pp. 77, 83.
124. L.-F. Arsenault, R. Neuberg, L. A. Hannah, and A. J. Millis. "Projected Regression Methods for Inverting Fredholm Integrals: Formalism and Application to Analytical Continuation". arXiv: `1612.04895`. → p. 77.

125. J. Otsuki, M. Ohzeki, H. Shinaoka, and K. Yoshimi. "Sparse modeling approach to analytical continuation of imaginary-time quantum Monte Carlo data". *Phys. Rev. E* **95,** 061302 (2017). → pp. 77, 83.
126. D. Bergeron and A.-M. S. Tremblay. "Algorithms for optimized maximum entropy and diagnostic tools for analytic continuation". *Phys. Rev. E* **94,** 023303 (2016). → pp. 77, 80, 100.
127. R. Levy, J. P. F. LeBlanc, and E. Gull. "Implementation of the maximum entropy method for analytic continuation". *Comput. Phys. Commun.* **215,** 149 (2017). → pp. 77, 100.
128. H. T. Dang, X. Ai, A. J. Millis, and C. A. Marianetti. "Density functional plus dynamical mean-field theory of the metal-insulator transition in early transition-metal oxides". *Phys. Rev. B* **90,** 125114 (2014). → pp. 77, 94, 96.
129. J. M. Tomczak and S. Biermann. "Effective band structure of correlated materials: the case of VO $_2$". *J. Phys.: Condens. Matter* **19,** 365206 (2007). → pp. 77, 87.
130. M. Jarrell. *The Maximum Entropy Method.* in *Correlated Electrons: from Models to Materials* (eds E. Pavarini, E. Koch, F. Anders, and M. Jarrell) chap. 13 (Forschungszentrum Jülich, Jülich, 2012). → p. 77.
131. A. Reymbaut, D. Bergeron, and A.-M. S. Tremblay. "Maximum entropy analytic continuation for spectral functions with nonpositive spectral weight". *Phys. Rev. B* **92,** 060509 (27, 2015). → p. 77.
132. M. De Raychaudhury, E. Pavarini, and O. K. Andersen. "Orbital Fluctuations in the Different Phases of $LaVO_3$ and YVO_3". *Phys. Rev. Lett.* **99,** 126402 (2007). → p. 77.
133. I. S. Krivenko and A. N. Rubtsov. "Analytic Continuation of Quantum Monte Carlo Data: Optimal Stochastic Regularization Approach". arXiv: `cond-mat/0612233`. → p. 77.
134. J. Skilling. *Classic Maximum Entropy.* in *Maximum Entropy and Bayesian Methods* (ed J. Skilling) 45 (Kluwer Academic Publishers, Dortrecht, 1989). → pp. 77, 79–81, 97.
135. E. Laue, J. Skilling, and J. Staunton. "Maximum entropy reconstruction of spectra containing antiphase peaks". *J. Magn. Reson.* **63,** 418 (1985). → pp. 77, 81.
136. S. Sibisi. *Quantified Maxent: An NMR Application.* in *Maximum Entropy and Bayesian Methods* (ed P. F. Fougère) 351 (Kluwer Academic Publishers, Dordrecht, 1990). → pp. 77, 81.
137. K. Maisinger, M. P. Hobson, and A. N. Lasenby. "A maximum entropy method for reconstructing interferometer maps of fluctuations in the cosmic microwave background radiation". *Mon. Not. R. Astron. Soc.* **290,** 313 (1997). → pp. 77, 81.
138. A. W. Jones, S. Hancock, A. S. Lasenby, R. D. Davies, C. M. Gutierrez, G. Rocha, R. A. Watson, and R. Rebolo. "10-ghz tenerife cosmic microwave background observations at 8 resolution and their analysis using a new maximum entropy method". *Mon. Not. R. Astron. Soc.* **294,** 582 (1998). → pp. 77, 81.
139. M. P. Hobson and A. N. Lasenby. "The entropic prior for distributions with positive and negative values". *Mon. Not. R. Astron. Soc.* **298,** 905 (1998). → pp. 77, 81, 82, 98.
140. S. Gull and G. Daniell. "Image reconstruction from incomplete and noisy data". *Nature* **272,** 686 (1978). → p. 80.

141. D. M. Titterington. "General Structure of Regularization Procedures in Image Reconstruction". *Astron. Astrophys.* **144,** 381 (1985). → p. 80.
142. S. F. Gull. *Developements in Maximum Entropy Data Analysis.* in *Maximum Entropy and Bayesian Methods* (ed J. Skilling) 53 (Kluwer Academic Publishers, Dortrecht, 1989). → pp. 80, 97.
143. R. K. Bryan. *Solving oversampled data problems by Maximum Entropy.* in *Maximum Entropy and Bayesian Methods* (ed P. F. Fougère) 221 (Kluwer Academic Publishers, Dordrecht, 1990). → pp. 80, 83, 87, 97, 98.
144. W. von der Linden, R. Preuss, and V. Dose. *The Prior-Predictive Value: A Paradigm of Nasty Multi-Dimensional Integrals.* in *Maximum Entropy and Bayesian Methods* (eds W. von der Linden, V. Dose, R. Fischer, and R. Preuss) 319 (Kluwer Academic Publishers, Dortrecht, 1999). → p. 80.
145. M. Hohenadler, D. Neuber, W. von der Linden, G. Wellein, J. Loos, and H. Fehske. "Photoemission spectra of many-polaron systems". *Phys. Rev. B* **71,** 245111 (2005). → p. 80.
146. S. F. Gull and J. Skilling. *Quantified Maximum Entropy MemSys5 Users' Manual* (Maximum Entropy Data Consultants Ltd., Bury St. Edmunds, 1999). → p. 81.
147. D. W. Marquardt. "An Algorithm for Least-Squares Estimation of Nonlinear Parameters". *J. Soc. Ind. Appl. Math.* **11,** 431 (1963). → pp. 84, 87.
148. A. Liebsch and A. Lichtenstein. "Photoemission Quasiparticle Spectra of Sr 2 RuO 4". *Phys. Rev. Lett.* **84,** 1591 (2000). → p. 87.
149. S. Biermann, A. Dallmeyer, C. Carbone, W. Eberhardt, C. Pampuch, O. Rader, M. I. Katsnelson, and A. I. Lichtenstein. "Observation of Hubbard bands in γ-manganese". *JETP Lett.* **80,** 612 (2004). → p. 87.
150. V. S. Oudovenko, G. Pálsson, S. Y. Savrasov, K. Haule, and G. Kotliar. "Calculations of optical properties in strongly correlated materials". *Phys. Rev. B* **70,** 125112 (2004). → p. 87.
151. M. Jarrell, J. K. Freericks, and T. Pruschke. "Optical conductivity of the infinite-dimensional Hubbard model". *Phys. Rev. B* **51,** 11704 (1995). → p. 87.
152. V. I. Anisimov, D. E. Kondakov, A. V. Kozhevnikov, I. A. Nekrasov, Z. V. Pchelkina, J. W. Allen, S.-K. Mo, H.-D. Kim, P. Metcalf, S. Suga, A. Sekiyama, G. Keller, I. Leonov, X. Ren, and D. Vollhardt. "Full orbital calculation scheme for materials with strongly correlated electrons". *Phys. Rev. B* **71,** 125119 (2005). → p. 87.
153. J. Mravlje and A. Georges. "Thermopower and Entropy: Lessons from Sr_2RuO_4". *Phys. Rev. Lett.* **117,** 036401 (2016). → p. 87.
154. J. Skilling. *Fundamentals of MaxEnt in data analysis.* in *Maximum Entropy in Action* (eds B. Buck and V. A. Macaulay) 19 (Clarendon Press, Oxford, 1991). → p. 88.
155. P. Werner and A. J. Millis. "Hybridization expansion impurity solver: General formulation and application to Kondo lattice and two-orbital models". *Phys. Rev. B* **74,** 155107 (2006). → p. 88.

156. E. Pavarini, A. Yamasaki, J. Nuss, and O. K. Andersen. "How chemistry controls electron localization in 3d 1 perovskites: a Wannier-function study". *New J. Phys.* **7,** 188 (2005). → pp. 94, 96.
157. L. Craco, M. S. Laad, S. Leoni, and E. Müller-Hartmann. "Insulator-metal transition in the doped $3d^1$ transition metal oxide $LaTiO_3$". *Phys. Rev. B* **70,** 195116 (2004). → p. 94.
158. E. Pavarini, S. Biermann, A. Poteryaev, A. I. Lichtenstein, A. Georges, and O. K. Andersen. "Mott Transition and Suppression of Orbital Fluctuations in Orthorhombic $3d^1$ Perovskites". *Phys. Rev. Lett.* **92,** 176403 (2004). → pp. 94, 96.
159. M. Cwik, T. Lorenz, J. Baier, R. Müller, G. André, F. Bourée, F. Lichtenberg, A. Freimuth, R. Schmitz, E. Müller-Hartmann, and M. Braden. "Crystal and magnetic structure of $LaTiO_3$: Evidence for nondegenerate t_{2g} orbitals". *Phys. Rev. B* **68,** 060401 (2003). → p. 94.
160. S. van der Walt, S. C. Colbert, and G. Varoquaux. "The NumPy Array: A Structure for Efficient Numerical Computation". *Comput. Sci. Eng.* **13,** 22 (2011). → p. 97.
161. J. D. Hunter. "Matplotlib: A 2D graphics environment". *Comput. Sci. Eng.* **9,** 90 (2007). → p. 97.
162. R. D. Levine. "Geometry in classical statistical thermodynamics". *J. Chem. Phys.* **84,** 910 (1986). → p. 97.
163. C. C. Rodriguez. *The Metrics Induces by the Kullback Number.* in *Maximum Entropy and Bayesian Methods* (ed J. Skilling) 415 (Kluwer Academic Publishers, Dortrecht, 1989). → p. 97.
164. O. Gunnarsson, M. W. Haverkort, and G. Sangiovanni. "Analytical continuation of imaginary axis data for optical conductivity". *Phys. Rev. B* **82,** 165125 (2010). → p. 100.
165. B. J. Kim, H. Jin, S. J. Moon, J.-Y. Kim, B.-G. Park, C. S. Leem, J. Yu, T. W. Noh, C. Kim, S.-J. Oh, J.-H. Park, V. Durairaj, G. Cao, and E. Rotenberg. "Novel $J_{\text{eff}} = 1/2$ Mott State Induced by Relativistic Spin-Orbit Coupling in Sr_2IrO_4". *Phys. Rev. Lett.* **101,** 076402 (2008). → pp. 103, 125.
166. S. N. Ruddlesden and P. Popper. "The compound $Sr_3Ti_2O_7$ and its structure". *Acta Crystallogr.* **11,** 54 (1958). → p. 103.
167. T. Ohnishi, K. Shibuya, M. Lippmaa, D. Kobayashi, H. Kumigashira, M. Oshima, and H. Koinuma. "Preparation of thermally stable TiO_2-terminated $SrTiO_3$(100) substrate surfaces". *Appl. Phys. Lett.* **85,** 272 (2004). → p. 103.
168. J. G. Connell, B. J. Isaac, G. B. Ekanayake, D. R. Strachan, and S. S. A. Seo. "Preparation of atomically flat $SrTiO_3$ surfaces using a deionized-water leaching and thermal annealing procedure". *Appl. Phys. Lett.* **101,** 251607 (2012). → p. 103.
169. Y. A. Abramov, V. G. Tsirelson, V. E. Zavodnik, S. A. Ivanov, and B. I. D. "The chemical bond and atomic displacements in $SrTiO_3$ from X-ray diffraction analysis". *Acta Crystallogr. B* **51,** 942 (1995). → p. 103.
170. F.-X. Wu, J. Zhou, L. Y. Zhang, Y. B. Chen, S.-T. Zhang, Z.-B. Gu, S.-H. Yao, and Y.-F. Chen. "Metal–insulator transition in $SrIrO_3$ with strong spin–orbit interaction". *J. Phys.: Condens. Matter* **25,** 125604 (2013). → p. 103.

171. S. J. Moon, H. Jin, K. W. Kim, W. S. Choi, Y. S. Lee, J. Yu, G. Cao, A. Sumi, H. Funakubo, C. Bernhard, and T. W. Noh. "Dimensionality-Controlled Insulator-Metal Transition and Correlated Metallic State in 5*d* Transition Metal Oxides $Sr_{n+1}Ir_nO_{3n+1}$ ($n = 1$, 2, and ∞)". *Phys. Rev. Lett.* **101,** 226402 (2008). → p. 103.
172. J. Matsuno, K. Ihara, S. Yamamura, H. Wadati, K. Ishii, V. V. Shankar, H.-Y. Kee, and H. Takagi. "Engineering a Spin-Orbital Magnetic Insulator by Tailoring Superlattices". *Phys. Rev. Lett.* **114,** 247209 (2015). → pp. 103–106, 119.
173. T. J. Anderson, S. Ryu, H. Zhou, L. Xie, J. P. Podkaminer, Y. Ma, J. Irwin, X. Q. Pan, M. S. Rzchowski, and C. B. Eom. "Metastable honeycomb $SrTiO_3/SrIrO_3$ heterostructures". *Appl. Phys. Lett.* **108,** 151604 (2016). → p. 103.
174. J. L. Lado, V. Pardo, and D. Baldomir. "Ab initio study of Z_2 topological phases in perovskite (111) $(SrTiO_3)_7/(SrIrO_3)_2$ and $(KTaO_3)_7/(KPtO_3)_2$ multilayers". *Phys. Rev. B* **88,** 155119 (2013). → p. 103.
175. S. Okamoto, W. Zhu, Y. Nomura, R. Arita, D. Xiao, and N. Nagaosa. "Correlation effects in (111) bilayers of perovskite transition-metal oxides". *Phys. Rev. B* **89,** 195121 (2014). → p. 103.
176. P. Schütz, D. Di Sante, L. Dudy, J. Gabel, M. Stübinger, M. Kamp, Y. Huang, M. Capone, M.-A. Husanu, V. N. Strocov, G. Sangiovanni, M. Sing, and R. Claessen. "Dimensionality-Driven Metal-Insulator Transition in Spin-Orbit-Coupled $SrIrO_3$". *Phys. Rev. Lett.* **119,** 256404 (2017). → pp. 104, 119.
177. D. J. Groenendijk, C. Autieri, J. Girovsky, M. C. Martinez-Velarte, N. Manca, G. Mattoni, A. M. R. V. L. Monteiro, N. Gauquelin, J. Verbeeck, A. F. Otte, M. Gabay, S. Picozzi, and A. D. Caviglia. "Spin-Orbit Semimetal $SrIrO_3$ in the Two-Dimensional Limit". *Phys. Rev. Lett.* **119,** 256403 (2017). → pp. 104, 119.
178. K.-H. Kim, H.-S. Kim, and M. J. Han. "Electronic structure and magnetic properties of iridate superlattice $SrIrO_3/SrTiO_3$". *J. Phys.: Condens. Matter* **26,** 185501 (2014). → p. 104.
179. B. Cordero, V. Gomez, A. E. Platero-Prats, M. Reves, J. Echeverria, E. Cremades, F. Barragan, and S. Alvarez. "Covalent radii revisited". *Dalton Trans.* 2832 (2008). → p. 105.
180. M. J. D. Powell. "An efficient method for finding the minimum of a function of several variables without calculating derivatives". *Comput. J.* **7,** 155 (1964). → p. 111.
181. E. Jones, T. Oliphant, P. Peterson, *et al. SciPy: Open source scientific tools for Python.* 2001–. URL: `http://www.scipy.org/`. → p. 111.
182. T. E. Oliphant. "Python for Scientific Computing". *Comput. Sci. Eng.* **9,** 10 (2007). → p. 111.
183. P. E. Blöchl, O. Jepsen, and O. K. Andersen. "Improved tetrahedron method for Brillouin-zone integrations". *Phys. Rev. B* **49,** 16223 (1994). → p. 116.
184. H. Zhang, K. Haule, and D. Vanderbilt. "Effective $J = 1/2$ Insulating State in Ruddlesden-Popper Iridates: An LDA+DMFT Study". *Phys. Rev. Lett.* **111,** 246402 (2013). → p. 117.

185. J. M. Tomczak, M. Casula, T. Miyake, and S. Biermann. "Asymmetry in band widening and quasiparticle lifetimes in $SrVO_3$: Competition between screened exchange and local correlations from combined GW and dynamical mean-field theory GW + DMFT". *Phys. Rev. B* **90,** 165138 (2014). → p. 118.

186. Y. Yuan, H. L. Feng, M. P. Ghimire, Y. Matsushita, Y. Tsujimoto, J. He, M. Tanaka, Y. Katsuya, and K. Yamaura. "High-Pressure Synthesis, Crystal Structures, and Magnetic Properties of 5d Double-Perovskite Oxides Ca_2MgOsO_6 and Sr_2MgOsO_6". *Inorg. Chem.* **54,** 3422 (2015). → pp. 121, 123.

187. J. Mravlje, M. Aichhorn, and A. Georges. "Origin of the High Néel Temperature in $SrTcO_3$". *Phys. Rev. Lett.* **108,** 197202 (2012). → pp. 121, 126.

188. G. Giovannetti. *The influence of Coulomb Correlations and Spin-Orbit Coupling in the electronic structure of double perovskites Sr_2XOsO_6 (X=Sc, Mg).* 2016. arXiv: 1611.06482. URL: https://arxiv.org/abs/1611.06482. → pp. 121, 123–126.

189. T. Pruschke and R. Bulla. "Hund's coupling and the metal-insulator transition in the two-band Hubbard model". *Eur. Phys. J. B* **44,** 217 (2005). → p. 128.

190. V. I. Anisimov, D. M. Korotin, M. A. Korotin, A. V. Kozhevnikov, J. Kuneš, A. O. Shorikov, S. L. Skornyakov, and S. V. Streltsov. "Coulomb repulsion and correlation strength in LaFeAsO from density functional and dynamical mean-field theories". *J. Phys.: Condens. Matter* **21,** 075602 (2009). → p. 128.